

ONLINE INTERNSHIP

Batch 1 Report

Vol 1, August 2020



SSERD

INTERNSHIP & PROJECT
D I V I S I O N

www.sserd.org

Summary

03 Aerodynamic Study of HL-20
Design Modification



26 Comparison between
Multiple bare tethers and
single bare tether for
deorbiting satellites



47 To develop a predictive model
for the energy of Solar Flares
using Machine Learning
and to find the correlation
between Sunspot Area and
related parameters



92 Conceptual Design of
Self-Sustainable
Inflatable Martian
Habitat



129 Study of eccentricities in
planetary systems stabilized by
orbital resonance - a
Hamiltonian Approach





AERODYNAMIC STUDY OF HL-20 DESIGN MODIFICATION

Sierra Nevada Corporation's
Dream Chaser[®]

SNC



AUGUST 2020

Aerodynamic Study of HL-20 Design Modification

Internal guide - Sujay Sreedhar
External guide - Pavan Kumar



Our Team

1. Apurva Majumdar R17ME033 of REVA University.
2. Mridul Agarwal 180010034 of Indian Institute of Technology Bombay.
3. M Vishnu Sankar 18B030013 of Indian Institute of Technology Bombay.
4. Thejas K. V. 17ETAS012062 of M. S. Ramaiah University of Applied Sciences.
5. Maaz Ahmed Shariff 17ETAS012023 of M. S. Ramaiah University of Applied Sciences.
6. Anshoo Mehra 17ETAS012004 of M. S. Ramaiah University of Applied Sciences.
7. Nikhil S N 1DS17AE029 of Dayananda Sagar College of Engineering.
8. Preethi S 1DS17AE033 of Dayananda Sagar College of Engineering.
9. S Akshaya 1DS17AE059 of Dayananda Sagar College of Engineering.
10. Vinutha G 1DS17AE056 of Dayananda Sagar College of Engineering.
11. Isha G 1DS17AE060 of Dayananda Sagar College of Engineering.
12. Soumitra Manish Dodkey 18103086 of Hindustan Institute of Technology and Science.
13. Mihir Rai AE18B114 of Indian Institute of Technology Madras.
14. Nagachandra N PES1201700570 of PES University Bengaluru.

15. Uttkarsha Gupta AIT17BEAE060 Acharya Institute of Technology Bangalore.

16. Shivam Suri 17BAS1174 of Chandigarh University.

17. V Kabbilaash Kumar UR16AE052 of Karunya University.

Contents

Our Team.....	5
Acknowledgements	9
Abstract.....	10
List of Figures.....	11
List of Abbreviations.....	12
1 Introduction	13
1.1 Motivation	14
1.2 Aims and Objectives	15
2 Literature Survey.....	15
3 Methodology.....	16
4 Design & Analysis	17
4.1 Development of Solid Model:	18
4.2 Grid Size:	19
4.3 Mesh:	20
4.3.1 Skewness:	20

4.3.2 Orthogonal Quality:.....	20
4.3.3 Aspect Ratio:.....	21
5 Results and Discussions	21
6 Conclusions	22
6.1 Future Work	22
7 References	23

Acknowledgements

Before introducing our research internship work, we would like to thank the people without whom the success of this work would have been impossible. We express our deepest gratitude and indebtedness to Mr. Sujay Sreedhar who is the Co-Founder and Chairman of Society for Space Education Research and Development and Miss. Nikhitha C who is also the Co-founder Chief Executive Officer of Society for Space Education Research and Development. The organization gave us the opportunity during a COVID-19 pandemic to allow students from different parts of India to come and work together virtually.

We would like to thank Mr. Sujay Sreedhar yet again for taking up the role of our internal guide and constantly monitoring our work. We extend our gratitude to Mr. Pavan Kumar for being our external guide and sharing some wonderful insights in our research process. Their constant support and encouragement were instrumental in completion of this research work. The guidance that we received from them helped us at each step in successfully completing our work on time.

We feel short of words to express our heartfelt thanks to the entire SSERD team and to all our family members and friends and all those who have directly or indirectly helped us during the course of this Internship.

Abstract

Lifting Body Re-entry Vehicle configuration is one of the most promising approaches for developing a reusable re-entry vehicle. The combination of lifting re-entry and ballistic re-entry enables these vehicles to achieve deceleration values optimum for crewed re-entry. It also provides the vehicle an increased accuracy in landing, minimized heating rates and fair control over the manoeuvres. The optimization of the vehicle body shape to achieve desired lift to drag ratio and low ballistic coefficient is one of the prime focus of research on these vehicles. The diameter of launch vehicles imposes a constraint on the width of the re-entry vehicle design which directly affects the planform area of the re-entry vehicle. HL-20 PLS vehicle is a lifting body configuration developed by NASA Langley Research Centre in the 1990s with an intent to achieve frequent manned orbital missions. This study focuses on the aerodynamic effects of incorporating a retractable wing extension on the HL-20 PLS design. The simulation results indicate an improved lift to drag ratio performance at lower angles of attack for the modified HL-20 PLS design with wing extensions. The modified design is also observed to showcase an early stall character in comparison with the original design.

List of Figures

4.1	Profile on Symmetric Plane along Longitudinal Axis	10
4.2	Construction of critical contour points for generating profile curves	10
4.3	Contour projections developed on the nine cross-sectional planes about the Longitudinal axis	11
4.4	Completed Wireframe Model	11
4.5	Stitched Surface Model	12
4.6	Generated Solid Model	12
4.7	HL-20 Original Configuration	13
4.8	HL-20 Modified Configuration with Wing Extension	13
4.9	Top View of the Grid	14
4.10	Side View of the Grid	15
4.11	Static Mesh performed on the surface of HL-20 Model	15
4.12	Depiction of Minimum Nodal Distance	16
4.13	Flow conditions at the interior and exterior of geometry	17
4.14	Flow properties at 60 km altitude	17
5.1	Lift & Drag coefficients at different angle of attacks	19
5.2	Lift coefficient vs Angle of Attack (AOA)	20
5.3	Drag coefficient vs Angle of Attack (AOA)	20
5.4	C_L vs C_D	20

List of Abbreviations

NASA National Aeronautics and Space Administration

ACRC Assured Crew Return Capability

PLS Personnel Launch System

L/D Lift by Drag ratio

B.C. Ballistic Coefficient

M Mach Number

CFD Computational Fluid Dynamics **g** Gravitational acceleration of Earth

C_D Coefficient of Drag

C_L Coefficient of Lift

CATIA Computer Aided Three-Dimensional Interactive Application **igs** Initial Graphics Exchange Specification

ANSYS Analysis System **AOA** Angle of Attack

I Introduction

Flying Wings and Lifting Body configurations are quite often viewed as unconventional aircraft concepts. On the contrary, these configurations are more popular in the designing of modern re-entry vehicles. In a broad sense, the Flying Wing configuration can be defined as a vehicle that accommodates all of its body within the structure frame of a wing profile. On a similar note, a Lifting Body can be defined as a vehicle that is aerodynamically shaped to generate lift performance similar to that of a wing. Lifting Body configurations are usually characterized with small wing sections or no wings in their design.

The flying wing emerges to be one of the most assuring configurations when it comes to the designing of sub-orbital flights. This configuration covers a range of vehicle concepts like blended wing-body, C-wing, tailless aircraft, etc. Fuel savings and lower pollution rate are the foremost merits of a flying wing configuration. Since the engines can be mounted above the wing and the aircraft does not require complex high lift devices, this configuration results in a much quieter airplane.

A lifting body is essentially a wingless vehicle that flies due to the lift generated by the shape of its fuselage. The lifting-body concept was a radical departure from the

aerodynamics of conventional winged aircraft. However, the most logical method for generating lift is through wings, but wings do create issues because they need to be extremely strong to handle the aerodynamic and the thermal stresses at hypersonic speeds during re-entry phase.

Majority of the re-entry vehicle designs in the 20th century used the ballistic re-entry approach with a conical capsule design. Despite their success, they were limited by the requirements of large-area landing and diminished re-entry control. The concept of lifting body re-entry vehicles evolved during the early 1960s at NASA. They were mainly influenced by the Burnelli designs of lifting fuselages. Some notable early lifting body designs include M2-F2, HL-10 and X-24. HL-20 happens to be one such lifting body design developed by the Langley Research Centre at NASA. It was developed as a part of two NASA programs, Assured Crew Return Capability ACRC Program and the Personnel Launch System (PLS) program, with a concept for manned orbital missions. The overall design of the HL-20 PLS concept has incorporated the deterrent from the operation of the Space Shuttle. Vehicle subsystems are located close to the exterior of the vehicle and removable panels are provided for easy access to these subsystems for quick vehicle maintenance and turnaround. Overall, HL-20 PLS vehicle processing is expected to be substantially

less than for the Space Shuttle orbiter. This vehicle would be launched into the orbit by a booster rocket or carried within the payload bay of the space shuttle orbiter. The vehicle would then deorbit by using an on-board propulsion system and perform a nose first re-entry and horizontal, possibly unpowered landing. It is designed to carry up to 10 people and very little cargo. The test results indicate the vehicle has a trimmed maximum hypersonic L/D of about 1.4. At subsonic speeds the vehicle has longitudinal trim at close to maximum L/D and a subsonic L/D of about 4.2. This reusable vehicle, designated the HL-20, has been designed for safe and reliable operations; improved operability, maintainability and affordability; and reduced life-cycle costs associated with placing people in orbit. The results of the human factors studies have shown where improvements in the baseline HL-20 design are desirable. These improvements will have little impact on overall vehicle shape or aerodynamic performance.

The ballistic coefficient (B.C.) describes how air resistance slows a projectile in flight. Low ballistic coefficients of the spacecraft will be effective in reducing the heat rate on the surface of the spacecraft. Therefore, in this research work an attempt has been made to reduce ballistic coefficient of the HL-20 design with the addition of retractable wing extensions.

I.I Motivation

The three crucial parameters affecting the sub-orbital and orbital space flights are deceleration of the spacecraft, heating rates during the descent and safe landing with accuracy. For unmanned space flights, the deceleration rate is limited by the structural loading that a spacecraft can take. However, human crew space exploration missions add an additional constraint on the deceleration limiting the maximum 'g' load around 6-7 g's. For a safe re-entry, the spacecraft must be ensured to remain in the re-entry corridor, ensuring the right flight velocity and drag conditions. If the entry angle is too steep the spacecraft would cross the undershoot boundary leading to rapid deceleration and adverse heating.

Spacecrafts with low-ballistic coefficients are much efficient in minimizing the heating rate on the spacecraft surface and ensuring optimum deceleration. The ballistic coefficient is inversely proportional to the cross-sectional area facing the flow direction. The width of spacecrafts designed for suborbital and orbital flights are constrained by the diameter of the launch-vehicle. The incorporation of extendable surfaces helps in overcoming the limitation of this constraint. During re-entry, this additional surface area will help in minimizing the ballistic coefficient and increasing the lift generation.

I.2 Aims and Objectives

During the initial survey, the performance parameters of Spaceship Two developed by Virgin-Galactic and Dream Chaser developed by Sierra Nevada Corporation were found to be promising for suborbital and orbital flights. Spaceship Two employs a unique feather configuration to increase the drag for deceleration during re-entry. But it suffers in achieving directional stability at low supersonic speeds. Dream Chaser is a lifting body configuration which uses the body lift generated to decelerate the space-craft. It is a successor of HL-20 Personnel Launch System developed by NASA and shares very close similarity with respect to design. The flat belly surface in both the designs make them the best suitable vehicle for incorporating an extendable wing surface. This project aims to study the aerodynamic effects of incorporating a retractable wing extension to the HL-20 design in comparison with the original configuration. The wing extension is intended to provide a larger surface area during re-entry, thereby increasing the lift and reducing the ballistic coefficient of the spacecraft.

2 Literature Survey

Soumya Dutta et al. (12) have investigated the design challenges in implementing entry

systems to Venus with shallow flight path angles and low ballistic coefficient. The possibility of using a deployable aeroshell during Venus entry to increase the wetted area and its effect on achieving a better trajectory is discussed.

Jeffrey S. Robinson et al. (11) have presented an investigation related to trajectory planning for crewed re-entry vehicles along with associated aero-heating environments. The re-entry data related to the Apollo Command Module is used to serve as a baseline for investigation. It presents methods used for identifying trajectories suitable for ablative systems and reusable systems. These methods include the selection of a reasonable range of initial velocity, ballistic coefficients and initial flight path angles to generate the trajectories.

G. M. Ware et al. (9) have studied the aerodynamic characteristics of HL-20 configuration and conclude about the lateral and longitudinal stability of the design in test Mach number range from 10 to 0.2. The study also presents the modifications to the outboard fins into an air foil shape and the associated effects on improved L/D ratio.

Yongyuan Li et al. (8) have presented the use of Genetic Algorithm for optimizing the aerodynamic shape of a lifting body. It uses the shape parameters of existing lifting body

designs as design variables to optimize the aerodynamic characters.

Dan Almosnino (7) has presented a study on the use of Euler-Adjoint solver for studying the aerodynamic characteristics of HL-20 for Mach number ranging from M=0.3 to

M=20. The study makes use of a 7% scale model for running the simulation and presents the computational considerations specific to the solver used.

K. James Weilmuenster et al. (5) have investigated the solution techniques for CFD analysis of HL-20 configuration at hypersonic conditions. The results indicate the negligible real-gas effects on the aerodynamic characters of the vehicle at these conditions. The results of surface heating were found to match closely with those obtained from NavierStokes solutions.

Zachary R. Putnam et al. (4) have presented a study on the feasibility of flying HL-20 without a steady-state body flap deflection.

R. Dale Reed (16) has recorded the early history and development of Lifting Body designs in the book 'Wingless Flight'. It explores the various factors and design considerations that have coursed the lifting body designs for suborbital flights and space flights. Richard M. Wood et al. (1) have presented a detailed study on the various classes of lifting vehicles including flying

wing and lifting body designs. The paper describes the relationships between these classes and also marks the importance of some of the influential designs belonging to these lifting vehicle classes.

B. Spencer et al. (2) have investigated into providing Personnel Launch System vehicle that is inherently stable from the re-entry phase to landing. It also looks into the improvement of aerodynamic performance of HL-20 in subsonic regimes by making few modifications into the original design. The paper also presents the cross-sectional dimensions of the original HL-20 7% scale model along the longitudinal axis. This data is used in our study to prepare the HL-20 model for simulation.

3 Methodology

The ballistic coefficient of a re-entry vehicle depends on the mass, drag coefficient and the cross-sectional area of the vehicle in the direction of velocity. It is given by the formula

$$B.C = \frac{M}{C_D * A} \quad (3.1)$$

where,

B.C. – Ballistic Coefficient

M – Mass of the spacecraft

C_D – Drag Coefficient

A – Cross-sectional area in the direction of velocity

The mass of the spacecraft is less ideal to be used for the control of ballistic coefficient during re-entry. In lifting body designs, the drag coefficient and the cross-sectional area are adjusted to obtain a desired ballistic coefficient by controlling the angle of attack of the vehicle. In order to achieve a lower ballistic coefficient, the angle of attack has to be increased to increase the effective area in the direction of velocity. An increased angle of attack can severely affect the lift generation beyond the stall angle, thereby setting up a limitation. The use of extendable wings can ensure the achievement of a low ballistic coefficient at a relatively lower angle of attack.

The aerodynamic performances of the original HL-20 configuration from experimental studies for Mach numbers ranging from 0.3 to 10 were studied. In order to demonstrate the feasibility of using this vehicle for sub-orbital flight space tourism, the study was focused on the descent phase from 100 km to 60 km altitude. A study was carried out to explore the mathematical models for Computational Fluid Dynamic simulations that were feasible with the aerodynamic and thermodynamic conditions at those altitudes. Due to computational limitations, it was decided to study the aerodynamic

characters at a Mach Number of 4 with free-stream conditions matching that of 60 km altitude for both the original and the modified HL-20 configurations. The range of angle of attack for the simulation was set from -5 degree to 35 degree. The obtained lift and drag coefficients were then used to draw a comparison between the variation in these parameters for both the models.

4 Design & Analysis

The modelling of the HL-20 vehicle was done using the CATIA V5 modelling tool. The essential cross-section dimensions for modelling were obtained from a journal paper presented by B. Spencer et al. The paper had presented the dimensions of a 7% scale model. This was scaled up to obtain the original dimensions of the HL-20 vehicle. A hybrid design environment is used on CATIA V5 software to enable the development of complex surfaces. The design process involved the construction of a wireframe model from the computed dimensions, generation of surfaces from the curves and conversion of surface model into a solid model.

Construction of Wireframe Model: The wireframe and surface modelling environment are used initially to generate a wireframe model. The profile of the HL-20 about its symmetric plane along the longitudinal axis was constructed. Nine

cross sectional planes at locations 0.05, 0.14, 0.25, 0.34, 0.45, 0.60, 0.75, 0.90 and 1.0, expressed as fractions of total length from the nose of the vehicle were constructed. The contour of the vehicle as projected on these planes were constructed by identifying few critical contour points. The completed wireframe model is then checked for any mismatched point while generating the curves.

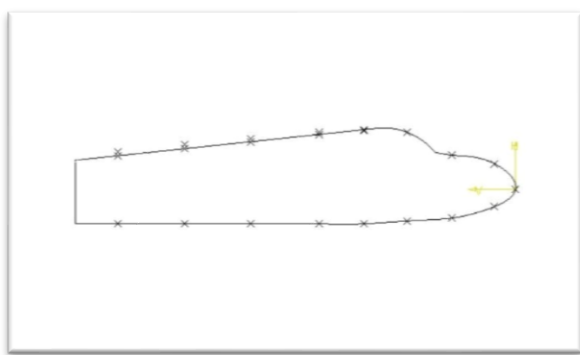


Figure 4.1: Profile on Symmetric Plane along Longitudinal Axis

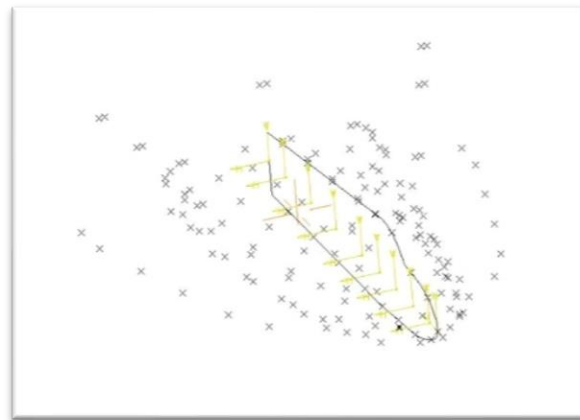


Figure 4.2: Construction of critical contour points for generating profile curves

4.1 Development of Solid Model:

The closed curves in the wireframe model are then used to generate surfaces. The selection of closed curves was carefully done so as to maintain continuous adjoining surfaces throughout the model. The surfaces so developed are then stitched together to enclose one single model. In the part design environment, the stitched surface model is converted into solid model. The completed model is then exported to igs format.

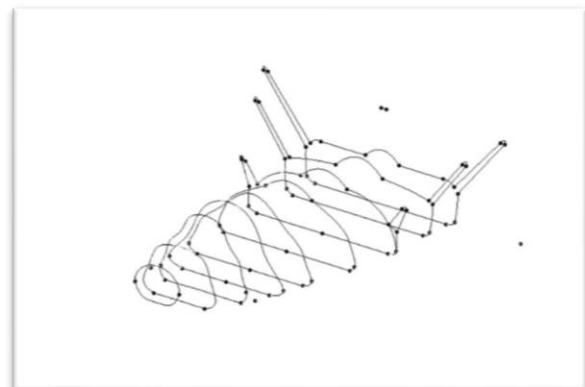


Figure 4.3: Contour projections developed on the nine cross-sectional planes about the Longitudinal axis.

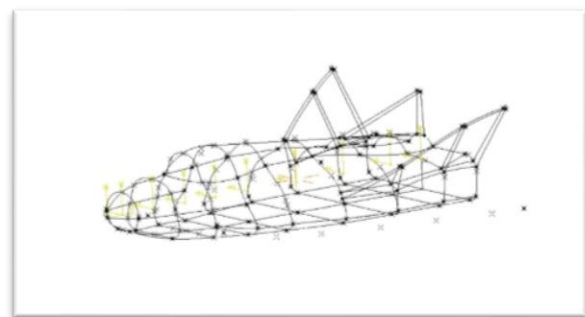


Figure 4.4: Completed Wireframe Model.

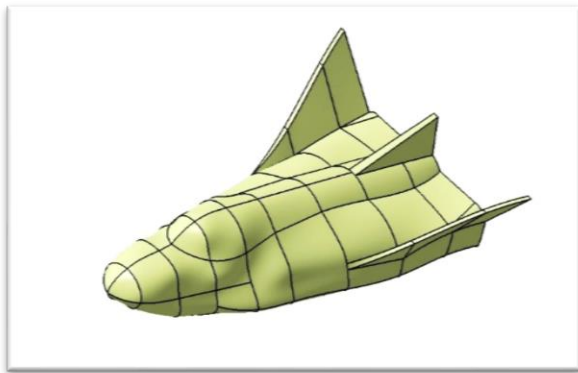


Figure 4.5: Stitched Surface Model

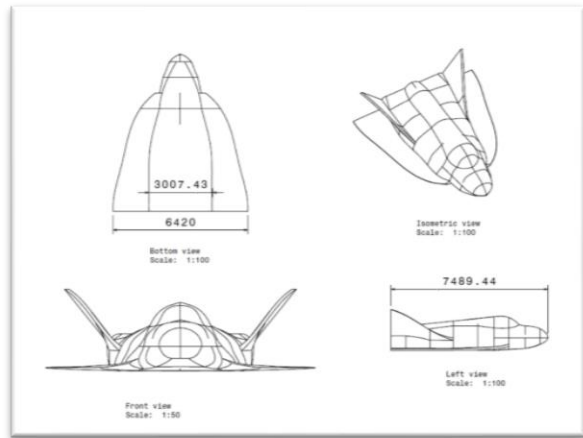


Figure 4.8: HL-20 Modified Configuration with Wing Extension.

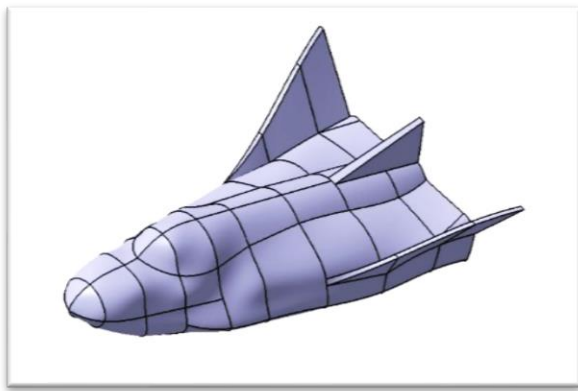


Figure 4.6: Generated Solid Model

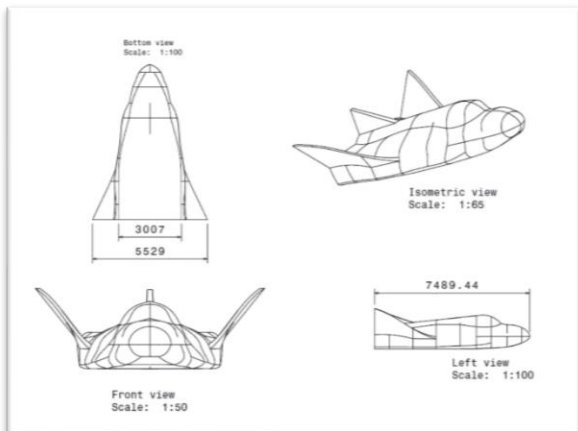


Figure 4.7: HL-20 Original Configuration

The meshing and flow simulation over both the models were performed using ANSYS software. The details of the mesh performed and the flow simulation conditions are discussed below.

4.2 Grid Size:

The grid is an enclosure of 27.5x22x13.2 cuboid, a model symmetric about its longitudinal axis is used to reduce the number of cells and computation time. Due to computational limitations, a grid of larger size couldn't be employed.

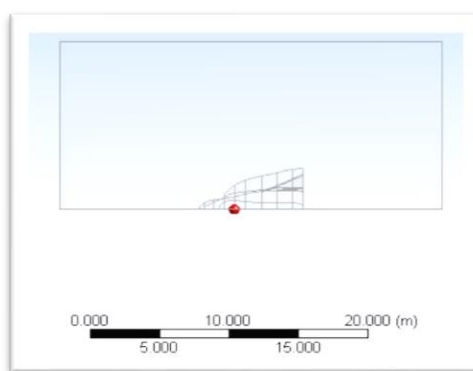


Figure 4.9: Top View of the Grid

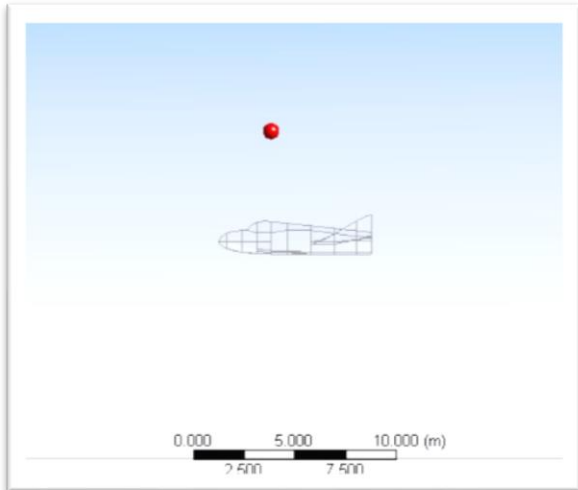


Figure 4.10: Side View of the Grid.

4.3 Mesh:

A static mesh with an average element size of 10cm on the surface of HL-20 and 25 cm on the grid was used. The boundary of the model consists of 10 inflation layers with distance between the nodes being as low as 0.4735 cm.

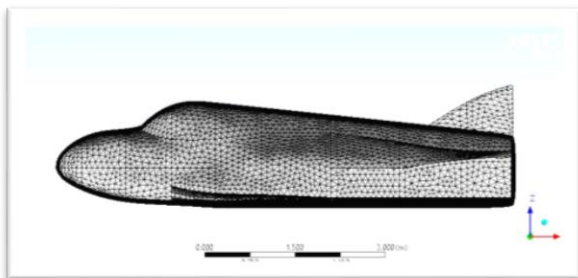


Figure 4.11: Static Mesh performed on the surface of HL-20 Model.

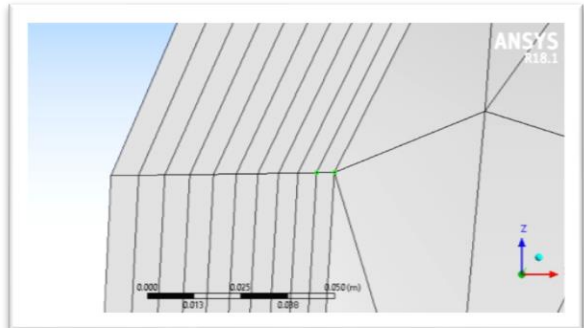


Figure 4.12: Depiction of Minimum Nodal Distance

The Mesh Metric characters like Skewness, Orthogonality, Aspect Ratio and Element Quality employed for the simulation are discussed below.

4.3.1 Skewness:

Skewness is a value that measures how much a cell is deformed from its ideal counterpart. For instance, the skewness of an irregular triangle is measured as the deviation of its edges from the corresponding edges of an equilateral triangle. A lower skewness value ensures the regularity of cells. For triangular cells, the skewness value is recommended to be placed below 0.85 in ANSYS for minimizing the computational errors. The mesh employed has a skewness value of cells below 0.65.

4.3.2 Orthogonal Quality:

It gives a measure of how close are the angles between the adjacent element faces with respect to an optimal angle. A value

close to 1 is recommended for accurate results. The average value of the orthogonal quality of the model was found to be 0.78.

4.3.3 Aspect Ratio:

Aspect ratio is the measure of the stretching of a cell. It is defined as ratio of the shortest edge to the longest edge of a cell. ANSYS recommends an average value between 1 to 5 for accurate results. The mesh was found to have an average value of 2.21.

The flow conditions for the simulation was set to match the free-stream atmospheric conditions at an altitude of 60 Km. The flow Mach number was set to M=4.

Ideal compressible gas was used with Sutherland's model to compute the dynamic viscosity. The specific heats were kept constant to reduce the complexities in simulation. With reference to a study made by Miroslav P. Pajcin et al on numerical analysis of hypersonic turbulent and laminar flow, the Standard k- Turbulence model was used for the simulation. The simulations were performed for angles of attack ranging from -5 degree to 35 degree in steps of 5 degrees.

Geometry	Flow Condition
Inlet	Mach 4
Outlet	Free-stream conditions
HL-20 Surface	No-Slip Condition
Plane of Symmetry	Symmetry

Figure 4.13: Flow conditions at the interior and exterior of geometry

Mach	4
Altitude (km)	60
Temperature (K)	247.02
Pressure (Pa)	21.96
Density (kg/m^3)	3.10E-04
Dynamic Viscosity (Pas)	1.58E-05

Figure 4.14: Flow properties at 60 km altitude

5 Results and Discussions

The lift coefficients and drag coefficients obtained at different angles of attack are listed in the figure 5.1 for both the configurations.

It is observed that the lift coefficient increases by a fair amount in the configuration

Angle of Attack (degree)	Original Configuration			Modified Configuration		
	Cl	Cd	L/D	Cl	Cd	L/D
-5	-0.7637	0.9959	-0.7669	-1.6505	1.1315	-1.4587
0	-0.0816	0.8958	-0.0911	-0.0861	0.8056	-0.1069
5	0.59797	0.9397	0.6363	0.9552	1.114	0.8575
10	1.3093	1.1264	1.1624	2.2627	1.4694	1.5399
15	2.081	1.4729	1.4129	3.5504	2.0443	1.7367
20	2.4078	1.8385	1.3097	4.9002	2.6936	1.8192
25	2.4464	2.1071	1.1610	4.2978	3.1408	1.3684
30	2.2628	2.2582	1.0020	3.2718	3.526	0.9279
35	1.8074	2.7562	0.6558	2.7855	2.9814	0.9343

Figure 5.1: Lift & Drag coefficients at different angle of attacks

with wing extension as expected. However, it is also accompanied by an early stall occurring at 20-degree angle of attack in the modified configuration. The original HL20 configuration exhibits a more gradual stall character. The L/D ratio is also found to be

higher in the regime of 5 degree to 25 degree for the modified configuration.

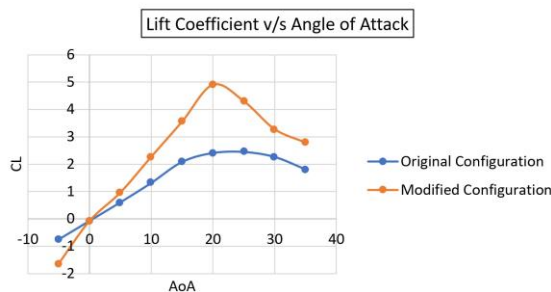


Figure 5.2: Lift coefficient vs Angle of Attack (AOA)

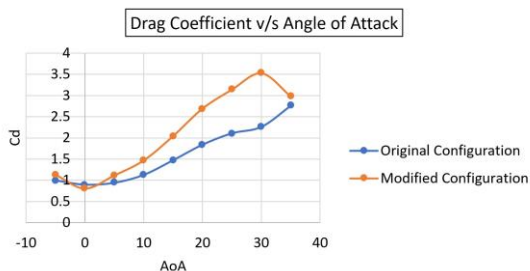


Figure 5.3: Drag coefficient vs Angle of Attack (AOA)

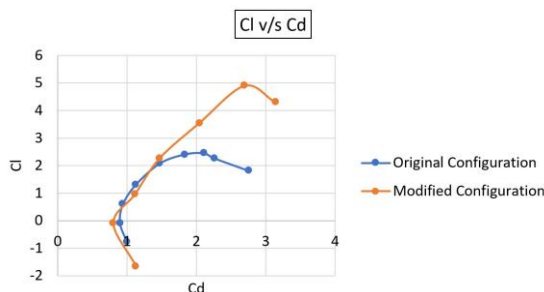


Figure 5.4: C_L vs C_D

6 Conclusions

The re-entry performance of a Lifting Body is determined mainly by its ballistic coefficient and L/D characteristics. A non-lifting body re-entry vehicle like a capsule usually employs a high ballistic coefficient

and prefers a direct re-entry trajectory with steeper flight path angles and shorter re-entry time. They result in very high surface heating and limited manoeuvrability. The employment of lift generated and low ballistic coefficient during re-entry in a lifting body configuration results in better re-entry performance. The constraint imposed by the diameter of a launch vehicle on the width of the re-entry vehicle could be overcome by having retractable wing extensions. The increased surface area during re-entry with this modification is valuable in lowering the ballistic coefficient of the vehicle.

Incorporation of wing extensions on the lifting re-entry vehicle showed to induce an early stall performance. However, it was also found to improve the aerodynamic lift and L/D ratio characteristics of the re-entry vehicle. A more precise study on the shape of wing extension has to be made in order to delay the stall and achieve better performance in all flight regimes.

6.1 Future Work

The current work crudely tries to explore the effects of incorporating a retractable wing extension on HL-20 PLS vehicle. Due to the limitations in the mathematical models

used for simulation in ANSYS software, the study was performed at a lower altitude of

60 km to compare the performances of the designs. There is also a requirement for looking into the mesh size quality and performing the grid independency test to ensure accurate results. A further extension of this work is to explore an optimal wing shape and associated dimensions that result in best aero-thermodynamic performance of the vehicle under all flight regimes ranging from subsonic to hypersonic.

7 References

- [1] Richard M. Wood and Steven X. S. Bauer, 'Flying Wings/ Flying Fuselages', <https://www.researchgate.net/publication/23826642>, AIAA, 2001.
- [2] B. Spencer Jr. et al, 'A Study to Determine Methods of Improving the Subsonic Performance of a Proposed Personnel Launch System (PLS) Concept', NASA Technical Memorandum 110201, NASA Langley Research Centre, 1995.
- [3] George M. Ware and Christopher I. Cruz, 'Aerodynamic Characteristics of the HL20', Journal of Spacecraft and Rockets, Vol. 30, No.5, September-October 1993.
- [4] Zachary R. Putnam et al, 'Variable Angle-of-Attack Profile Entry Guidance for a Crewed Lifting Body', AIAA [5] K. James Weilmuenster and Francis A. Greene, 'HL-20 Computational Fluid Dynamics Analysis', Journal of Spacecraft and Rockets, Vol. 30, No.5, September October 1993.
- [6] Zhoujie Lyu and Joaquim R. R. A. Martins, 'Aerodynamic Design Optimization Studies of a Blended-Wing-Body Aircraft', DOI: 10.2514/1.C032491, Journal of Aircraft, Vol. 51, No. 5, September-October 2014.
- [7] Dan Almosnino, 'Assessment of an Inviscid Euler-Adjoint Solver for Prediction of Aerodynamic Characteristics of the NASA HL-20 Lifting Body', 23 References <https://www.researchgate.net/publication/303903221>, 34th AIAA Applied Aerodynamics Conference, 13-17 June 2016
- [8] Yongyuan Li and Yi Jiang, 'Shape Design of Lifting body Based on Genetic Algorithm', <http://www.mecs-press.org/>, I.J. Information Engineering and Electronic Business, 1, Pg. No. 37-43, 2010.
- [9] G. M. Ware et al, 'Aerodynamic Characteristics of the HL-20 And HL-20A Lifting Body Configurations', <https://www.researchgate.net/publication/23856704>, AIAA 9th Applied Aerodynamics Conference, September 23-25, 1991.
- [10] E. Bruce Jackson et al, 'Real-Time Simulation Model of the HL-20 Lifting Body', NASA Langley Research Centre, 1992.
- [11] Jeffrey S. Robinson and Kathryn E. Wurster, 'Trajectory and Aero heating

Environment Development and Sensitivity Analysis for Capsule-Shaped Vehicles',
<https://ntrs.nasa.gov/search.jsp?R=20080014105>, NASA Langley Research Centre, AIAA, 2008.

[12] Soumya Dutta et al, 'Mission Sizing and Trade Studies for Low Ballistic Coefficient Entry Systems for Venus',
<https://ntrs.nasa.gov/search.jsp?R=20120006657>, IEEE, 2012.

[13] 'Reusable Launch Vehicle Programs and Concepts', Associate Administrator for Commercial Space Transportation, 1998.

[14] Roger D. Launius and Dennis R. Jenkins, 'Coming Home: Re-entry and Recovery from Space', ISBN 978-0-16-091064-7, NASA Aeronautics Book Series, Library of Congress Cataloguing-in-Publication Data, 2012 [15] Lane E. Wallace, 'Flights of Discovery', The NASA History Series, Library of Congress Cataloguing-in-Publication Data, 1996 24 References.

[16] R. Dale Reed, 'Wingless Flight: The Lifting Body Story', ISBN 0-16-049390, <https://ntrs.nasa.gov/search.jsp?R=19980169231>, The NASA History Series, Library of Congress Cataloguing-in-Publication Data, 1998.

[17] Amanda Deng, 'The Prediction of Aerodynamic Performance and Handling Quality of Spaceship Two Based on the

Analysis of Spaceship One Flight Test Data', 2012.

[18] John C. Adams Jr, 'Atmospheric Re-entry', 2003.

[19] Frank W. Taylor et al, 'Challenges and Opportunities Related to Landing the Dream Chaser Reusable Space Vehicle at a Public-Use Airport', Space Traffic Management Conference, Sierra Nevada Corporation, 2014.

[20] Sneha Deep and G. Jagadeesh, 'Aerothermodynamic effects of controlled heat release within the hypersonic shock layer around a large angle blunt cone', <https://doi.org/10.1063/1.5046191>, American Institute of Physics, 2018.

[21] Selin Aradag et al, 'Aerodynamic Analysis of a Vertical Landing Lifting Body', ISSN 1300-3615, Journal of Thermal Science and Technology, TIBTD, 2015.

[22] Marti Sarigul-Klijn et al, 'Flight Mechanics of Manned Sub-Orbital Reusable Launch Vehicles with Recommendations for Launch and Recovery', <https://www.researchgate.net/publication/237448317>, AIAA, 2003.

[23] Roberta Fusero et al, 'Conceptual design of a crewed reusable space transportation system aimed at parabolic flights: stakeholder analysis, mission concept selection, and spacecraft architecture

definition', DOI 10.1007/s12567-016-0131-7, CEAS, 2016.

[24] Norman Hahn and Cheryl Perich, 'Active Thermal Control System Radiators for the Dream Chaser Cargo System', 48th International Conference on Environmental Systems, 2018 25 References.

[25] Erik Seedhouse, 'Tourists in Space: A Practical Guide', ISBN 978-0-387-74643-2, Praxis Publishing Ltd, 2008.

[26] Erik Seedhouse, 'Virgin Galactic: The First Ten Years', ISBN 978-3-319-09262-1, Springer International Publishing Switzerland, 2015.

[27] Kenneth J. Stroud and David M. Klaus, 'Spacecraft Design Considerations for Piloted Re-entry and Landing', <https://ntrs.nasa.gov/search.jsp?R=20080026216>, 2008.

[28] Borg K. and Matula E., "The SKYLON Spaceplane", University of Colorado, ASEN 5053 – Rocket Propulsion, 2015 .

[29] S. Tauqeer ul Islam Rizvi et al, 'Optimal trajectory and heat load analysis of different shape lifting re-entry vehicles for medium range application', www.sciencedirect.com, Elsevier - Defence Technology 11 (2015) 350e361, 2015.

[30] G. Naresh Kumar et al, 'Re-entry Trajectory Optimization using Gradient Free Algorithms', www.sciencedirect.com,

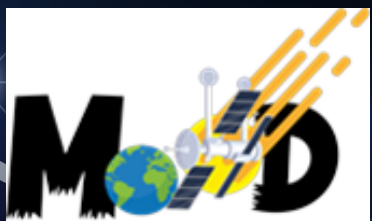
Elsevier - IFAC Papers Online 51-1 (2018) 650–655, 2018.

[31] Guo Jie et al, 'Autonomous gliding entry guidance with geographic constraints', Chinese Journal of Aeronautics, (2015), 28(5): 1343–1354. 2015.

[32] Miroslav P. Pajcin et al, 'Numerical Analysis of Hypersonic Turbulent and Laminar Flow using a commercial CFD Solver', Thermal Science, Vol.20, Suppl. 6, pp. S1- S13, 2016.



COMPARISON BETWEEN MULTIPLE BARE TETHERS AND SINGLE BARE TETHER FOR DEORBITING SATELLITES



**AUGUST
2020**

Comparison between Multiple bare tethers and single bare tether for deorbiting satellites

Internal guide - Komal Kedarnath

External guide - Shreya Santra



Our Team

- 1 adityabhaskaran98@gmail.com
- 2 18103066, Hindustan Institute of Technology and Science, Padur
- 3 4SF17EC008, Sahyadri College of Engineering and Management, Mangalore
- 4 1MV17EE011, Sir M Visvesvaraya Institute of Technology, Bengaluru
- 5 arunadevi.31@outlook.com
- 6 1MS17EC135, M S Ramaiah Institute of Technology, Bengaluru
- 7 18BSR06040, Jain University School of Sciences, Bengaluru
- 8 1915030, K J Somaiya College of Engineering, Mumbai
- 9 N140230, Rajiv Gandhi University of Knowledge Technologies, Nuzvid
- 10 CB.EN.U4AEE19047, Amrita Vishwa Vidyapeetham, Coimbatore

Table of Contents

Our Team	28
List of Figures	31
List of Tables.....	31
List of Symbols	32
Abstract.....	33
Acknowledgement.....	34
1 Introduction	35
2 Methodologies and Theory	36
2.1 Premise.....	36
2.2 Basics of Electrodynamic Tether.....	36
2.3 Debye Length.....	37
2.4 Orbital Motion Limited Theory.....	37
2.5 Effect of Quasi Neutral Plasma on Conductors	37
2.6 Debye Sheath	38
3 Design and Analysis	38
3.1 Force for Constant Current.....	38
3.1.1 Force by a Long Tether.....	38
3.1.2 Force by a Short Tether	39

3.2 Force due to Changing Current	39
3.2.1 Force on a Single Tether due to Changing Current	40
3.2.2 Force on Multiple Tethers due to Changing Current.....	40
3.3 Distance between Adjacent Tethers	41
3.4 De-orbiting Time due to Changing Current	42
4 Results and Conclusions.....	43
5 Future Scope	45
6 Summary.....	45
7 References	45

List of Figures

- 1 Electrodynanic tether and lorentz force[1].
- 2 A tether(blue) placed in plasma(pink) having Debye length (λd)[2].
- 3 Force on a single long tether.
- 4 Force on multiple short tethers.
- 5 Time of de-orbiting versus altitude.

List of Tables

- 1 Table relating Debye length, sheath radius and spacing distance with different altitudes
- 2 Table relating the time that each object would take to de-orbit from its own orbit to 200km altitude, for given characteristics.

List of Symbols

Symbol	Connotation	Value
B	Magnetic Field of the Earth	$2.5 \times 10^{-5} Wm^{-2}$
G	Universal Gravitational Constant	$6.673 \times 10^{-11} Nm^2 kg^{-2}$
M	Mass of Earth	$6.4 \times 10^{24} kg$
v	Velocity	
ψ	Induced Voltage	
I	Current	
R_{net}	Resistance of the Tether	
ρ	Resistivity	
A	Area of Cross Section of Tether	
d	Spacing Distance	
F_t	Force Produced by Tether	
m_{ion}	Mass of Ion	
m_e	Mass of Electron	$9.1 \times 10^{-31} kg$
E_{mag}	Work Done by Electromagnetic	
m_t	Work Done by the Tether	
w_{grav}	Work Done Due to Gravity	
m_{tot}	Mass of the Satellite	
x_d	Debye Length	
e_d	Sheath Thickness	

Abstract

This paper compares the working of multiple bare electrodynamic tethers versus a long single tethered system on a satellite in Low Earth Orbit(LEO) for end of life de-orbiting to combat the further formation of space debris. The paper demonstrates the use of several equal length short tethers, placed in parallel orientation on one face of the satellite. Tethers have proved to be efficient passive de-orbiting systems, yet tethers used in previous missions have been subjected to damage due to their extremely large lengths. The paper also upholds the fact that the same drag force can be produced using multiple tethers just like a single long tether. The calculation of de-orbiting time is presented along with the effects of initial induced voltage and current. To obtain the maximum efficiency from each short tether optimum spacing distances between the tethers are also presented.

Acknowledgement

We would like to express our profound gratitude and deep regards to our internal guide Mr.Komal Kedar, external guide Ms. Shreya Santra, Mr. Pavan Kumar, Mr. Sujay Sreedhar and Ms.Nikitha and each and every one at Society for Space Education Research and Development(SSERD) for their exemplary guidance, monitoring, constant encouragement, timely help and advice throughout the course of this project.

We are extremely grateful for their confidence in us and our project, entitled "Mitigation of Orbital Debris". At this juncture, we feel honoured in expressing our sincere thanks to our mentors for making the resources available at the right time and providing valuable insights leading to the successful completion of our project.

I Introduction

Orbital debris is one of the major issues in the field of space technology, which includes uncontrollable objects in space. Anybody or particle that is uncontrollable or has been left defunct constitute space debris. This includes, paints, gases, tools, and destroyed rockets and satellites. They not only pose a major threat to the existing assets in space but also affect future missions too. According to the National Space Society (NSS), there are about 22,000 Earth-orbiting debris pieces that are larger than 10cm size, around 7,00,000 fragments between 1cm and 10cm range, and the number of tiny bits that are smaller than 1cm exceeds 100 million [3].

Orbital debris persist in space due to the lack of on-board de-orbiting mechanisms that could dispose of the satellite at the end of the mission. These abandoned satellites have no control over their trajectories and hence can lead to collisions resulting in the generation of more debris. Inter-Agency

Space Debris Coordination Committee (IADC) has made guidelines that any object put into Low Earth Orbit (LEO) should not have an orbital lifetime for more than 25 years post the end of its useful life [4]. Hence several institutions and organizations have proposed and tested different de-orbiting mechanisms[5].

de-orbiting mechanisms can be of two types, active and passive. Passive de-orbiting mechanisms do not require a power supply from the spacecraft, need no monitoring, and also can perform re-entry more effectively. Among passive de-orbiting mechanisms, electrodynamic tethers (EDT) are one of the most effective systems. This study focuses on the physics behind electrodynamic tethers, while addressing a possible solution for optimization of its length. The length of single tethers is proposed to be reduced by replacing it with a set of multiple short tethers, without affecting much of its intended performance.

2 Methodologies and Theory

2.1 Premise

For the purpose of this study, the magnetic field of the Earth is considered to be constant along the orbit and altitude of consideration. The variation of solar irradiance is ignored as the satellite is within the bounds of Van Allen belt. The orbits are considered to be equatorial and circular in LEO. The oblateness of the Earth is ignored. The ambient plasma condition in the ionosphere is considered to be quasi-neutral. Only prograde satellites are being considered. The study considers microsatellite of a mass of 100kg. If found effective, this mechanism of multiple tethers can be implemented for various classes of satellites. The study looks into the performance of the tether system in orbit, and does not consider the structural properties of the system.

2.2 Basics of Electrodynamic Tether

EDT works on the principle of electro-motive force the presence of the magnetic field of the Earth induces a current in the conductor (the tether), that moves relative to it. The motion of the satellite is from west to east i.e., eastward. The tether is

deployed from the satellite in the direction radially towards the Earth. When a conductor is moved in a magnetic field with some relative velocity such that it cuts the field lines, voltage is induced in the conductor as a consequence. The induced voltage in the tether (ψ) can be obtained from the cross product of the velocity of the tether (v) and the magnetic field (B) where the direction will be radially away from the Earth as given by the below equation:

$$(\psi) = \int_0^L (v \times B) dl = vBL \sin \theta,$$

where L is the length of the tether and θ is the angle between the direction of velocity and direction of the magnetic field.

Hence the current (I) induced due to the induced voltage(ψ) will also be in the direction away from the Earth given by

$$I = \frac{\psi}{R_{net}} = \frac{vBL}{R_{net}},$$

where R_{net} is the resistance of the tether.

The Lorentz force (Ft) produced by the induced current (I) is given by the below expression where its direction will be opposite to that of the velocity of the satellite and thus help in reducing the orbit altitude gradually.

where α is the angle between the direction of current and magnetic field.

In this method the EDT can be used to de-orbit a satellite from the orbit. The induced

voltage produces a current in the tethers, a complete path of current is formed in the ambient plasma with help of contactors, which act as electron flow medium between the tethers and the ambient plasma. This current in the tether is responsible for producing the required force, the drag force, for de-orbiting.

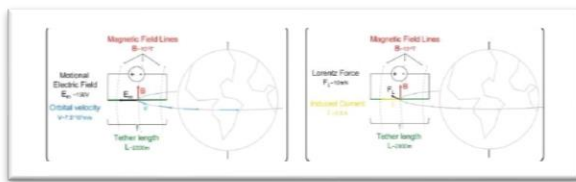


Figure 1: Electrodynamiic tether and lorentz force[1]

2.3 Debye Length

Debye length is the measure of the net electrostatic effect of charge carriers in a solution and how far its electrostatic effect persists. Debye length is denoted by λ_d , it can be defined as the decrease in the magnitude of the electric field by a factor of $1/e$, where e is the charge of the electron.

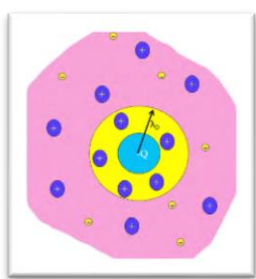


Figure 2: A tether(blue) placed in plasma(pink) having Debye length (λ_d)[2]

2.4 Orbital Motion Limited Theory

According to Orbital Motion Limited (OML) theory[6], the orbital-motion-limit regime is attained when the cylinder radius is small enough such that all incoming particle trajectories that are collected are terminated on the cylinder's surface while being connected to the background plasma. In an electrodynamic tether system and for a given mass of tether, the best performance is achieved for a tether diameter chosen to be smaller than 1 electron Debye length, for typical ionospheric ambient conditions from 200 to 2000 km altitude range.[7]

2.5 Effect of Quasi Neutral Plasma on Conductors

Consider a plasma which has an equal number of electrons and ions. Let a conducting metal wire be placed inside the plasma. It is observed that a sheath gets formed around this conducting surface. The sheath arises because of the following reasons. The electrons usually have a temperature of the order equal to or greater than that of the ions, and electrons are comparatively very light than ions. Speed of electrons is greater than speed of ions by a factor of $\sqrt{\frac{m_{ion}}{m_e}}$, where m_{ion} is the mass of ion and m_e is the mass of electron.

As the plasma is considered as neutral plasma, with the assumption that the

number of electrons and the number of ions in the plasma is about 100, due to the high speed of the electrons for every 1 ion collision with the surface of the conductor, there would have been 100 electrons that would have collided with the surface. Due to this movement of electrons and ions, the surface of the tether gets negatively charged and due to the electrostatic force of attraction, positive ions get accumulate around the metal surface to balance the negative charge on the surface. This layer is called the Debye sheath.

2.6 Debye Sheath

Debye sheath is a layer in plasma which has a greater density of positive ions, and hence an overall excess positive charge, that balances an opposite negative charge on the surface of a material with which it is in contact. The thickness of this layer can be several “Debye length” thick, a value whose size depends on various characteristics of plasma, like temperature, density, etc.[8] This formula gives the sheath thickness in terms of Debye length.

$$\epsilon_d = \frac{d}{\lambda_d} = \left(\frac{1}{c_1} \ln \left[\sqrt{\frac{m_{ion}}{2\pi m_e}} \right] \right)^{3/4} \quad (1)$$

where d is the sheath thickness.

3 Design and Analysis

3.I Force for Constant Current

Consider a tether of length L and let voltage induced by this tether be

$$\psi = \int_0^L (v \times B) dl,$$

where v is the velocity of the satellite and B is the magnetic field of earth. By integrating, the following equation is obtained,

$$\psi = vBL,$$

where L is the length of a single tether. Now consider a short tether of length L/N, keeping the material and the area same.

The induced voltage is,

$$\begin{aligned} \psi' &= \int_0^{L/N} (v \times B) dl \\ \psi' &= \frac{vBL}{N}, \\ \psi' &= \frac{\psi}{N}. \end{aligned} \quad (2)$$

So, the length of the tether affects the voltage induced by the tether.

3.I.I Force by a Long Tether

The force acting on the tether is

$$F_t = \int_0^L (I \times B) ds,$$

which, when integrated gives,

$$F_t = BIL \sin(\theta),$$

where θ is the angle between direction of current I and magnetic field B. The tether is

placed perpendicular to the direction of magnetic field of Earth, therefore $\theta = 90^\circ$ and voltage is given by

$$\psi = IR_{net},$$

where R_{net} is the net resistance of the tether.

$$I = \frac{\psi}{R_{net}},$$

And

$$R_{net} = \frac{\rho L}{A},$$

where ρ is the resistivity of the tether and A is the cross-sectional area of tether.

Therefore, force produced by the tether is

$$F_t = \frac{B\psi L}{\frac{\rho L}{A}} \\ F_t = \frac{B\psi A}{\rho}. \quad (3)$$

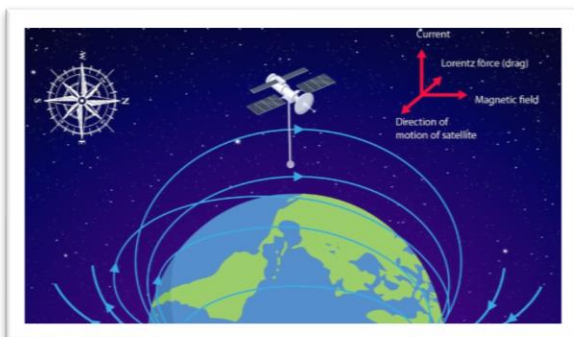


Figure 3: Force on a single long tether

3.I.2 Force by a Short Tether

Since the tethers are placed parallel to each other and the force is in the same direction, the force for a shorter tether of length L/N is,

$$F_i = \int_0^{L/N} (I \times B) ds,$$

where I is current and B is magnetic field.

Now by integrating,

$$F_i = \frac{B\psi' A}{N\rho} \\ F_i = \frac{F_t}{N}. \quad (4)$$

As the induced voltage reduces due to reduce in length, the force also reduces.

But when there are N such short tethers, the force is same as that due to single long tether

$$F_{tm} = F_t \quad (5)$$

Therefore, the force produced by a single tether is equal to the force produced by multiple tethers whose lengths sums up to the length of the single tether.

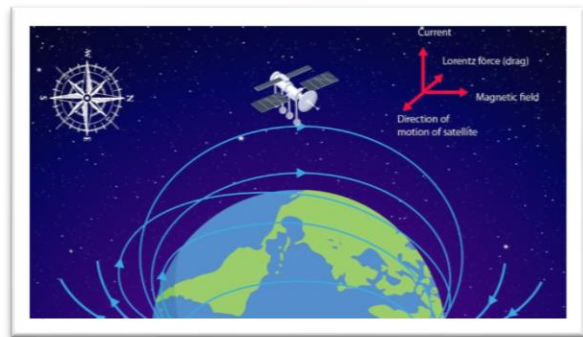


Figure 4: Force on multiple short tethers

3.2 Force due to Changing Current

The previous section derived the force for a constant current condition. But since the current changes throughout the process of de-orbiting, so will the force. Hence, the force produced is modelled as follows.

3.2.1 Force on a Single Tether due to Changing Current

By lorentz force,

$$F_t = BI(t)L,$$

$$\frac{dF_t}{dt} = BL \frac{dI}{dt} \quad (6)$$

$$\frac{dI}{dt} = \frac{d\varphi}{dt} \frac{1}{R_{net}} \quad (7)$$

By Faraday's law of electromagnetic induction, induced voltage is given by,

$$\frac{d\varphi}{dt} = LB \frac{dv}{dt} \quad (8)$$

By Newton's second law of motion,

$$\frac{dv}{dt} = -\frac{F_t}{m_{tot}} \quad (9)$$

From 6 7, 8 and 9

$$\frac{dF_t}{dt} = -\frac{B_2 L^2 F_t}{m_{tot} R_{net}}$$

Transposing the terms (9)

$$\frac{dF_t}{F_t} = -\frac{B^2 L^2 dt}{m_{tot} R_{net}}$$

Integrating on both sides from $t_0 = 0$ to t and force $F_t = F_0$ when $t_0 = 0$

$$\ln \frac{F_t}{F_0} = -\frac{B^2 L t}{m_{tot} R_{net}}$$

$$\frac{F_t}{F_0} = e^{\frac{-B^2 L^2 t}{m_{tot} R_{net}}} \quad (10)$$

At $t = t_0$, $F_t = F_0$ and $I = I_0$, hence,

$$F_0 = BI_0 L,$$

And,

$$I_0 = \frac{v_0 B L}{R_{net}},$$

$$v_0 = \sqrt{\frac{GM}{r_0}},$$

$$I_0 = \frac{BL}{R_{net}} \sqrt{\frac{GM}{r_0}},$$

Therefore 10

becomes,

$$F_t = \frac{B^2 L^2}{R_{net}} \sqrt{\frac{GM}{r_0}} e^{\frac{-B^2 L^2 t}{m_{tot} R_{net}}} \quad (11)$$

This is the force produced by a single tether of length N due to changing current.

3.2.2 Force on Multiple Tethers due to Changing Current

By lorentz force,

$$F_i = \frac{BI_i L}{N},$$

where F_i is the lorentz force and I_i is the current in a single short tether.

$$\frac{dF_i}{dt} = B \frac{L}{N} \frac{dI_i}{dt}. \quad (12)$$

$$\frac{dI_i}{dt} = \frac{d\psi_i}{dt} \frac{N}{R_{net}}. \quad (13)$$

$$\frac{d\psi_i}{dt} = \frac{BL}{N} \frac{dv_N}{dt}. \quad (14)$$

$$\frac{dv_N}{dt} = -\frac{F_{tm}}{m_{tot}} = -\frac{NF_i}{m_{tot}} \quad (15)$$

where F_{tm} is the force by multiple tethers.

From 12,13,14 and 15

$$\frac{dF_i}{dt} = -\frac{B^2 L^2 F_i}{m_{tot} R_{net}}. \quad (16)$$

By transposing the terms,

$$\frac{dF_i}{F_i} = -k dt$$

$$\text{Where } k = \frac{B^2 L^2}{m_{tot} R_{net}}.$$

Integrating both sides from F_0 to F_i and t is from 0 to t

$$\begin{aligned}\ln \frac{F_i}{F_{i0}} &= -kt, \\ F_i &= F_{i0}e^{-kt}, \\ F_{i0} &= \frac{BLI_{i0}}{N}, \\ I_{i0} &= \frac{v_0 B \frac{L}{N}}{\frac{R_{net}}{N}}, \\ F_{i0} &= \frac{B^2 L^2 v_0}{NR_{net}} = \frac{F_0}{N}.\end{aligned}$$

Therefore,

$$F_{tm} = \frac{F_0 e^{-kt}}{N} N.$$

But there are N such tethers and their individual forces act on the same satellite in the same direction. Therefore,

$$F_{tm} = F_t \quad (17)$$

Thus, all calculations henceforth will have the bearing for both single tethered system as well as multiple tethered system. Which implies that the de-orbiting time by single tether and multiple tether are the same.

3.3 Distance between Adjacent Tethers

Consider a condition where two conductors are placed in the plasma in proximity of each other, a positive ion sheath is formed over the conductors. When the spacing between the two conductors is less than the minimum required spacing, the net positive ions around each conductor reduces as there will be interference with the sheath of adjacent conductors. This results in the distribution of positive charges between the interfering sheaths. The reduction of positive ions in the sheath will in return

reduce the number of electrons on the sheath-contact surface of the conductor resulting in the reduction of the current in the individual conductor. Hence, if each of the tethers is placed outside the sheath radius of its adjacent tether, there will not be any reduction of induced current.

Maintaining a minimum spacing of twice the sheath radius of the individual tether will prevent any loss of performance, as there will be no interference between the sheath of adjacent tethers. The following table is one such example. Here oxygen ions have been taken where its mass is

$$m_{ion} = 16.022 \times 10^{23},$$

The constant

$$C_1 = 1.36.$$

Thus from 1, $d = 3.39\lambda_d$.

$$\frac{d\psi}{dt} = LB \frac{dv}{dt}. \quad (20)$$

Altitude (km)	$4\lambda_d(\text{mm})$	Sheath thickness d(mm)	Spacing distance
650	7.25	24.57	49.14
700	8.25	27.967	55.93
750	8.5	28.815	57.63
800	8.5	28.815	57.63
850	9.75	33.052	66.104
900	12.25	41.527	83.054
950	13.75	46.612	93.224
1000	16	54.24	108.48

Table 1: Table relating Debye length, sheath radius and spacing distance with different altitudes

(The first 2 columns of the table are from effects of electron emission on plasma sheaths [8])

3.4 De-orbiting Time due to Changing Current

By lorentz force,

$$\frac{dF_t}{dt} = BL \frac{dI}{dt}, \quad (18)$$

$$\frac{dI}{dt} = \frac{d\psi}{dt} \frac{1}{R_{net}} \quad (19)$$

By Faraday's law of electromagnetic induction, induced voltage is,

By Newton's second law of motion,

$$\frac{dv}{dt} = -\frac{F_t}{m_{tot}}. \quad (21)$$

From 18, 19, 20 and 21

$$\frac{dF_t}{dt} = -\frac{B^2 L^2 F_t}{m_{tot} R_{net}}.$$

By transposing terms,

$$\frac{dF_t}{F_t} = -\frac{B^2 L^2 dt}{m_{tot} R_{net}}.$$

Integrating on both sides from $t_0 = 0$ to t and force $F_t = F_0$ when $t = t_0$

$$\ln F_t - \ln F_0 = -\frac{B^2 L^2 (t - t_0)}{m_{tot} R_{net}}$$

$$F_t = F_0 e^{-kt},$$

$$\text{Where } k = \frac{B^2 L^2}{m_{tot} R_{net}}$$

$$F_0 = BL I_0,$$

$$I_0 = \frac{\psi_0}{R_{net}},$$

$$\psi_0 = v_0 BL,$$

$$F_0 = \frac{B^2 L^2 v_0}{R_{net}},$$

$$v_t = v_0 + \frac{F_0 e^{-kt}}{km_{tot}} - \frac{F_0}{km_{tot}}$$

As $F_0 = k v_0 m_{tot}$,

$$r_t = r_0 - \frac{F_t}{k^2 m_{tot}},$$

$$\frac{dE_{mag}}{dt} = F_t v_t + \frac{dF_t}{dt} \int v_t dt.$$

$$\text{Power} = \frac{F_t^2}{km_{tot}} - k F_t r_0 + \frac{F_t^2}{km_{tot}}.$$

Integrating on both sides from $t_0 = 0$ to t , so

F from F_0 to F_t and r from r_0 to r_t

$$W_t = -F_t r_0 - \frac{F_t^2}{k^2 m_{tot}} + F_0 r_0 + \frac{F_0^2}{k^2 m_{tot}},$$

$$W_t = F_0 r_0 (1 - e^{-kt}) + \frac{F_0^2}{k^2 m_{tot}} (1 - e^{-2kt}).$$

By substituting $F_0 = k v_0 m_{tot}$,

$$\begin{aligned} W_t &= v_0^2 m_{tot} \left[\frac{k r_0}{v_0} (1 - e^{-kt}) + (1 - e^{-2kt}) \right]. \\ W_{grav} &= \left(\frac{GMm_{tot}}{r_t^2} - \frac{m_{tot}v_t^2}{r_t} \right) r_t - \left(\frac{GMm_{tot}}{r_0^2} + \frac{m_{tot}v_0^2}{r_0} \right) r_0 \\ W_{grav} &= \frac{GMm_{tot}}{r_t} - m_{tot}v_t^2 - \frac{GMm_{tot}}{r_0} + m_{tot}v_0^2. \\ W_t &= k v_0 m_{tot} r_0 (1 - e^{-kt}) + \frac{k^2 v_0^2 m_{tot}^2}{k^2 m_{tot}} (1 - e^{-2kt}) \\ W_t &= k v_0 m_{tot} r_0 (1 - e^{-kt}) + \frac{k^2 v_0^2 m_{tot}^2}{k^2 m_{tot}} (1 - e^{-2kt}), \quad (22) \end{aligned}$$

Orbital velocity at an orbit orbit of radius r_0 is $v_0 = \sqrt{\frac{GM}{r_0}}$,

$$W_{grav} = \frac{GMm_{tot}}{r_t} - m_{tot}v_t^2,$$

$$\begin{aligned} W_{grav} &= v_0^2 m_{tot} \left[\frac{r_0}{r_t} - 1 \right] \\ W_t &= W_{grav}, \quad (23) \end{aligned}$$

$$\frac{r_0}{r_t} - 1 = \frac{k r_0}{v_0} (1 - e^{-kt}) + 1 - e^{-2kt} \quad (24)$$

By solving this equation using the above-mentioned software some inferences were derived which are explained in the next section.

4 Results and Conclusions

Graphs were plotted for the following sample data for three separate objects.

Object	Mass (in kg)	Length (in km)	Total resistance of tether(in kΩ)
Object 1	100	10	1
Object 2	100	1	1
Object 3	10	10	1

It can be observed that the de-orbiting time, as a result of the force produced by the tethers, decreases, from higher altitudes to 200km above the Earth's surface.

It can also be observed that the multiple tethers do not affect the de-orbiting time as the total force produced multiple tethers, F_t , is same as that of a single tether and even the velocity v_t expression remains the same.

The Energy is only dependent on the above-mentioned variables and other common arbitrary and prespecified constants r_0 , m_{tot} , etc. which are taken to be equal for

comparison purposes owing to same initial conditions.

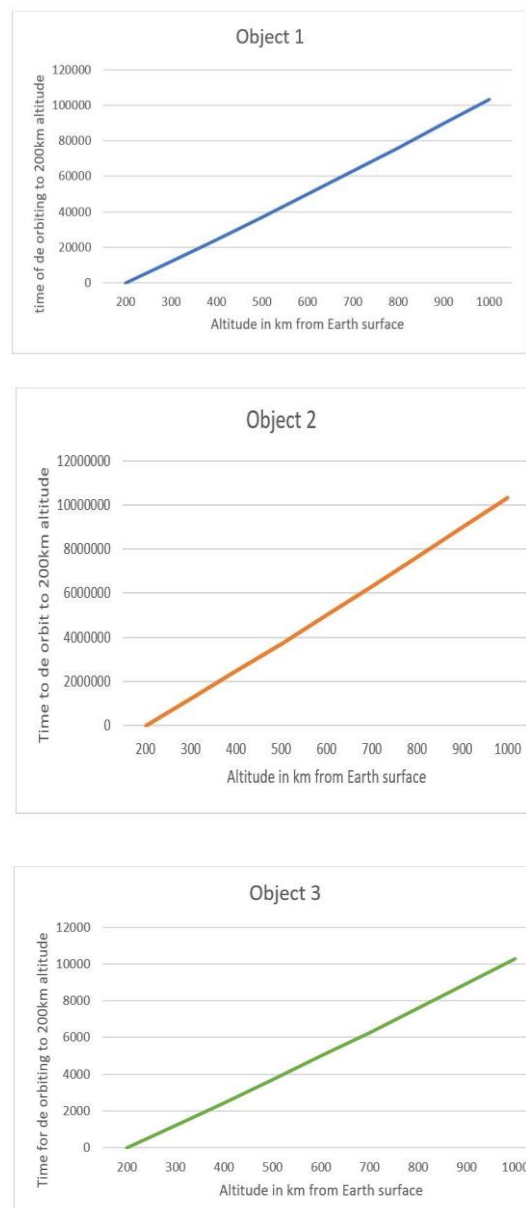
Altitude in km	Object-1 time (in s)	Object-2 time (in s)	Object-3 time (in s)
200	0	0	0
300	12210	1221000	1218
400	24610	2462000	2455
500	37210	3722000	3711
600	50000	5001600	4986
700	63000	6302500	6283
800	76220	7624800	7600
900	89660	8969400	8939
1000	103300	10337000	10300

Table 2: Table relating the time that each object would take to de-orbit from its own orbit to 200km altitude, for given characteristics.

Notice that as the Keplerian orbit being considered from 200km altitude initially, yields 0 de-orbiting time, as it is already there at the required resultant position.

The de-orbiting time was calculated by plotting the total energy expression on Desmos (<https://www.desmos.com/calculator>), an online graphing

calculator, against the X axis of time, and finding the root of the constraint, which would give us the de-orbiting time when the net condition of W_t and W_{grav} would be equal, their difference being 0. Thus, the value of the X intercept by the function of total work-energy, yields us the solution required.



(a) Object 1 (b) Object 2 (c) Object 3

Figure 5: Time of de-orbiting versus altitude

From the graphs, we can see that the nature of variation of de-orbiting time with initial altitude is similar in nature to that of the other objects.

5 Future Scope

From past papers and by observing the properties of multiple conductors in quasi-neutral plasma, this paper uses the Child Langmuir equation to calculate the thickness of the sheath around multiple tethers and has theoretically proposed the concept of optimum distance between two tethers. Experimental results need to verify this proposal and conclude the optimum distance between the tethers. The sheath to sheath interactions is also open for experimental verification, which can provide greater insight into the behaviour of plasma itself. A setup can be demonstrated to develop and verify short multiple tethers, whose length sums up to be equal to the length of a single long tether can produce the same force can also be verified. Apart from the experimental analysis of the deployment mechanics required for multiple tethers, the circuitry of the contactors can begin the era of multiple tethers for future de-orbiting mechanism. This paper extensively works with the consideration of microsatellites for analysis, if efficient

enough multiple tethers can be modulated to all classes of satellites.

6 Summary

The paper provides an introductory analysis of the concept of using multiple tethers rather than a single long tether to produce the required drag force to de-orbit a satellite.

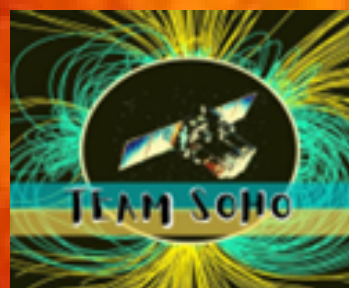
The paper also introduces the concept of optimum distance between the tethers so as to avoid any interactions between the plasma sheaths of the multiple tethers. It is essential that the multiple tethers need to place at appropriate distances to produce the same electrodynamic drag forces as a long tether to de-orbit the satellite within the same de-orbiting time with a single large tether. The plasma sheath to sheath interactions, though, having not much available literature, has been excluded from consideration.

7 References

- [1] Gonzalo Sanchez-Arriaga, Gabriel Motta, Enrico Lorenzini, Lorenzo Tarabini Castellani, and Martin Tajmar. Low work-function tether deorbit kit. 12 2019.

- [2] James Creel. *Characteristic measurements within a GEC rf Reference Cell.* PhD thesis, 08 2010.
- [3] Orbital debris: Overcoming challenges. National Space Society, 2016.
- [4] M Yakovlev. The “iadc space debris mitigation guidelines”and supporting documents. In *4th European Conference on Space Debris*, volume 587, 2005.
- [5] Gonzalo Sanchez-Arriaga, J.R. Sanmartín, and Enrico Lorenzini. Comparison of technologies for deorbiting spacecraft from low-earth-orbit at end of mission. *Acta Astronautica*, 138, 09 2017.
- [6] Xian-Zhu Tang and Gian Luca Delzanno. Orbital-motion-limited theory of dust charging and plasma response. *Physics of Plasmas*, 21(12):123708, 2014.
- [7] Keith Fuhrhop. *Theory and Experimental Evaluation of Electrodynamic Tether Systems and Related Technologies.* PhD thesis, 01 2007.
- [8] Samuel J. Langendorf. Effects of electron emission on plasma sheaths. 2015.

**TO DEVELOP A PREDICTIVE MODEL FOR THE ENERGY
OF SOLAR FLARES USING MACHINE LEARNING AND
TO FIND THE CORRELATION BETWEEN SUNSPOT AREA
AND RELATED PARAMETERS**



AUGUST 2020

To develop a predictive model for the energy of Solar Flares using Machine Learning and to find the correlation between Sunspot Area and related parameters.

Internal guide - Sundar
External guide - Dr. Parshati Patel



Our Team

1. Adhitya Shreyas SP, RA1811019010006, SRM Institute of Science and Technology, Kattankalathur.
2. Amaria Bonsi Navis. I, 170046, Holy Cross College Nagercoil.
3. Anisha, 18582042, Kalindi College New Delhi.
4. Ankit Kumar Mishra, 11703983, Lovely Professional University Punjab.
5. Apeksha Mahesh Phadte, 201810848, PES RSN College of Arts and Science Goa University, Goa.
6. Arvindh E. Prasad, RA1811019010001, SRM Institute of Science and Technology, Kattankalathur.
7. Athuliya A, 721017101011, Nehru institute of technology, Coimbatore.
8. Kritika Joshi, 19MS0053, IIT(ISM) Dhanbad.
9. Megha Madhusudhan, RV18S1183, NMKRV College for Women, Bangalore.
10. Prateek Boga, 122017009, SASTRA University Thanjavur, Hyderabad.
11. Priyanka Kasturia, 18567021, kalindi college, Delhi.
12. R. Aparna, RA1811019010031, SRM Institute of Science and Technology, Chennai.
13. Renuka Velu, 17PHY28, Bhaktavatsalam Memorial College, Chennai.

Contents

Our Team.....	49
Acknowledgements	54
Abstract.....	55
1 Introduction	56
1.1 Aims and Objectives	56
1.1.1 Objective I: To develop a predictive model for the energy of solar flares with the help of Machine Learning.	56
1.1.2 Objective II: To find an inverse correlation between the sunspot area and solar activity.....	57
2 Background & Literature Overview	57
2.1 Magnetic Field of the Sun.....	57
2.2 Sunspots.....	58
2.3 Solar Flares	59
2.4 Coronal Mass Ejections	60
2.5 Total Solar Irradiance (TSI).....	61
2.6 Machine Learning	61
2.7 Curve fitting.....	62
2.8 Scatterplot Matrix	63

2.9 Ensembled Methods	63
3 Methodology & Data Collection	64
3.1 Objective I: To develop a predictive model for the energy of solar flares using machine learning	64
3.1.1 Generated code from Regression Learner App:	66
3.1.2 Code for same model without using Regression Learner App:	69
3.1.3 Output for hyperparameter optimization:	70
3.2 Objective II: To find an inverse correlation between the sunspot area and solar activity	70
3.2.1 Averaging code	70
3.2.2 Code to sort the data to SSN ranges	71
3.2.3 Magnetic flux code.....	72
3.2.4 Data extraction code.....	73
3.2.5 Plotting and curve-fitting code.....	74
4 Results & Discussion	75
4.1 Objective I: To develop a predictive model for energy of solar flares using Machine Learning.....	75
4.1.1 Prediction model for Solar Flare:	75
4.1.2 LS boost optimizable ensemble regression model.....	75
4.1.3 Model type:	75

4.1.4 Optimized Hyperparameters	75
4.1.5 Hyperparameter Search Range	76
4.1.6 Optimizer Options.....	76
4.1.7 Feature Selection	76
4.1.8 SFI vs Magnetic Flux Density	76
4.2 Objective II: To find the correlation between sunspot area and related parameters	80
4.2.1 Number of Solar Flares v/s SSA:	80
4.2.2 Solar Flare Index v/s SSA:.....	81
4.2.3 Total Solar Irradiance v/s SSA:.....	82
4.2.4 CME Width v/s SSA:	83
4.2.5 Linear speed v/s SSA:	84
4.2.6 2nd order Initial Speed v/s SSA:.....	85
4.2.7 2nd order Final Speed v/s SSA:	86
5 Conclusions	87
5.1 Objective I:To develop a predictive model for the energy of Solar Flares using Machine Learning	87
5.2 Objective II : To find the correlation between Sunspot Area and related parameters	88
5.3 Future Scope	88

5.3.1 Objective I:To develop a predictive model for the energy of Solar Flares using Machine Learning.....	88
5.3.2 Objective II: To find the correlation between Sunspot Area and related parameters	89
6 References	89
6.1 Background & Literature survey.....	89

Acknowledgements

We'd like to firstly express our utmost gratitude to SSERD for giving us this unique opportunity of a research internship which has enhanced each and every one of us in both, an individualistic and collective sense due to the immense exposure, knowledge and fun we've had due in the short duration of a month. The SSERD team has been extremely helpful by providing us a user-friendly and safe platform where communication between us was made easy. The constant support we received from Ms. Nikhitha, Mr. Sujay Sreedhar, Mr. Komal Kedarnath and Mr. Mahesh have been a great source of motivation and driven us to accomplish our goal. The weekly update meetings that were conducted helped us to analyse our weekly progress.

The technical talks that were conducted twice a week helped us gain knowledge and has taught us valuable lessons in terms of career growth. We are also extremely thankful to our mentors Mr. Sundar and Dr. Parshati Patel for their valuable inputs in every step of the way. Their guidance and patience with us throughout have been supremely helpful for this was a learning process for all of us. Mr. Sundar has never once hesitated to help us with our queries irrespective of how late at night it may be and we are so very thankful for that. Mr. Pavan Kumar has also been kind enough to help us whenever we had doubts and wanted to verify our proceedings. We are grateful for each and every person that has made this possible and are looking forward to make use of this whole experience to grow in our careers!

Abstract

We have studied the long-term variation of various solar parameters and aimed at making a predictive model for solar flares using parameters that influence solar flare activity, and also to find a correlation between different parameters of Coronal Mass Ejections (CMEs). The analysis of the predictive model was performed an R-square value of 0.79 and RMSE value of 2.9653 was obtained which pertains to the fact that the model fits. A detailed correlative study has been performed using the monthly data among a variety of solar activity parameters like CME width, Number of Solar Flares, Linear Speed of CMEs, Solar Flare Index, 2nd order Initial and Final Speeds of CMEs and Total Solar Irradiance. The Correlation analysis was performed by studying the Spearman coefficient obtained by plotting and curve fitting graphs for various CME parameters with respect to Sunspot Number ranges and Magnetic Flux differences. It was concluded that the relation between the parameters and the Sunspot Area was an inverse relation where the coefficient values with the MF difference were negative and for the parameters that didn't yield a negative coefficient was an effect of magnetic flux and the anomalies observed were due to lack of data.

I Introduction

The involvement of a strong magnetic field at localized regions (called active regions) in the atmosphere of the sun gives rise to different dynamic and spatially confined phenomena. These are sunspot groups, faculae, plages, filaments or prominences (when viewed on the solar disk or the solar limb respectively), flares, coronal mass ejections (CMEs), Solar winds, coronal loops, Solar Energetic Particles (SEPs), etc. The active regions are the areas of strong magnetic fields where the bundles of these field lines extend above the photosphere and form into the loops in the solar atmosphere. Thus, the sun displays a few or all phenomena in the active regions.

One such solar activity is the sunspots, which are the temporary dark spots on the solar photosphere, from which, most of the solar flares and Coronal Mass Ejections originate. It is reasonable to study the sunspot parameters like sunspot numbers(SSN) and sunspot area(SSA) as they are crucial in the study of solar activities. On the other hand, Solar flares are the intense burst of the radiations due to the sudden release of the energy stored in the magnetic fields, and the Solar Flare Index (SFI) is one of the considered parameters to get the rough measurement of their energy.

The cause of these phenomena is the magnetic field. But there are different parameters such as kinetic energy of CMEs, shear angles, differential rotations, solar cycle, flux densities, irradiance, CME speed parameters, etc. that are essential to look upon for studying these phenomena. Python programming, MATLAB, Supervised Machine Learning, and Ensemble modelling were useful in data analysis, graphs plotting, curve fitting and developing a predictive model.

I.I Aims and Objectives

I.I.I Objective I: To develop a predictive model for the energy of solar flares with the help of Machine Learning.

Solar flares are the most well-known phenomenon, which is a part of the 11-year solar activity cycle with increasing and decreasing the number of sunspots on the Sun. These sunspots can be tens of thousands of kilometres across. The number of sunspots peak during the solar maxima and are generally closer to the Sun's equator.

These solar flares are accompanied by huge amount of high energy proton and electron ejections exceeding the normal solar winds. It is part of the solar weather and at their peak, could harm satellites due to its excessive magnetic field interactions. Solar flares Index of solar flares depends on

various parameters but the most important and easily accessible are Magnetic flux density, sunspot number and sunspot area.

Linking all these parameters would create a better understanding of Solar flares and would create a new perspective to the study of the Sun. The data from this was taken and put into machine learning algorithms to acquire desirable results.

I.I.2 Objective II: To find an inverse correlation between the sunspot area and solar activity.

The cause of solar activity in sun is its complex magnetic field and phenomena relating to it i.e. loop formations, magnetic reconnection etc.

Solar activities like solar flares, coronal loops, CMEs are directly related to sunspot formations. The hypothesis is based on a very basic properties of magnetic field lines.

They don't intersect each other

The magnetic strength is stronger where the lines are near to each other.

This suggests that for a sunspot with a lesser area, the field lines will be confined to a smaller region which means that the magnetic field strength at that region will be higher.

Hence, the possibility of occurrence of Solar activities are more if the SSA is less. To understand this phenomenon, observation

of one particular sunspot has to be done, which is difficult. Overall solar activity and magnetic field strength can be observed and analysis can be done. However, there are other factors affecting the magnetic field strength. At an instance, if number of sunspots are different, the strength is bound to vary. Hence, instances of same/similar SSN are to be considered.

Similarly, even with the same SSN values, the magnetic flux from a particular sunspot might vary. Thus, instances are to be refined further to ones with same/similar magnetic flux. At last, the parameters of solar activity are to be compared with SSA of refined time periods with same SSN and same magnetic flux.

2 Background & Literature Overview

2.I Magnetic Field of the Sun

The presence of the electric current within the surface of the sun generates the magnetic field, which further causes various activities such as sunspots, solar flares, coronal mass ejections, solar winds, etc. at the solar surface in a regular cycle of 11-years, called the solar cycle. Comparable to the bar magnet, the sun's magnetic field has two poles that flip at the peak of each solar activity cycle.

Plasma, the main constituent of the sun, a gas-like state of matter in which electrons and ions are separated, creating a super-hot mix of charged particles. When charged particles move, they naturally create magnetic fields, which in turn have an additional effect on how the particles move. The plasma in the sun, therefore, sets up a complicated system of cause and effect in which plasma flows inside the sun, churned up by the enormous heat produced by nuclear fusion at the centre of the sun, thus creating the sun's magnetic fields.

The differential rotation, which is the rotation of the solar surface at different speeds depending on the latitude, increases the complexity of the solar magnetic field. Differential rotation (DR) is a powerful generator of magnetic fields, and therefore, a key ingredient in stellar dynamo models. The surface DR of the sun has been known for a long time from the tracking of sunspots.

The strongest magnetic field regions are in sunspots, reaching field strengths of $B = 2000\text{--}3000 \text{ G}$. Active regions and their places comprise a larger area around sunspots with average photosphere fields of $B \approx 100\text{--}300 \text{ G}$, containing small-scale pores with typical fields of $B \approx 1000 \text{ G}$. The background magnetic field in the quiet Sun and coronal holes have a net field of $B 0.1\text{--}0.5 \text{ G}$, while the absolute field strengths in

resolved elements amount to $B = 10\text{--}50 \text{ G}$. Therefore, understanding the magnetic field is extremely important to predict the solar activities and to develop relations among them.

2.2 Sunspots

Sunspots are the dark regions with the intense magnetic field and low temperature, found in the photosphere, are known to the humans since the middle of the fourth century, coined by Theophrastus. They are the temporary structures evolved on the Sun, and their population varies according to the eleven-year cycle of solar minimum and maximum. Their growth, survival, and decay have been explained by different theories and mechanisms.

Sunspots accompany secondary phenomena such as coronal loops, prominences, and reconnection events with the intense magnetic field, and usually appear in pairs of opposite magnetic polarity. Most solar flares and coronal mass ejections originate in magnetically active regions around visible sunspot groupings. Sunspots areas and sunspots numbers are the parameters of the sunspots that are useful and measurable quantities to study the sunspots that accompany secondary phenomena such as coronal loops, prominences, and reconnection events.

It is believed that the rotation of the sun causes distortion in the magnetic field. These distortions cause magnetic areas to break through the photosphere, resulting in the sunspots. Although Alfvén's theory of sunspot is not accepted yet, but preferred in many cases, and explains many properties of spots, such as their tendency to occur in pairs of opposite magnetic polarity, the duration of the solar cycle, the reversal of polarities in each new cycle, the progression of spots towards the equator during a cycle, etc.

Most solar flares and coronal mass ejections originate in magnetically active regions around visible sunspot groupings. The Sunspots numbers, which have been recorded for several centuries, used as a proxy for describing the level of solar activity. Sunspot Number, as an index, can be defined on a daily basis. But, because of the large day-to-day variation, they are usually averaged over longer periods, and the most common being the monthly and the yearly average. The sunspot number varies smoothly, charting the progress of the solar cycle when averaged over a year.

2.3 Solar Flares

Solar flares are the intense burst or explosion on the sun's atmosphere, caused due to sudden release of the free energy stored in twisting magnetic fields by

magnetic reconnection (Petschek 1964), and usually observed in close proximity to a sunspot group. They can last from minutes to hours and are also sites where particles (electrons, protons, and the heavier ones) are accelerated.

The study of solar flares is necessary as they're the most energetic explosions in the solar system, and they can have a direct effect on Earth's atmosphere. It can also be useful in understanding other cosmic events as the energy release process is similar.

A solar flare can be observed by the emergence of photons (or light) it releases at most every wavelength of the spectrum. The primary ways in which the flares are monitored are in x-rays and optical light. In the corona, where solar flares occur, the magnetic field structure is controlled by the photospheric magnetic field. Therefore, it is expected that the photospheric magnetic parameters have some strong relationships with the flare parameters. Flares occur in active regions around sunspots, where intense magnetic fields penetrate through the photosphere to link the corona to the solar interior. The same energy releases may produce coronal mass ejections (CMEs).

There are several studies, which has analysed the relations between the flare and the sunspot properties. A study for the probability of flare eruptions in terms of the sunspot parameters (increase and decrease

in the area, spot class, and others) was done by Giovanelli (1939). Also, Mayfield and Lawrence (1985), in their work, reported that the flare index derived from H α emission is proportional to the magnetic flux of active regions.

Solar flare index (SFI), an important parameter to predict the probability of solar flares to occur, and can be defined as the rough measurement of the total energy emitted by the flares. Kleczka (1952) introduced the quantity $FI = it$ to quantify the daily flare activity over 24 hours per day and named it ‘flare index’ (FI). In this relation, i represents the intensity scale of importance and t the duration of the flare in minutes.

Solar flare index can also be expressed as the energy of the flares per unit area. FI is one of the best indicators of activity variations in the chromosphere. It is of value as a measure of the short lived (minutes to hours) activity on the Sun. The comparison of FI with these similar indices should indicate how well they correlate, and this will be useful to model the temporal variations of solar activity.

2.4 Coronal Mass Ejections

One of the phenomena occurred due to the Solar Magnetic field, in which a significant amount of plasma releases from the sun’s corona. CMEs most frequently originate

from active regions on the Sun’s surface, such as groupings of sunspots, and are associated with solar flares.

A plausible important cause behind the generation of CMEs is magnetic reconnection. When two oppositely charged magnetic fields are brought together, rearrangement takes place, and immediately after this rearrangement, the energy stored in the oppositely directed magnetic field lines is released. This sudden release of energy is assumed responsible for solar flares which causes the CMEs.

CMEs are responsible for large-scale changes in the corona that have fundamental implications for the evolution of the magnetic flux of the Sun. Therefore, we can expect a good correlation between the various observed physical parameters of CMEs and the other tracers of solar activity such as sunspots number and sunspot areas. Due to the magnetic field, CMEs’ parameters like acceleration, mass, Kinetic energy, width, linear speed, and second-order initial and final speed are affected too.

The characterization of CMEs depends on three speeds: (1) the linear speed (2) initial quadratic speed, and (3) the final quadratic speed when the CMEs reach a height of 20 solar radii. The acceleration of a CME can be positive, negative, or close to zero, meaning CMEs speed up, move with constant speed or slow down.

2.5 Total Solar Irradiance (TSI)

The TSI variation is an important parameter for the understanding of the solar internal structure and solar-terrestrial relationships. It can indicate a secular change that might be associated with subtle changes in the solar radius, which may be related to a pulsating solar core. Short-term changes of TSI during the solar activity cycles are expected to be due to the luminosity changes connected with the temperature fluctuation of the solar surface, and may also be due to the redistribution of the solar radiation by sunspots and active region population.

Measurements of TSI vary over a range of periodicities, and most of the observed changes are probably associated with other solar activities, e.g., sunspot numbers, solar flares, solar diameter, solar neutrino fluxes, low order acoustic p-modes, etc. Estimations of solar magnetic field contribution to total solar irradiance variations show that magnetic features at the solar surface account for over 90% of the irradiance variations on a solar rotation time scale and at least 70% on a solar cycle time scale.

For the research project, the knowledge of the computation skills and predictive models were also essential. Therefore, the applications of Supervised Machine

Learning and Python programming were implemented, the theoretical concepts behind the Scatterplot Matrix, MATLAB, Curve Fit Models, Linear and Non-linear Regressions, Regression Forest Method, and Ensembled Modelling were also understood.

2.6 Machine Learning

Machine learning involves a computer to be trained using a given data set, and use this training to predict the properties of a given new data. For example, a computer can be trained by feeding it 1000 images of cats and 1000 more images other than that of a cat, and train so that the computer identifies the corresponding image correctly. When the computer observes a new image, it should be able to differentiate between cat's and other picture from the above training. The process of training and prediction involves the use of specialized algorithms. The training data is feed to an algorithm, and it uses the training data to give predictions on a new test data.

At most fundamental level, machine learning is categorized to three major kinds: supervised, unsupervised, and reinforcement learning. Supervised learning involves modelling the relationship between measured features of data and some label associated with the data. Once this model is determined, it can be used to apply labels to new and unknown data. This is further

subdivided into classification tasks and regression tasks: in classification, the labels are discrete categories, while in regression, the labels are continuous quantities.

Regression analysis consists of a set of machine learning methods that allow us to predict a continuous outcome variable (y) based on the value of one or multiple predictor variables (x). Briefly, the goal of regression model is to build a mathematical equation that defines y as a function of the x variables.

2.7 Curve fitting

Regression analysis is a form of predictive modelling technique, which investigates the relationship between a dependent and independent variable. In the regression, curve fitting is a mathematical tool that examines the relationship between one or more predictors (independent variables) and a response variable (dependent variable), intending to define the best fit model of the relationship. The trend in the data is captured and allows us to make predictions of how the data series will behave in the future.

Whenever the scattered data is fit to a straight line, then it is called linear regression, or the linear curve fit. A straight-line equation is obtained, having two constant parameters, called slope and intercept. But it is not necessary to get much

accuracy in the linear relationship for specific data sets, so it is better to look for the polynomial curve fits in those cases. Polynomial curve fitting is used to fit the data to the graph of a polynomial function.

For linear relationships, the mean of the dependent variable always changes by a specific amount for a unit increase in the independent variable. But, the change in the dependent variable associated with a one-unit shift in the independent variable varies based on location in observation space for a curved relationship.

Whenever the data is curve fitted, there are a few related values such as RMSE, SSE, R-square, and adjusted R-square associated with the curve that describes the errors, relationship between dependent and independent variables, and accuracy of the curve fit, which are helpful in statistical analysis of the graph. Thus, these quantities are the measure of the goodness of the fit. Apart from that, the equations can be obtained for a predictive model for the dependent variable.

RMSE or Root Mean Square Error is the standard deviation of the residuals (prediction errors). Residuals are a measure of distance of data points from the regression line; RMSE is a measure of spread of the residuals. In other words, it tells you degree of concentration of the data around the line of best fit. While SSE is the

sum of squares due to errors, measures the total deviation of the response values from the fit to the response values. It is also called the summed square of residuals and is usually labelled as SSE.

R-square, also known as the coefficient of determination is the proportion of the variance in the dependent variable that is predictable from the independent variable(s). It is a statistic used in the context of statistical models whose main purpose is either the prediction of future outcomes or the testing of hypothesis, on the basis of other related information. It is also a measurement of the closeness of the fit to the data points and the values ranges from 0 to 1. Therefore, it can be said that the R-square is the measurement of the accuracy of the fit. It is also known as the square of the correlation coefficient.

Correlation coefficient is defined as the statistical measure of the strength of the relationship between the relative movements of two variables. The values range between -1.0 and 1.0. There are several types of correlation coefficients, but the one that is most common is the Pearson correlation (r). This measures the strength and direction of the linear relationship between two variables. Another type is the Spearman's rank correlation coefficient, which is a measure of the relationship between two variables that can be described by a

monotonic function. The sign of the Spearman correlation indicates the direction of association between X (the independent variable) and Y (the dependent variable).

2.8 Scatterplot Matrix

A scatter plot matrix is a grid (or matrix) of scatter plots used to visualize bivariate relationships between combinations of variables. Each scatter plot in the matrix visualizes the relationship between a pair of variables, allowing many relationships to be explored in one chart. A scatter plot matrix is composed of a grid of mini-plots and one larger preview plot that shows selected mini-plot in more detail. A scatter plot matrix is made up of three or more Numeric fields. A scatter plot will be created for every pairwise combination of variables.

2.9 Ensembled Methods

It is a meta-algorithm which combines smaller or weaker models working on different subsets of main dataset to produce better predictions with less errors. The goal of ensemble methods is to combine the predictions of several base estimators built with a given learning algorithm in order to improve generalizability (robustness) over a single estimator. It can be categorized into its two major types: Parallel Ensemble Learning and Sequential Learning.

In the Parallel Learning, all base learners are running parallel. Bragging is one such method that puts data into 5 different bags and put random data points and then the model is trained and retrained. But in the Sequential Learning, base Learners are running on a sequential basis so that every next model is an improvement over the previous one. Boosting is one such model, which takes a subset, trains, finds errors, and emphasises on those errors in the next base learner along with random data points from main data set. There are mainly Adaptive Boosting, Gradient Boosting and XG boosting for the modelling.

Adaptive Boost has sequence of weak learners whose results are combined by weighted average. Gradient Boosting trains many models in a gradual, additive and sequential manner. The major difference between Adaptive Boost and Gradient Boosting Algorithm is how the two algorithms identify the shortcomings of weak learners (e.g. decision trees). While the Adaptive Boost model identifies the shortcomings by using high weight data points, gradient boosting performs the same by using gradients in the loss function.

We used LS Boost Optimizable Ensemble learning with 5-fold cross validation, i.e., we applied Ensemble method of type LS boost (Comes under Gradient Boosting), and running it 5 different times on data (each of

these base learners worked on different subsets of data) and produced the predictions.

3 Methodology & Data Collection

The work began with the background reading and collective study of the sun's interior, solar atmosphere, solar probes, and solar activities such as Coronal Mass Ejections, Solar Flares, Solar energetic particles, and High-speed solar wind streams, and the factors which influence solar activity. The core of all these activities was found to be the magnetic field followed by other factors such as sunspots number and area, tilt angle, speed parameters, number of flares, flare index, flux densities, etc. So, to align the objectives with the studies and data availability, the parameters were selected.

3.1 Objective I: To develop a predictive model for the energy of solar flares using machine learning

Understanding machine learning played an important role in the work. The team first studied upon various types and methods and upon discussion came to a standpoint of using reinforced learning. However, first the data was arranged and analysed. Since the

data exists between different timelines, the dataset was shortened and cut down to get equal amounts for comparison.

For training the predictive model, data for different solar flare parameters like Solar Flare Index (SFI), number of Solar Flares, Sunspot Area (SSA), Sunspot Number (SSN) were collected. However, the data was in a raw form i.e. un processable form. Thus, the data was later neatly arranged in Excel. Some datasets were in 'DAT' format which was then put in Excel sheets for easier data handling. If the datasets were on a daily basis, it was averaged month-wise by using the below mentioned code.

```
import pandas as pd

fulldata = pd.read_excel(r'C:\\
\\Users\\SPAS\\Documents\\Courses_Apri2020\\
SSERD\\Magnetic
\\flux_density_data.xlsx')

df1 = pd.DataFrame(fulldata, columns=
['dated']) df2 = pd.DataFrame(fulldata,
columns= ['MFD']) datedarr = df1.values
magfielddens = df2.values

cnt=1 sum1=0

file = open('mfd_avg.txt', 'a') for i in
range(1,len(datedarr)):

if(datedarr[i]==datedarr[i-1]):
if(magfielddens[i-1][0]!=100):
sum1+=magfielddens[i-1][0] cnt+=1

else:
```

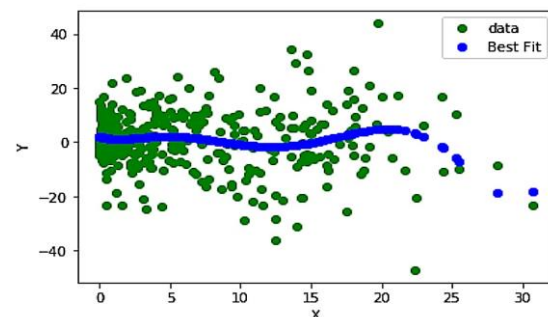
```
sum1+=magfielddens[i-1][0] avg=sum1/cnt
file.write(str(avg)) file.write('\\n')
sum1=0 cnt=1

final_list = [] for num in datedarr: if num
not in final_list: final_list.append(num)

# print(final_list) file =
open('mfd_avg_date.txt', 'a') for num in
final_list: arrOfStr = str(num).split(); res =
""; for a in arrOfStr: res += a[2:len(a) - 2] +
" ";

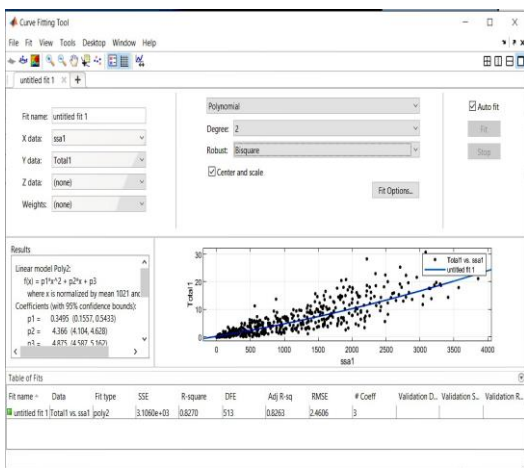
file.write(res) file.write('\\n') file.close()
print("end")
```

The data for SFI was taken and plotted against other parameters and curve fitted using python. Different curves were tried to curve-fit it to the maximum accuracy. One of the results and its corresponding code are shown in the pictures below. Unfortunately, the results were not satisfactory.

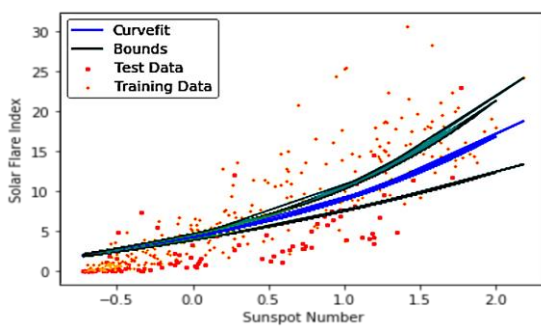


To make the curve fitting better and more accurate, team switched to MATLAB. Using Curve Fit toolbox on MATLAB, the data was curve fitted in much better way. The

versatility of MATLAB helped in getting better results. A sample of which is shown below.

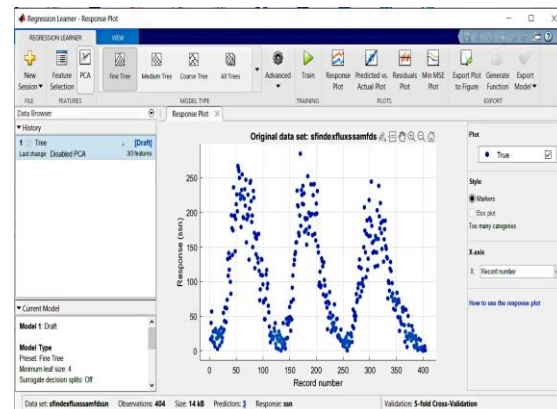


Each curve fit was used to understand the plots and the relation between the variables. Initially, the aim was to get a better Root Mean Square Error (RMSE) value but with time, focus was shifted to the R-square value instead. Training and testing of data was done in python, once again. However, the results were lacking expected accuracy and precision. The team relied upon MATLAB once again.



The data was hence arranged into a single excel sheet and imported into MATLAB. The MATLAB Regression Learner was used where the software receives the data and

applies various regression models to it. The regression learner contained all the required tools to build the model very precise and accurate. The picture of the feature is shown below.



Individually, the output of the models was satisfactory. However, insatiable to get more accuracy, the team applied ensemble method to the data. The model was enhanced and errors went down to a great extent. The code and its corresponding output were recorded and is displayed below.

3.I.I Generated code from Regression Learner App:

```
function [trainedModel, validationRMSE] =  
trainRegressionModel(trainingData)  
  
% [trainedModel, validationRMSE] =  
trainRegressionModel(trainingData)  
  
% returns a trained regression model and its  
RMSE. This code recreates the  
  
% model trained in Regression Learner app.  
Use the generated code to % automate  
training the same model with new data, or to
```

learn how to % programmatically train models.

%

% Input:

% trainingData: a table containing the same predictor and response % columns as imported into the app.

%

% Output:

% trainedModel: a struct containing the trained regression model. The

% struct contains various fields with information about the trained % model.

%

% trainedModel.predictFcn: a function to make predictions on new data.

% validationRMSE: a double containing the RMSE. In the app, the % History list displays the RMSE for each model.

%

% Use the code to train the model with new data. To retrain your model, % call the function from the command line with your original data or new % data as the input argument trainingData.

%

% For example, to retrain a regression model trained with the original data % set T, enter:

% [trainedModel, validationRMSE] =

trainRegressionModel(T)

%

% To make predictions with the returned 'trainedModel' on new data T2, use

% yfit = trainedModel.predictFcn(T2)

%

% T2 must be a table containing at least the same predictor columns as used % during training. For details, enter:

% trainedModel.HowToPredict

% Auto-generated by MATLAB on 28-Jul-2020 17:35:47

% Extract predictors and response

% This code processes the data into the right shape for training the % model.

```
inputTable = trainingData; predictorNames = 'mfd_avg', 'SSA', 'ssn'; predictors = inputTable(:, predictorNames); response = inputTable.SFIndex; isCategoricalPredictor = [false, false, false];
```

% Train a regression model

% This code specifies all the model options and trains the model.

template = templateTree(...

'MinLeafSize', 1, ...

```
'NumVariablesToSample', 3);
regressionEnsemble = fitrensemble...
predictors, ... response, ...

'Method', 'LSBoost', ...

'NumLearningCycles', 10, ...

'Learners', template, ...

'LearnRate', 0.2480844467477807);

% Create the result struct with predict
function predictorExtractionFcn = @(t) t(:, ...
predictorNames); ensemblePredictFcn =
@(x) predict(regressionEnsemble, x);
trainedModel.predictFcn = @(x)
ensemblePredictFcn(predictorExtractionFcn
(x));

% Add additional fields to the result struct
trainedModel.RequiredVariables = 'SSA',
'mfd_avg', 'ssn';
trainedModel.RegressionEnsemble =
regressionEnsemble; trainedModel.About =
'This struct is a trained model exported
from Regression Learner R2019b.';
trainedModel.HowToPredict = sprintf
("To make predictions on a new table, T,
use: \n yfit = c.predictFcn(T) \nreplacing
"c" with the name of the variable that is this
struct, e.g. "trainedModel". \n \nThe table,
T, must contain the variables returned by:
\n c.RequiredVariables \nVariable formats
(e.g. matrix/vector, datatype) must match
the original training data. \n

Additional variables are ignored. \n \nFor
more information, see <a
href="matlab:helpview
(fullfile(docroot, "stats", "stats.map"),
"appregression_exportmodeltoworkspace")"
> How to predict using an exported
model</a>);

% Extract predictors and response % This
code processes the data into the right shape
for training the % model.

inputTable = trainingData; predictorNames
= 'mfd_avg', 'SSA', 'ssn'; predictors =
inputTable(:, predictorNames); response =
inputTable.SFIndex; isCategoricalPredictor
= [false, false, false];

% Perform cross-validation

partitionedModel =
crossval(trainedModel.RegressionEnsemble,
'KFold', 5);

% Compute validation predictions
validationPredictions =
kfoldPredict(partitionedModel);

% Compute validation RMSE
validationRMSE =
sqrt(kfoldLoss(partitionedModel, 'LossFun',
'mse'));
```

30/7/20 7:06 PM MATLAB Command Window 14 of 14

```
>> [trainedModel, validationRMSE] = trainRegressionModel(trainingData)
trainedModel =
struct with fields:
    predictFcn: @(x)ensemblePredictFcn(predictorExtractionFcn(x))
    RequiredVariables: {'SSA' 'mfd_avg' 'sm'}
    RegressionEnsemble: [1x1 classreg.learning.regr.RegessionEnsemble]
    About: 'This struct is a trained model exported from Regression'
Learner E2019b.
    HowToPredict: 'To make predictions on a new table, T, use: yfit = c.mfd_avg.predictFcn(T) where replacing 'e' with the name of the variable that is this struct, e.g., 'trainedModel'. The table, T, must contain the variables returned by: c.mfd_avg.RequiredVariables. Variable formats (e.g. matrix/vector, datatype) must match the original training data. Additional variables are ignored. For more information, see How to predict using an exported model.'
validationRMSE =
3.1326
>> yfit = trainedModel.predictFcn(T2)
yfit =
0.7419
```

10 Best 2.357 0.25126 2.357 2.3924 10 0.27012 8
11 Accept 2.4201 0.24155 2.357 2.4199 10 0.26632 1
12 Accept 3.6867 10.334 2.357 2.4197 450 0.0010008 72
13 Accept 2.5278 13.068 2.357 2.4171 500 0.027803 211
14 Best 2.3473 9.4441 2.3473 2.3524 499 0.046688 1
15 Accept 3.6761 0.26784 2.3473 2.3527 11 0.043683 2
16 Accept 2.5469 13.285 2.3473 2.3653 500 0.092423 384
17 Accept 2.5713 9.5351 2.3473 2.4259 499 0.048562 4
18 Accept 4.4025 0.23602 2.3473 2.4268 10 0.0010049 3
19 Accept 2.5428 10.15 2.3473 2.4255 497 0.0040187 8
20 Best 2.3061 9.6017 2.3061 2.3305 499 0.0090502 3
=====
Iter Eval Objective: Objective BestSoFar BestSoFar NumLearningC- LearnRate MaxNumSplits
result log1(loss) runtime {observed} {estim.} cycles
=====
21 Accept 2.459 12.068 2.3061 2.3636 499 0.0093261 155
22 Accept 2.3464 10.092 2.3061 2.3479 498 0.0096835 1
23 Accept 2.3481 9.8439 2.3061 2.3447 500 0.010916 1
24 Accept 2.3879 9.5912 2.3061 2.3554 498 0.0086048 1
25 Accept 2.3263 9.2733 2.3061 2.3465 496 0.012019 1
26 Best 2.2731 9.1628 2.2731 2.3295 494 0.011746 1
27 Accept 2.3571 9.6821 2.2731 2.3319 500 0.014501 1
28 Accept 2.4199 9.0396 2.2731 2.3388 497 0.0081132 1
29 Accept 2.3651 9.1128 2.2731 2.3412 498 0.013798 1
30 Accept 2.6574 1.778 2.2731 2.3422 94 0.019379 1

Optimization completed.
MaxObjectiveEvaluations of 30 reached.
Total function evaluations: 30
Total elapsed time: 214.99 seconds.
Total objective function evaluation time: 179.4644
Best observed feasible point:

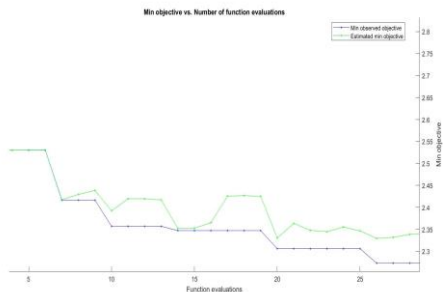
3.1.2 Code for same model without using Regression Learner App:

```
load('sfnewopt.mat')
X = [mfd_avg SSA sm];
Y = SFIndex;
rng default
Mdl = fitrensemble(X,Y, ...
    'Method','LSBoost',...
    'Learner',templateTree('Surrogate','on'),...
    'OptimizeHyperparameters',{'NumLearningCycles','MaxNumSplits','LearnRate'},...
    'HyperparameterOptimizationOptions',struct('Repartition',true,... ...
    'AcquisitionFunctionName','expected-improvement-plus'))
loss = kfoldLoss(crossval(Mdl,'kfold',5))
Mdl2 = fitrensemble(X,Y, ...
    'Method','LSBoost',...
    'Learner',templateTree('Surrogate','on'));
loss2 = kfoldLoss(crossval(Mdl2,'kfold',5))
Mdl3 = fitrensemble(X,Y);
loss3 = kfoldLoss(crossval(Mdl3,'kfold',10))

Output:
    >> code_without_app
=====
| Iter | Eval | Objective: | Objective | BestSoFar | BestSoFar | NumLearningC- | LearnRate | MaxNumSplits |
| | result | log1(loss) | runtime | {observed} | {estim.} | cycles | | |
=====
| 1 | Best | 2.8621 | 8.6406 | 2.8621 | 2.8621 | 383 | 0.51519 | 6 |
| 2 | Best | 2.7014 | 0.46159 | 2.7014 | 2.7099 | 16 | 0.66503 | 13 |
| 3 | Best | 2.5302 | 0.92495 | 2.5302 | 2.5313 | 33 | 0.2556 | 350 |
| 4 | Accept | 4.2993 | 0.34115 | 2.5302 | 2.5304 | 13 | 0.0053227 | 8 |
| 5 | Accept | 2.8378 | 1.8638 | 2.5302 | 2.5305 | 68 | 0.99821 | 385 |
| 6 | Accept | 2.6973 | 0.31369 | 2.5302 | 2.5307 | 10 | 0.13171 | 295 |
| 7 | Best | 2.4165 | 0.29034 | 2.4165 | 2.4176 | 10 | 0.28637 | 364 |
| 8 | Accept | 2.4795 | 0.28574 | 2.4165 | 2.4296 | 10 | 0.35491 | 371 |
| 9 | Accept | 2.4493 | 0.28383 | 2.4165 | 2.4387 | 10 | 0.25623 | 136 |
```

NumLearningCycles	LearnRate	MaxNumSplits
494	0.011746	1
Observed objective function value = 2.2731		
Estimated objective function value = 2.3422		
Function evaluation time = 9.1628		
Best estimated feasible point (according to models):		
NumLearningCycles	LearnRate	MaxNumSplits
500	0.010916	1
Estimated objective function value = 2.3422		
Estimated function evaluation time = 9.4136		
Mdl =		
classreg.learning.regr.RegessionEnsemble		
ResponseName: 'Y'		
CategoricalPredictors: []		
ResponseTransform: 'none'		
NumObservations: 387		
HyperparameterOptimizationResults: [1x1 BayesianOptimization]		
NumTrained: 500		
Method: 'LSBoost'		
LearnerNames: {'Tree'}		
ReasonForTermination: 'Terminated normally after completing the requested number of training cycles.'		
FitInfo: [500x1 double]		
FitInfoDescription: (2x1 cell)		
Regularization: []		
Properties, Methods		
loss = 9.2569		
loss2 = 16.7055		
loss3 = 15.5417		

3.I.3 Output for hyperparameter optimization:



The recorded results were analysed and compared with the standard values to ensure proper model building.

3.2 Objective II: To find an inverse correlation between the sunspot area and solar activity

Concerning to the correlation aspect of our objective, three different CMEs' speed parameters, Total Solar Irradiance (TSI), and CMEs width and solar flares parameters like Solar Flare Index (SFI), Number of flares (monthly) were taken into consideration. At first, the data for the chosen parameters was collected from various credible sources. However, the data was in raw form i.e. not in processable form (.dat or .txt format). Hence, the data was to be converted to excel for further processing. Some of the data was as daily data which was to be averaged to monthly for further use. This was done using a python code.

3.2.I Averaging code

```

import pandas as pd

fulldata = pd.read_excel
(r'C:\Users\SPAS\Documents\Courses_A
pril2020\SSERD\CMEavg.xlsx') df1 =
pd.DataFrame(fulldata, columns= ['Date2'])
df2 = pd.DataFrame(fulldata, columns=
['Acceleration'])

datedarr = df1.values
central = df2.values
cnt=1
sum1=0

file = open('cme_avg.txt', 'a')

for i in range(1,len(datedarr)):
if(datedarr[i]==datedarr[i-1]):

if(central[i-1][0]!=100):
sum1+=central[i-1][0]
cnt+=1
else:
sum1+=central[i-1][0]

avg=sum1/cnt
file.write(str(avg))

file.write('\n')

sum1=0
cnt=1

file.close()

print("end")

```

The objective entails development of a correlation between the mentioned parameters and SSA without the effects of SSN and Magnetic Flux changes as explained before. Hence, it became important for the team to do a 2-stage refining on the existing data to get the data corresponding to same/similar SSN and Magnetic Flux. A python code was used to categorize all the epochs (time periods) which had SSN values in the ranges of 1-5, 6-10 and 11-15.

3.2.2 Code to sort the data to SSN ranges

```
import pandas as pd
import datetime
fulldata = pd.read_excel(r'C:\Users\SPAS\Documents\Courses_April2020\SSERD\daily1.xlsx')
df1 = pd.DataFrame(fulldata, columns=['dated'])
df2 = pd.DataFrame(fulldata, columns=['sunspotno'])
datedarr = df1.values
sunspotno = df2.values
print(datedarr[1])
print(sunspotno[1])
final_list = []
for num in sunspotno:
    if num not in final_list:
        final_list.append(num)
final_list.sort()
cnt=0
max1=0
sum1=0
for key in final_list:
    if(key>max1):
        max1=key
    sum1+=key
    cnt+=1
print('Average= ')
print(sum1/cnt)
print(str(datedarr[1]))
string = str(datedarr[1])
arrOfStr = string.split();
res = "";
for a in arrOfStr :
    res += a[2:len(a) - 2] + " ";
print(res)
string2 = '09/02/2017'
print(string2)
```

```
format_str = '%d/%m/%Y' # The format
datetime_obj =
datetime.datetime.strptime(res, format_str)
print(datetime_obj.date())
```

In the 2nd stage of processing i.e. for attaining data with same amount of magnetic flux, team encountered a hurdle. The data for magnetic flux was not available. Hence, the data for magnetic flux

density and SSA were multiplied for the corresponding epochs and the magnetic flux data was attained. Upon observation, the magnetic flux values were not same for any of the epochs. Thus, it

became inevitable for the team, but to categorize the epochs in the ranges of Magnetic Flux difference. A program was coded to achieve the same.

3.2.3 Magnetic flux code

```
import pandas as pd
fulldata = pd.read_excel
(r'C:\Users\SPAS\Documents\Courses_A
pril2020\SSERD\Magnetic_flux
_density_data.xlsx')
df1 = pd.DataFrame(fulldata, columns=
['dated'])
df2 = pd.DataFrame(fulldata, columns=
['MFD'])
```

```
datedarr = df1.values
magfielddens = df2.values
cnt=1
sum1=0
file = open('mfd_avg.txt', 'a')
for i in range(1,len(datedarr)):
if(datedarr[i]==datedarr[i-1]):
if(magfielddens[i-1][0]!=100):
sum1+=magfielddens[i-1][0]
cnt+=1
else:
sum1+=magfielddens[i-1][0]
avg=sum1/cnt
file.write(str(avg))
file.write('\n')
sum1=0
cnt=1
final_list = []
for num in datedarr:
if num not in final_list:
final_list.append(num)
# print(final_list)
file = open('mfd_avg_date.txt', 'a')
for num in final_list:
arrOfStr = str(num).split();
```

```

res = "";
for a in arrOfStr:
    res += a[2:len(a) - 2] + " ";
file.write(res)
file.write('\n')
file.close()
print("end")

```

The range of Magnetic flux difference (MF difference) was considered and not Magnetic flux due to

the fact that the MF difference is the affecting factor in the hypothesis. Multiple ranges were chosen

to understand the trend of parametric changes with MF difference as well. The next task for the team

was to get the data for the corresponding refined epochs. Programming was used here as well.

3.2.4 Data extraction code

```

import numpy as np
import scipy.optimize
import pandas as p
import matplotlib.pyplot as plt
import xlwt
from xlwt import Workbook

```

```

epochdata = p.read_excel
(r'D:\PRATEEK\SSERD\Data\Ready to
process\EPOCH_TSI(m).xlsx')
epochs = p.DataFrame(epochdata,
columns= ['Epochs'])
MY = p.DataFrame(epochdata, columns=
['MY'])
area = p.DataFrame(epochdata, columns=
['Area'])
par = p.DataFrame(epochdata,
columns=['TSI'])
Epochs = epochs.values
my = MY.values
Area = area.values
Par = par.values
i=0
j=0
k=0
l=0
wb=Workbook()
sheet1=wb.add_sheet("Sheet 1")
for i in range(0,len(EPOCHS)) :
    if Epochs[i]=="100/100":
        k+=2
    l=0
else:

```

```

for j in range(0,len(my)):
    if (Epochs[i]==my[j]):
        sheet1.write(l+1,k,str(Area[i][0]))
        sheet1.write(l+1,k+1,str(Par[j][0]))
        l+=1
    wb.save('Epoch_TSI_6-10.xls')
print("end")

```

At the end of this stage, the data for all the parameters and its corresponding SSA values was available and ready to be plotted. The data was read in the program and was plotted. Further, it was

curve-fitted with an inverse equation (i.e. $y = m/x + b$). For all the graphs, the correlation coefficient was also found. Unfortunately, the results were completely off the hypothesis.

Upon introspection, the team found the mistake. There was a human error in the 2nd stage of the refining. Instead of using the refined data from the first stage, the original data was used and hence the results were flawed. The results further improved after a talk with Mr. Pavan Kumar who suggested

us to explore the possibilities of different equations for curve-fitting. The equation of curve fit was

changed to a general equation

$$(i.e. y = \left(\frac{m}{x^a} + \frac{n}{x^b} + c \right)^d)$$

3.2.5 Plotting and curve-fitting code

```

import math
import numpy as np
import scipy.optimize
from scipy.optimize import curve_fit
import pandas as p
import matplotlib.pyplot as plt
from scipy.stats import pearsonr
from scipy.stats import spearmanr
from scipy.stats import kendalltau
x, y = np.loadtxt("Book1.csv",
                   delimiter=",", skiprows=1, unpack = True,
                   usecols=[0,1])
i=0
j=i+1
for i in range (0,len(x)-1):
    for j in range (i+1,len(x)-1):
        if x[i]>x[j]:
            temp=x[i]
            x[i]=x[j]
            x[j]=temp
            temp2=y[i]
            y[i]=y[j]
            y[j]=temp2

```

```

y[j]=temp2

j+=1

def test(x, a, b, c, d, m, n, o, q, e ,f):
    return (m/x**a + n/x**b + c)**d

param,param_cov= curve_fit(test,x,y,
maxfev=1000000000)

residuals = y- test(x, *param)
ss_res = np.sum(residuals**2)
ss_tot = np.sum((y-np.mean(y))**2)

r_squared = 1 - (ss_res / ss_tot)
print(r_squared)

spm, _ = spearmanr(x,y)

kt, _ = kendalltau(x,y)

data=len(x)

plt.plot(x,y,'o', label=data)

plt.plot(x,test(x,*param), label=spm)

plt.xlabel('SSA')

plt.ylabel('SFI')

plt.title('SFI vs. SSA (SSN 1-10, 0-900 MF difference)')

plt.legend()

plt.show()

```

4 Results & Discussion

4.I Objective I: To develop a predictive model for energy of solar flares using Machine Learning

4.I.I Prediction model for Solar Flare:

Firstly, we took 384 datasets in total. The predictors we took are average Magnetic Flux Density,

Sunspot Number and Sunspot Area. The response of Solar Flare Index was recorded.

4.I.2 LS boost optimizable ensemble regression model

Cross-validation: 5 folds validation

The results obtained were:

RMSE : 2.9653

R-squared : 0.79

MSE : 8.7929

MAE : 2.0799

Prediction speed = 14000 obs/sec

Training Time : 193.59 sec

4.I.3 Model type:

Present: Optimizable Ensemble

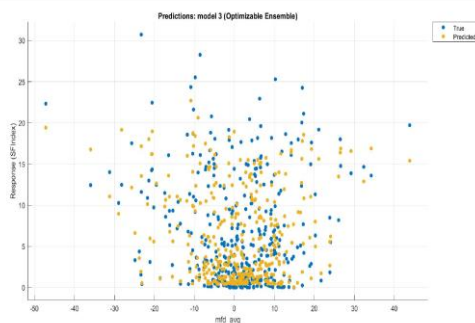
4.I.4 Optimized Hyperparameters

Ensemble method : LS Boost

Minimum leaf size : 1

Number of learners : 10

Number of predictors to sample : 3



4.I.5 Hyperparameter Search Range

Ensemble method : Bag, LS Boost

Number of learners : 10-500

Learning rate : 0.001-1

Minimum leaf size : 1-192

Number of predictors to sample : 1-3

4.I.6 Optimizer Options

Optimizer Bayesian optimization

Acquisition function : Expected improvement per second plus

Training time limit : false

Iterations : 30

4.I.7 Feature Selection

All features used in the model, before PCA.

PCA: PCA disabled

4.I.8 SFI vs Magnetic Flux Density

Figure 4.1: Prediction model between SF Index and Average MFD

This is a prediction model between SF Index and Average MFD. It shows us the true and predicted data points.

4.I.9 SFI v/s Record Number:

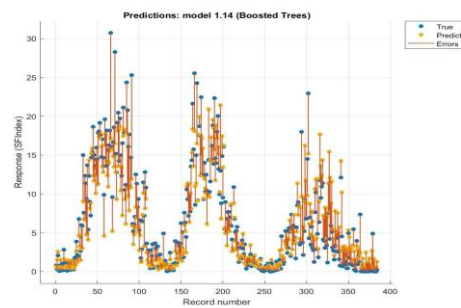


Figure 4.2: Prediction model between SF Index and Record Number.

This is a prediction between SF Index and Record Number. The RED lines show the errors, the BLUE dots show true data points and the YELLOW dots show the predicted points. Record Number allocates the number to the recorded variables of dataset.

4.I.10 SFI v/s SSA:

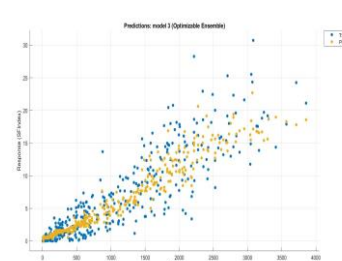


Figure 4.3: Prediction model between SF Index and SSA.

This is a prediction model between SF Index and SSA. We can see the True and Predicted data points represented by the BLUE and YELLOW dots, respectively.

4.I.II SF Index v/s SSN:

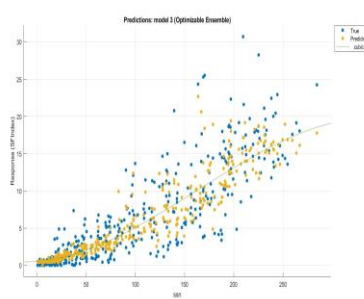


Figure 4.4: Prediction model between SF Index and SSN.

It is the prediction model between SF Index and Sunspot Number(SSN). The GREY line represents the cubic relationship and the BLUE and YELLOW dots represent the True and Predicted data points, respectively.

4.I.I2 Minimum MSE Optimization:

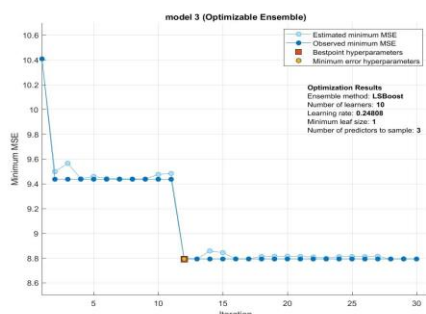


Figure 4.5: Minimum MSE optimization for every iteration of processing or training the dataset(model)

This curve is generated to optimize the minimum MSE for every iteration of processing or training the dataset(model) and find the minimum optimal parameter for MSE(8.79). The error was reduced by optimization. This plot is between minimum MSE and Iteration. This model shows Estimated minimum MSE, Observed minimum MSE, Best point hyperparameters and minimum error hyperparameters.

4.I.I3 Optimized Ensemble Model between the Predicted response and True response:

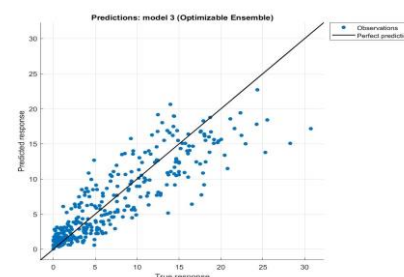


Figure 4.6: Optimized Ensemble Model between the Predicted response and True response

The above is also an optimized ensemble model between the Predicted response and True response. It shows us the observations and the perfect prediction line, represented by the BLUE dots and BLACK line, respectively.

4.I.I4 Residual Plots: Evaluate Model Using Residuals Plot

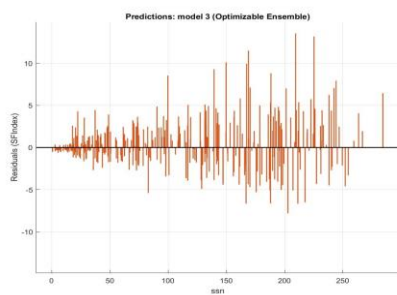


Figure 4.7: Optimized Ensemble Prediction Model between SF Index and SSN

The residuals plot displays the difference between the predicted and true responses. Usually a good model has residuals scattered roughly symmetrically around 0.

The above curve is an optimized ensemble prediction model between SF Index and SSN. We can observe that as the graph progresses, it gets wider and towards the end, it becomes narrow again. It is clear that at the ends of the graph, the error is less than that present in the middle portion.

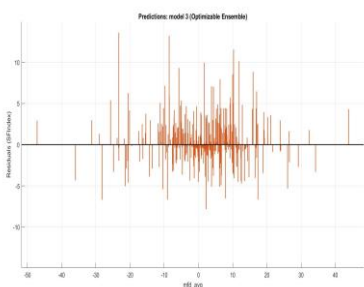


Figure 4.8: Optimized Ensemble Prediction Model between SF Index and Average MFD

This curve is an optimized ensemble prediction model between SF Index and Average MFD. We can observe that as the graph progresses, it gets wider and towards the end, it becomes small again. The error is more in the middle portion than at the ends.

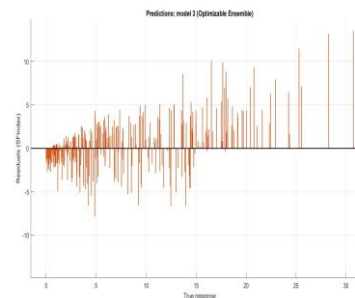


Figure 4.9: Optimized Ensemble Prediction Model between SF Index and True Response

This curve is an optimized ensemble prediction model between SF Index and True Response. As the graph progresses, it gets wider. The error is lesser in the ends as compared to the error in the middle portion.

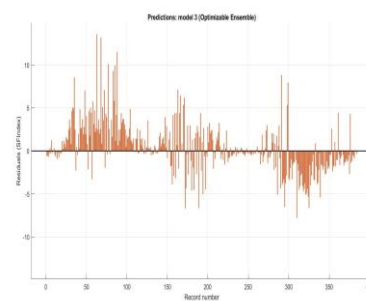


Figure 4.10: Optimized Ensemble Prediction Model between SF Index and Record Number

This curve is an optimized ensemble prediction model between SF Index and Record Number. This is different as it has more error differences at the ends than at the middle. This causes more error at the ends than the middle.

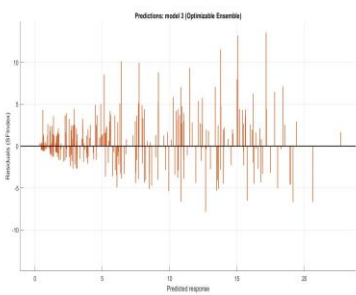


Figure 4.11: Optimized Ensemble Prediction Model between SF Index and Predicted Response

This curve is an optimized ensemble prediction model between SF Index and Predicted Response. We can observe that as the graph progresses, it gets wider and towards the end, it becomes small again. Error differences are more in the beginning.

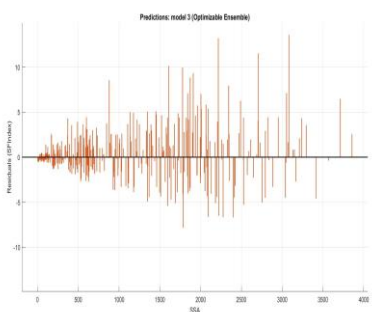


Figure 4.12: Optimized Ensemble Prediction Model between SF Index and SSA

This curve is an optimized ensemble prediction model between SF Index and SSA. We can observe that as the graph progresses, it gets wider. Error differences present in the beginning and the end are less compared to the middle regions.

4.I.15 Discussions:

1. R-square value of 0.6 or above was the goal of the model and attaining 0.79 as the R-square value shows that the model fits with the data to a fair extent keeping in mind the noise and variation in data.
2. RMSE value in this instance is scale relative. Considering the variance of data and also limitations in data availability, the RMSE value is acceptable and in time, with collection of data, the values can be improved using the same model.
3. Keeping in mind the variations in the data trends, the average magnitude of errors is acceptable. Hence, MAE is in the acceptable range.
4. A comparatively higher value of MSE indicates the highly biased or high variance estimate. This suggests a more refined approach or it is also explained by insufficiency of the data.
5. Since the data was shortened due to excessive refining and combining with the other parameters, the MSE value may be considered to be in the acceptable range.

Using ensemble model was to make sure the errors are reduced to the minimum and to optimize the model to the maximum.

6. The cross validation had been done in 5 folds and not more to avoid over fitting of the model. Since the data set was split into 5 models, each of it was used for the training and testing to get the acceptable results. It has also provided much more information on the algorithm performance.

4.2 Objective II: To find the correlation between sunspot area and related parameters

Our objective was to obtain the value of Spearman's coefficient by plotting and curve fitting graphs

for various parameters related to CMEs and solar flares with all the possible SSN ranges and magnetic flux differences (MF differences). Since the data for lesser MF difference is not available due

to 2-stage refining, the trends are to be observed. If the coefficient values increase as the MF difference range increases, we can extrapolate it back to the lesser MF difference ranges and suggest

the corresponding coefficients to be negative. A negative coefficient would mean an inverse relation

supporting our hypothesis.

Graphs were plotted for SSN ranges 1-5 and 6-10 with magnetic flux differences varying from 0-600, 0-700, 0-800. The following were observed:

4.2.I Number of Solar Flares v/s SSA:

4.2.I.I SSN I-5:

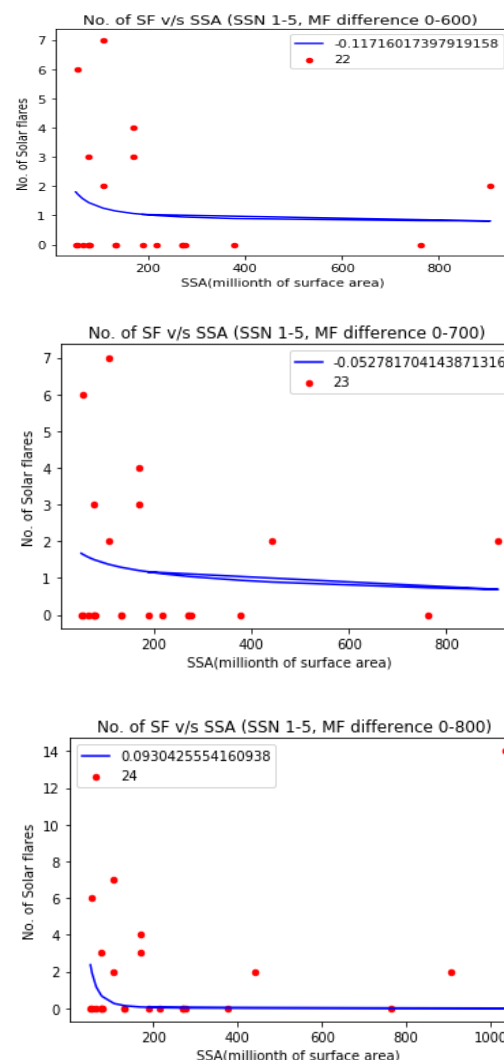


Figure 4.13: No. Of SF v/s SSA for SSN range 1-5

It is quite evident from the graphs that MF difference affects no. of flares more

drastically as compared to ranges of SSN, as Spearman's coefficient value surged from -0.117 to 0.093 over the given range.

4.2.1.2 SSN 6-10:

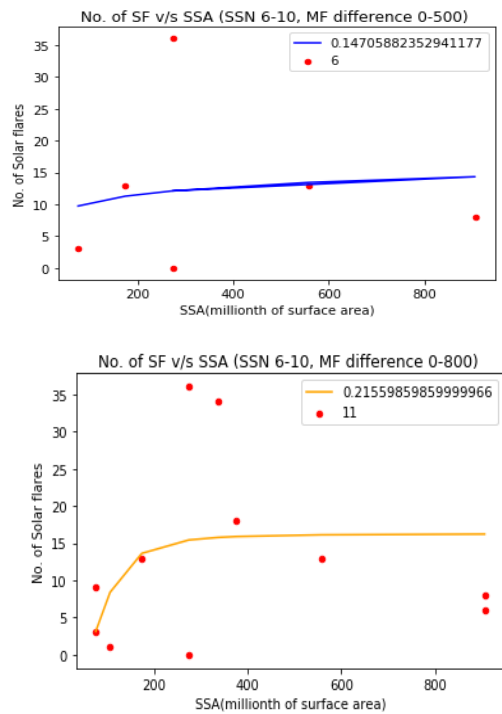


Figure 4.14: No. Of SF v/s SSA for SSN range 6-10

Similarly, the correlation coefficient consistently increases from 0.147 to 0.215 as MF difference increase from 0-500 to 0-800 respectively.

4.2.2 Solar Flare Index v/s SSA:

4.2.2.1 SSN I-5:

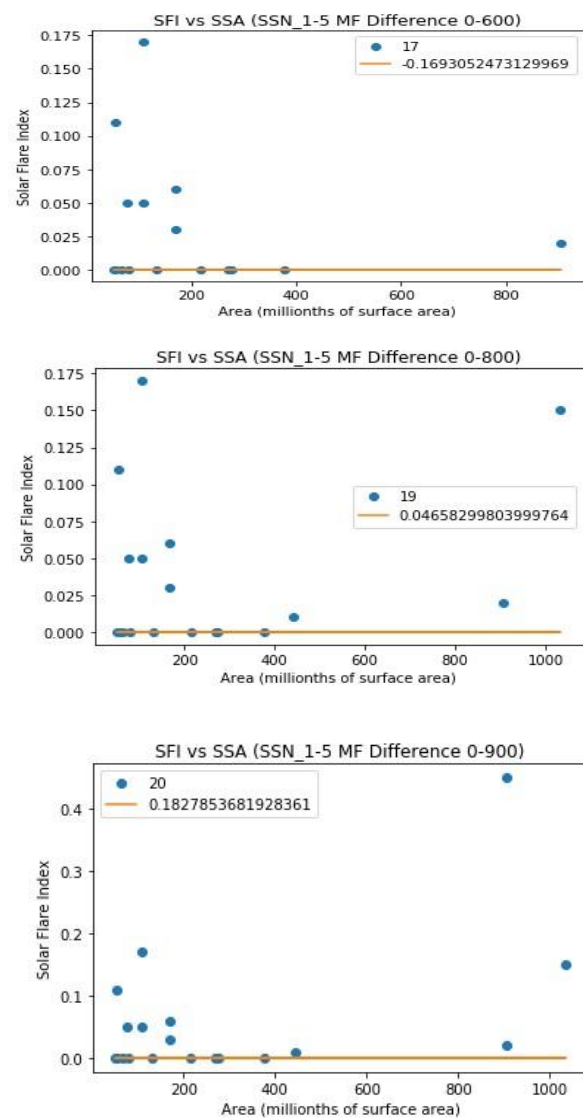


Figure 4.15: SFI v/s SSA for SSN range I-5

Keeping SSN range constant, the coefficient value gradually increases from -0.169 to 0.182 with increase in MF difference.

4.2.2.2 SSN 6-10:

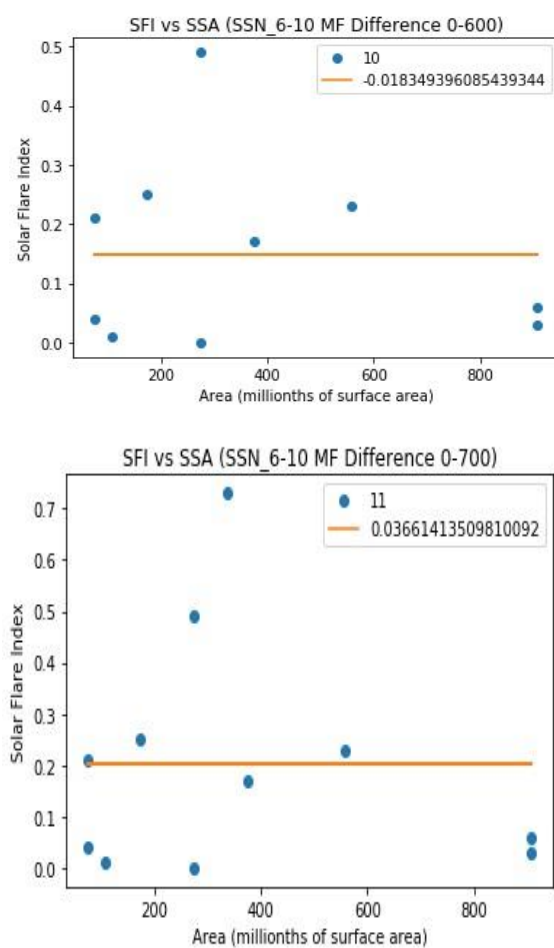


Figure 4.16: SFI v/s SSA for SSN range 6-10

The graphs are quite identical with that of SSN range 1-5 by showing a steady increase in coefficient value. The Spearman's coefficient for the MF difference 0-700 increased to 0.0366141 and this value is retained for the higher values of MFD due to lack of data.

4.2.3 Total Solar Irradiance v/s SSA:

4.2.3.I SSN I-5:

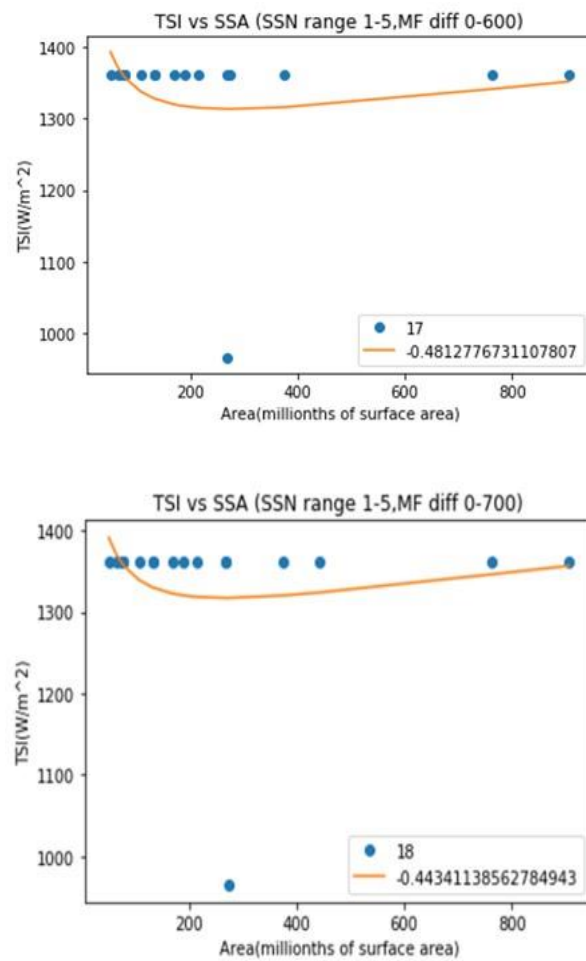


Figure 4.17: TSI v/s SSA for SSN range 1-5

The given graphs show the increase in coefficient value from -0.481277 for 0-600 to -0.443411 for 0-700 as MF difference increase.

4.2.3.2 SSN 6-10:

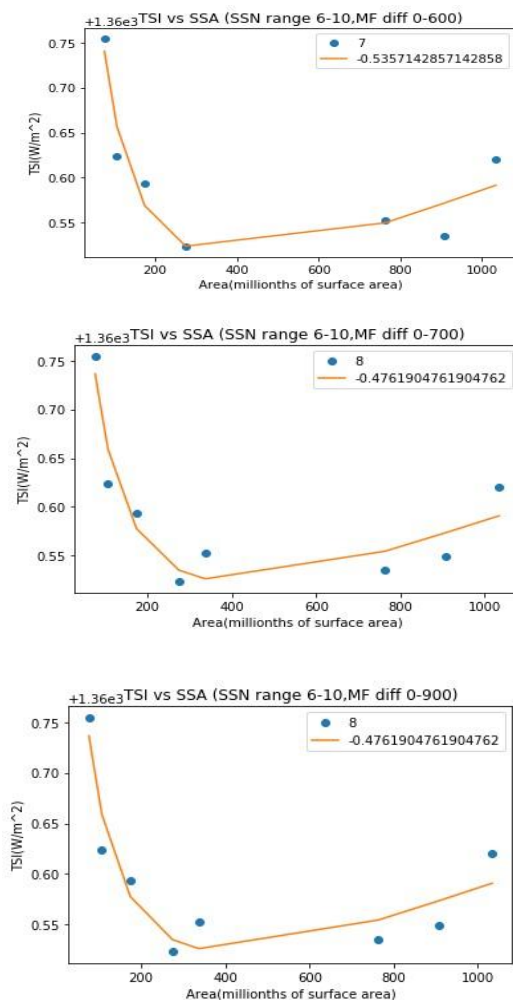


Figure 4.18: TSI v/s SSA for SSN range 6-10

It is clear from the graphs that the Spearman's coefficient increases from -0.535 to -0.476 for the MF differences 0-600 and 0-700. This value remains constant till 0-900 owing to lack of data.

4.2.4 CME Width v/s SSA:

4.2.4.1 SSN I-5:

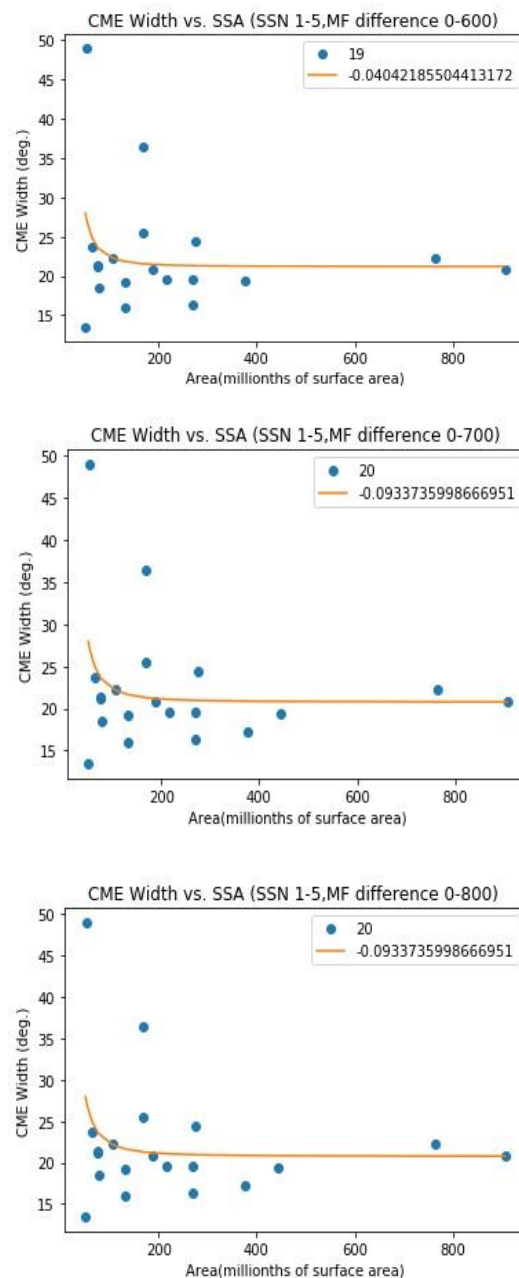


Figure 4.19: CME width v/s SSA for SSN range 1-5

As far as CME Width is concerned, the correlation coefficient decreases from -0.0404 for 0-600 MF difference to -0.0933 for 0-700 MF difference and stays the same

for other ranges. This is an anomaly. However, it can be dismissed due to the fact that the coefficient is still negative, clearly indicating an inverse relation between the parameter.

4.2.4.2 SSN 6-10:

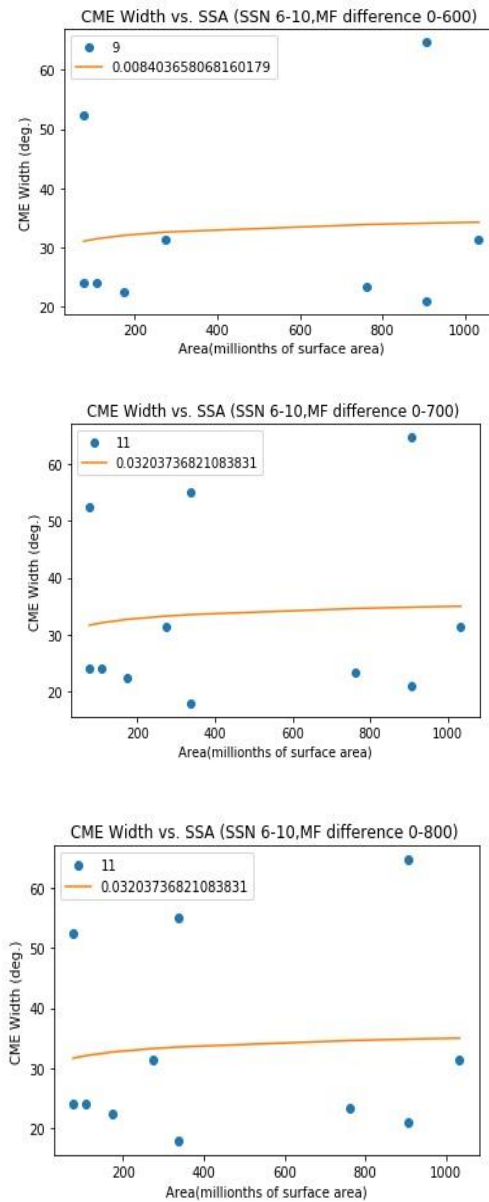


Figure 4.20: CME width v/s SSA for SSN range 6-10

For SSN range 6-10, the coefficient increases from 0.0084 for 0-600 MF difference range to 0.032 for 0-700 MF difference.

4.2.5 Linear speed v/s SSA:

4.2.5.I SSN 1-5:

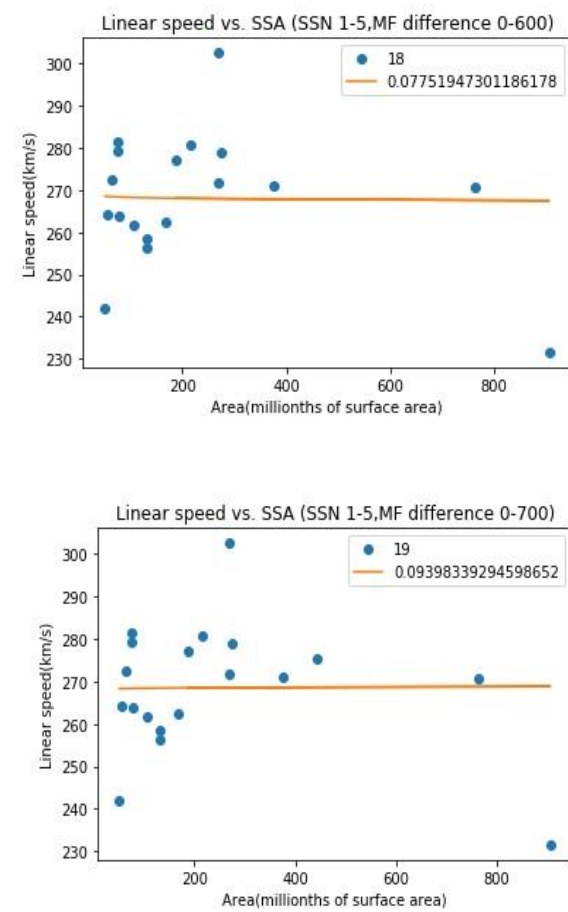


Figure 4.21: Linear speed v/s SSA for SSN range 1-5

For CME's linear speeds, as observed from the graphs, the spearman coefficient increases from 0.0775 for MF difference 0-600 to 0.0939 for MF difference 0-700. The coefficient and the curve remain same for the

next MF difference ranges due to the lack of data.

4.2.5.2 SSN 6-10:

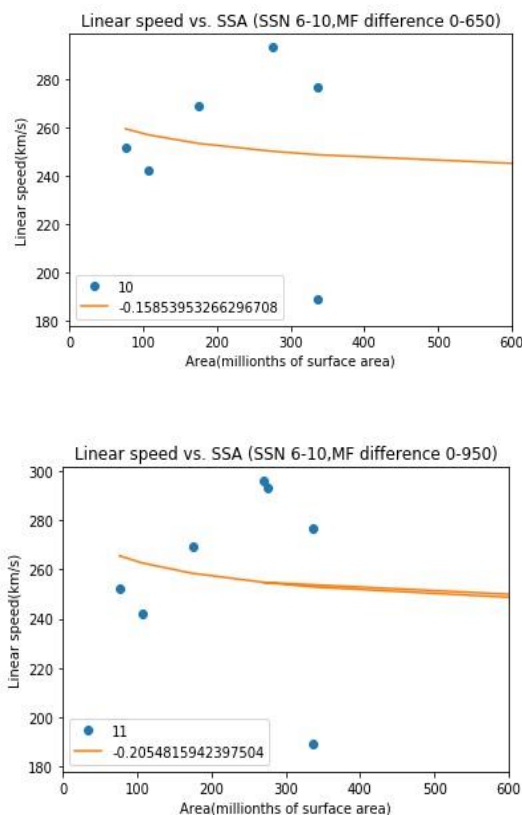


Figure 4.22: Linear speed v/s SSA for SSN range 6-10

Similarly, for the SSN range 6-10, we can see the spearman coefficient decreases from -0.15 for 0-650 MF difference to -0.20 for 0-950 MF difference. This is exhibiting an anomalous behaviour.

Reasons for this behaviour could be lack of data. The data sets were same for other ranges in between 0-650 and 0-950 MF difference leaving us no room to perform analysis on those.

4.2.6 2nd order Initial Speed v/s SSA:

4.2.6.I SSN 1-5:

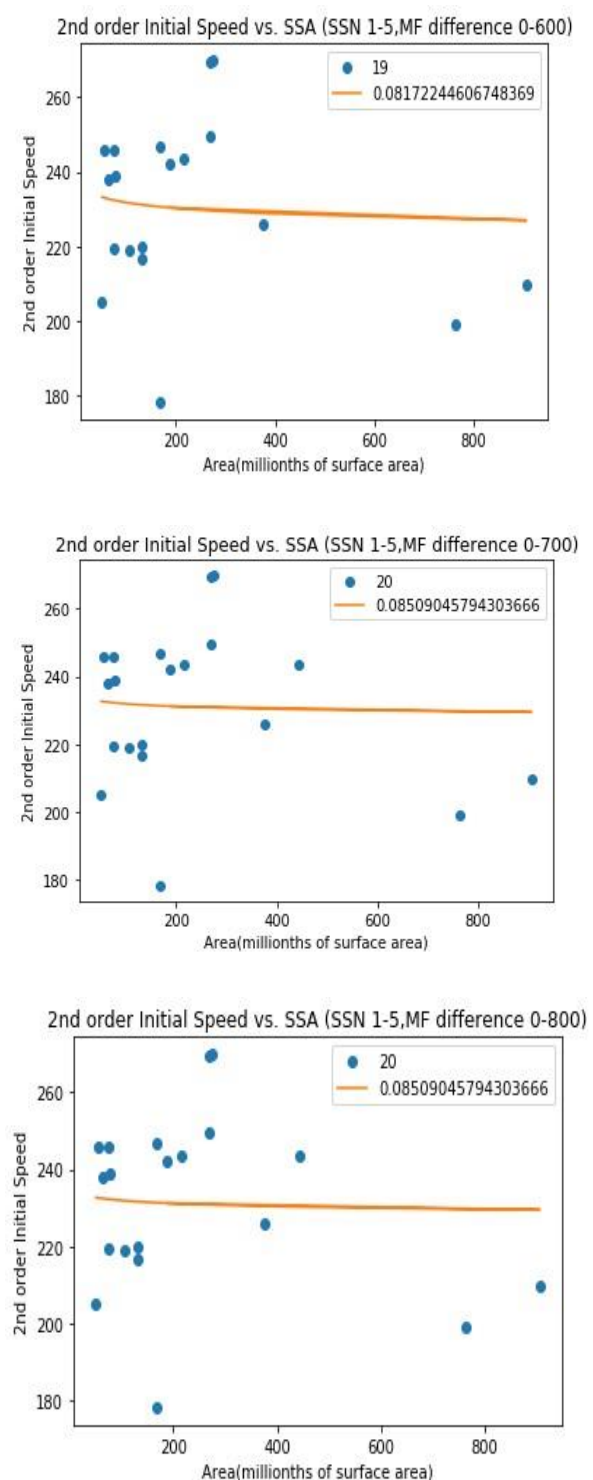


Figure 4.23: 2nd order Initial Speed v/s SSA for SSN range 1-5

From the graph, we can see that there is a small increase in the correlation coefficient from

0.0817224 to 0.0850904. The coefficient remains 0.0850 for the next ranges due to lack of data.

4.2.6.2 SSN 6-10:

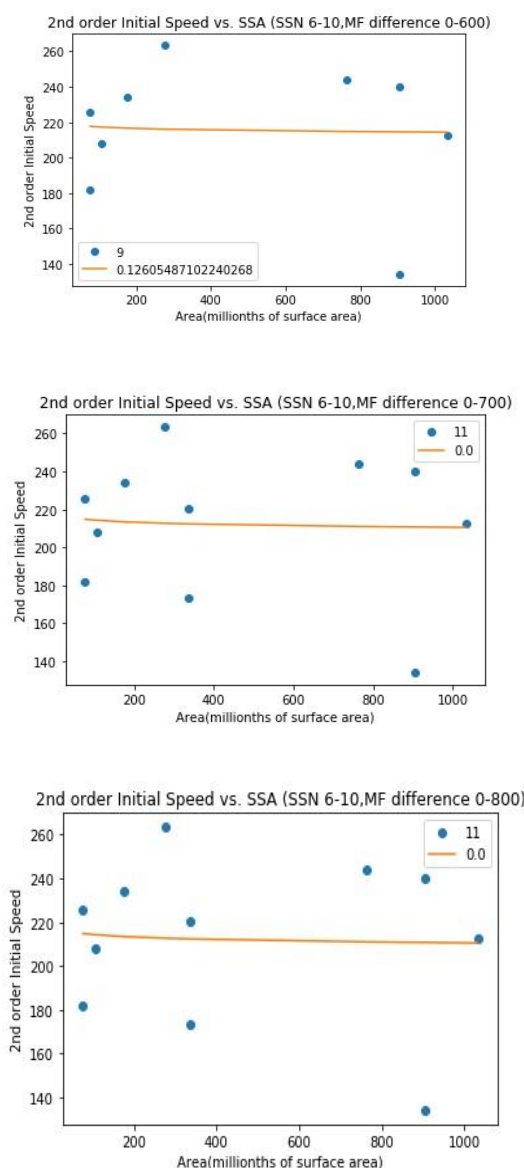


Figure 4.24: 2nd order Initial Speed v/s SSA for SSN range 6-10

Here, we can observe that the correlation coefficient decreases from 0.12605 to 0.0. This is an anomaly which can be due to the lack of data for this SSN range. The magnetic flux might be another factor causing the anomaly.

4.2.7 2nd order Final Speed v/s SSA:

4.2.7.1 SSN 1-5:

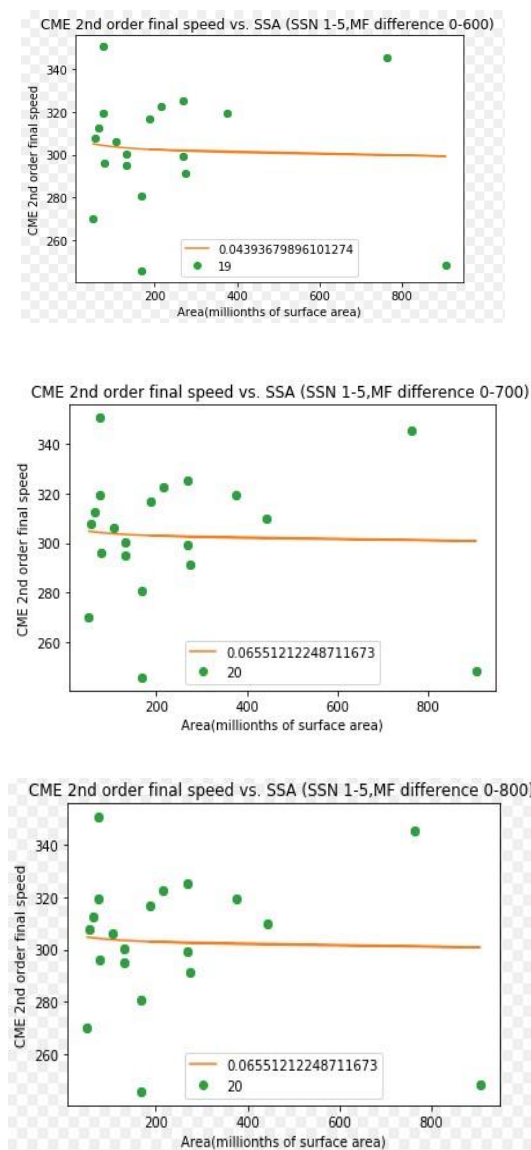


Figure 4.25: 2nd order Final Speed v/s SSA for SSN range 1-5

It can be observed that there is an increase in the value of the coefficient from 0.0439 for 0-600 to

0.0655 for 0-700. The value remains the same for the further ranges due to the lack of data.

4.2.7.2 SSN 6-10:

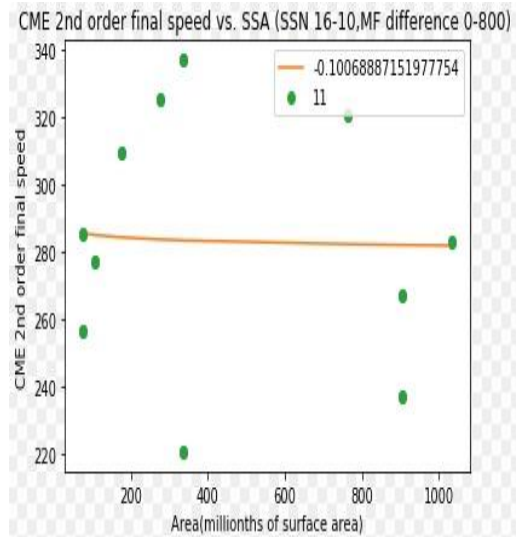
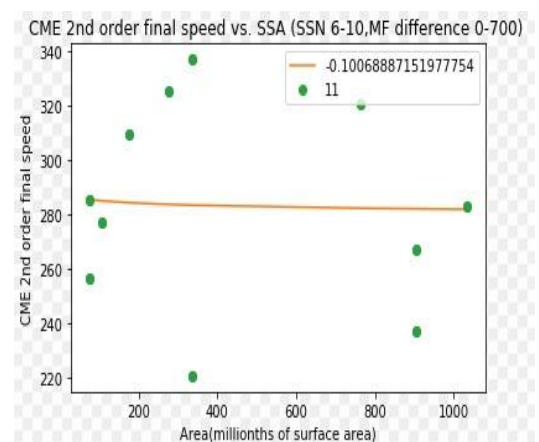
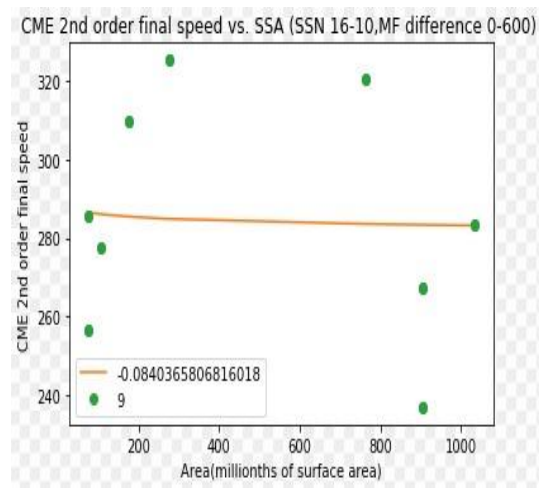


Figure 4.26: 2nd order Final Speed v/s SSA for SSN range 6-10

The graphs clearly suggest that the coefficient decreases here, from -0.0840365 for 0-600 to -0.1006 for 0-700, after which it remains constant. This decrease is again, an anomaly which might be occurring due to the lack of data.

5 Conclusions

5.1 Objective I: To develop a predictive model for the energy of Solar Flares using Machine Learning

- As we obtained R-square value of 0.79, which is well above the required conditions, we can say that the model fits with the data, while considering the noise and variation in data.
- The RMSE value obtained (2.9653) is scale relative and acceptable. With more

data collection and time, these values can be well improved

3. The average magnitude of errors is acceptable, while considering the variations in data trends. Thus, MAE value (2.0799) is in the acceptable range.
4. A high variance estimate is indicated by a comparatively higher value of MSE (8.7929). This might be explained by the insufficiency of the data or requires a more refined approach.
5. It can be concluded by saying that if more parameters and data sets were available, predictions for SFI could have been more precise
6. This model initially didn't give desirable results, but it was after this that we found out about ensemble learning. We used ensemble learning as the data was very scattered and bad in a few places. Ensemble predictions have helped this model immensely.

5.2 Objective II : To find the correlation between Sunspot Area and related parameters

1. The coefficient values are not negative for all the parameters. The reason is the effect of magnetic flux. In an ideal case, same value of magnetic flux would not affect the results yielding a perfect negative correlation coefficient.

2. It can be concluded that all the graphs which have the coefficient values increasing along with the MF difference can be extrapolated to lower MF difference values and corresponding coefficients can be suggested to be negative. The lower coefficient values would mean a negative coefficient which suggest that the relation between the parameters and SSA is an inverse relation.
3. Some anomalies were also observed. The reason for that might be lack of data and same dataset for multiple ranges. The difference in data sets for different ranges could have helped in understanding the behaviour more efficiently.
4. Out of 7 parameters, 2 ranges of SSN for each parameter i.e. 14 trends, only 4 trends were anomalous. This gives a rough accuracy of 71.428%.

5.3 Future Scope

5.3.1 Objective I:To develop a predictive model for the energy of Solar Flares using Machine Learning

Prediction of Solar Flares is a very important factor in understanding the space weather. The sudden eruptions of the flares and surges in number of energetic particles make the satellites and the astronauts vulnerable. The proposed and rendered model to predict the Solar Flare Index (SFI),

which is a measure of energy emitted by the flare can be used to foresee the impact of the flare. Hence, giving us time to brace for impact and take necessary precautions. The model can be incorporated with a website and make it open for external use. From a research perspective, other parameters can be added to the model and increase the accuracy. One of the important parameters can be magnetic field strengths which can be achieved by studying the magnetograms. Further, the method of building such model can be used and applied to other parameters like duration of flares, time of occurrence etc.

5.3.2 Objective II: To find the correlation between Sunspot Area and related parameters

The accomplished results can be used as basis for further research. An equation between the parameters and SSA can be formed which can be used to make the results more concrete. This equation would not only relate the parameter with SSA but also the parameter with each other. With the existing parameters, new parameters like geomagnetic field strengths can be added in order to understand the impact of sun on Earth. Another potential candidate as a parameter can be the magnetic field strength of sun. Magnetograms can be studied and the variation with SSA can help us solidify the correlation.

6 References

6.1 Background & Literature survey

1. How the Sun's magnetic field works:

<https://docs.sunpy.org/en/stable/>

2. Understanding the magnetic Sun:

<https://www.nasa.gov/feature/goddard/2016/understanding-the-magnetic-sun2016>.

3. Differential rotation:

<https://astronomy.swin.edu.au/cosmos/D/Differential+Rotation>

4. Solar Magnetic Field:

<https://www.sciencedirect.com/topics/earth-and-planetary-sciences/solar-magnetic-field>

5. Babu Ram Tiwari 'The Solar Flux and Sunspot Number; A long trend analysis'

<https://journals.aijr.in/index.php/ias/article/download/751/172/2018>.

6. Sunspots:

<https://en.wikipedia.org/wiki/Sunspot#:~:text=Sunspots%20are%20temporary%20phenomena%20on,field%20flux%20that%20inhibit%20convection>

7. What is the Sunspot Number:

<https://www.sws.bom.gov.au/Educational/2/3/3>

8. Coronal Mass Ejections:

[https://en.wikipedia.org/wiki/Coronal_mass_ejection#:~:text=A%20coronal%20mass%20ejection%20\(CME,be%20observed%20in%20coronagraph%20imagery](https://en.wikipedia.org/wiki/Coronal_mass_ejection#:~:text=A%20coronal%20mass%20ejection%20(CME,be%20observed%20in%20coronagraph%20imagery)

9. Onuchukwu Chika Christian ‘A statistical analysis of sunspot and CME parameters for the Solar cycle 23.’

<http://medcraveonline.com/PAIJ/PAIJ-02-00103.pdf> 2018.

10. K. B. Ramesh ‘Coronal Mass Ejections and Sunspots-Solar Cycle Perspective’

<https://iopscience.iop.org/article/10.1088/2041-8205/712/1/L77/pdf> 2010.

11. SOHO LASCO CME CATALOG:

https://cdaw.gsfc.nasa.gov/CME_list/catalog_description.htm

12. What is a solar flare:

<https://www.nasa.gov/content/goddard/what-is-a-solar-flare>

13. Correlations between flare parameters magnetic parameters in Solar Flares:

<https://academic.oup.com/pasj/article/61/1/75/1501202>

14. Probhas Raychaudhuri ‘Total Solar Irradiance Variability and the Solar Activity Cycle’

<https://arxiv.org/ftp/astro-ph/papers/0601/0601335.pdf>

15. SK Solanki ‘How much of the Solar irradiance variations is caused by the Magnetic Field at the Solar surface?’

<https://www.sciencedirect.com/science/article/pii/S0273117702002387> 2002.

16. Machine learning with Python:

https://www.tutorialspoint.com/machine_learning_with_python/machine_learning_with_python_ecosystem.htm

17. Introduction to Machine Learning using Python:

<https://www.geeksforgeeks.org/introduction-machine-learning-using-python/#:~:text=To%20Prevent%20It-,Introduction%20To%20Machine%20Learning%20using%20Python,when%20exposed%20to%20new%20data.>

18. What is Machine Learning:

<https://jakevdp.github.io/PythonDataScienceHandbook/05.01-what-is-machine-learning.html>

19. Scatter Plot Matrix:

<https://pro.arcgis.com/en/pro-app/help/analysis/geoprocessing/charts/scatterplotmatrix.htm#:~:text=A%20scatter%20plot%20matrix%20is,be%20explored%20in%20one%20chart.>

<https://www.itl.nist.gov/div898/handbook/eda/section3/scatterb.htm>

20. Curve and Surface Fitting:

<https://www.originlab.com/index.aspx?go=Products/Origin/DataAnalysis/CurveFitting>

21. What is Root Mean Square Error?

[https://www.statisticshowto.com/probability-and-statistics/regression-analysis/rmse-rootmeansquareerror/#:~:text=Root%20Mean%20Square%20Error%20\(RMSE\)%20is%20the%20standard%20deviation%20of,theline%20of%20best%20fit.](https://www.statisticshowto.com/probability-and-statistics/regression-analysis/rmse-rootmeansquareerror/#:~:text=Root%20Mean%20Square%20Error%20(RMSE)%20is%20the%20standard%20deviation%20of,theline%20of%20best%20fit.)

22. Goodness of Fit statistics:

<https://web.maths.unsw.edu.au/~adelle/Garvan/Assays/GoodnessOfFit.html#:~:text=SSE%20is%20the%20sum%20of,accounted%20for%20by%20the%20model.>

23. Coefficient of Determination:

https://en.wikipedia.org/wiki/Coefficient_of_determination

24. Correlation Coefficient:

<https://www.investopedia.com/terms/c/correlationcoefficient.asp>

25. Spearman's rank correlation coefficient:

https://en.wikipedia.org/wiki/Spearman%27s_rank_correlation_coefficient

26. Ensemble methods:

<https://scikit-learn.org/stable/modules/ensemble.html>

27. Understanding Gradient Boosting Machines:

<https://towardsdatascience.com/understanding-gradient-boosting-machines-9be756fe76a>

Conceptual Design of Self-Sustainable Inflatable Martian Habitat



Team ECLSS-IH & SSERD IPD

August 2020



Conceptual Design of Self-Sustainable Inflatable Martian Habitat

External Guide - Mr. Mahesh P.

Internal Guide - Mr. Rohith



Our Team

1. Pranay Tummalapalli, 05011502817, Bharati Vidyapeeth's College of Engineering, New Delhi.
2. Vignesh Vishwanath, CB.EN. U4AEE18048, Amrita Vishwa Vidyapeetham, Coimbatore, Tamil Nadu.
3. Aishanee Pattnaik, BE1038016, Birla Institute of Technology, Mesra.
4. Aviraj Hanmant Pawar, 180101051045, Sandip University Nashik, Maharashtra.
5. D V S Siddhartha, Andhra Pradesh.
6. Jinit Dhondiyal, IU1741090007, Indus University, Ahmedabad.
7. Kripasree S, TCR17EC027, Government Engineering College, Thrissur Alappuzha, Kerala.
8. Kanchan Vinayak Bhale, C22018111145, Cummins College of Engineering for Women, Pune, Maharashtra.
9. Mohammed Meeran Adnan, Acharya Institute of Technology, Channapatna, Karnataka.

ACKNOWLEDGEMENT

We express our sincere gratitude to Society for Space Education Research and Development (SSERD), Mr. Sujay Sreedhar, Ms. Nikhitha C. for their help and support. We are also grateful to Mr. Mahesh P. and Mr. Rohith NR, our External and Internal Guides respectively, who have bestowed their great efforts and guidance at appropriate levels without which it would have been very difficult on our part to finish this work. Finally, we would also like to thank the other team members for providing us with valuable feedback and suggestions from time to time.

ABSTRACT

A trip to Mars is a costly undertaking. But it is as exciting and as it is rewarding in the field of space exploration. With space agencies working towards colonizing Mars, it is clear that there is a need for long-term human sustenance due to the fact that frequent resupply missions to Mars are next to impossible. This is definitely not a reliable option. So this project deals with a Technology Demonstration Mission for a self-sustainable Martian habitat. It deals with Inflatable Habitat Technology and Life Support Systems required for the mission. The concept of an “Inflatable Habitat” is becoming an active and demanding area of research, as far as human space missions are considered. So this project is a conceptual design of such a mission, and is designed in par with SpaceX’s Mars Mission. This also deals with all the necessary factors including detailed study of materials required, structural design and analysis and design of the Environment Control and Life Support System or ECLSS required. The ECLSS is what provides an Earth-like environment inside the habitat, making it suitable for the humans to live. The main aim of this mission is to achieve self-sustainability. Therefore, it would also serve a test-bed to test the possibility of growing plants inside the habitat to provide food for the astronauts. This project also caters to the power requirements and In-Situ Resource Management. This way, it is possible to achieve self-sustenance. With this, there is a strong hope that this project will open doors for future manned missions to Mars, eventually making Mars an established colony.

Contents

Our Team	94
ACKNOWLEDGEMENT.....	95
ABSTRACT	96
LIST OF FIGURES	101
LIST OF TABLES	102
1.Introduction	103
2. Objective.....	103
3.Habitat Location	103
4.Design of the habitat.....	104
4.1 Design Requirements	104
4.1.1 Mechanical Properties	104
4.1.2 Aerodynamic and Structural Stability	105
4.1.3 Simulated Environment	105
4.1.4 Volume.....	105
4.2 Structural Design and Analysis	105
4.3 Internal Atmosphere of the Habitat.....	106
4.4 Dimensions and Volumetric Analysis	107

4.4.1 Dimensions	107
4.4.2 Volume calculations from values	108
4.4.3 Stress Calculations	108
5. Materials	109
6. Stowed Configuration for Vehicle Payload.....	111
7. Deployment	111
8. Power Source	112
8.1 Solar Energy	112
8.2 Nickel Hydrogen Batteries	112
8.3 Fuel Cells	113
9. In-Situ Resource Utilization	113
9.1 Fuel production from a Martian atmosphere.....	114
9.1.1 Adsorptive Compressor	114
9.1.2 Solid Oxide Electrolyzer	114
9.1.3 Adsorptive Separation	115
9.1.4 FT synthesis slurry bed	115
10. Life Support System.....	115
10.1 Waste Management System (WMS)	116
10.1.1 Human metabolic waste-collection and storage.	116

10.1.2 Food waste- collection and storage	116
10.1.3 Non-recyclable waste management system.	117
10.1.4 Medical waste collection and storage	117
10.1.5 Miscellaneous waste.....	117
10.2 Water Reclamation System	117
10.2.1 Reusable Waste Processing Assembly (RWPA).....	117
10.2.2 Urine Processor Assembly (UPA)	118
10.2.3 Distillation Assembly (DA)	119
10.2.4 Pre-treatment of liquid waste in WSTA.....	120
10.3 Atmospheric Management System (AMS)	121
10.3.1 Atmosphere circulation.....	121
10.3.2 Atmosphere Particulate Control	121
10.3.3 Trace Contaminant Control	121
10.3.4 Fire detection and notification	122
10.3.5 Post-fire Atmosphere Recovery.....	122
10.3.6 O ₂ Generation System	123
10.3.7 Atmospheric Humidity and Temperature Control.....	123
10.3.8 Carbon Dioxide Removal System.....	124
10.3.9 Four – Bed Molecular Sieve (4BMS) Carbon Dioxide Removal Assembly (CDRA)	124
10.3.10 Sabatier CRA	125

11. Results and Conclusions.....	126
12. References	126

LIST OF FIGURES

- A topographic view of Valles Marineras
- 3D representation of the inflated habitat
- Diagram representing functional organization
- Top view of the habitat
- Hoops stress for semi cylindrical structure
- Longitudinal stress for half-cylinder
- Membrane stress for hemisphere
- Cross-section of the habitat showing the different layers of shielding
- 3D representation of the stowed configuration
- Deployment stages
- Stowed configuration
- Half deployment with module bases extended
- Fully deployed habitat
- Ethane Fuel from CO₂ block diagram
- Hierarchy chart of WMS
- Output waste quantities of a person per day
- Block diagram of waste management system
- Block diagram representation of UPA
- Cross-section of Distillation Assembly

- Block diagram representation of the AMS
- Block diagram representation of CDRA
- Block diagram of the Sabatier and OGS showing the quantities of material

LIST OF TABLES

- Water quality data, indicating Russian pre-treatment may improve water quality.

I. Introduction

Space exploration has shown significant growth over the years. In the era of space exploration, a manned mission to Mars has far reaching implications both technologically, and for the growth of our country. Unlike missions to the ISS or the moon, a mission to mars is definitely a more challenging one especially since there is very little known about the planet.

All these days, we have continuously witnessed various unmanned missions to Mars to gather data of the environmental conditions on the planet, its topography, the composition of its surface and most importantly the possibility of the presence of water on the planet. Such unmanned missions include rovers like Curiosity, Spirit and Opportunity and the recently launched Perseverance Rover and Ingenuity Helicopter, and orbiters like Mars Orbiter Mission launched by ISRO, Maven Orbiter, Mars Reconnaissance Orbiter, Mars Odyssey Orbiter among many more. These missions have gathered valuable data for us while also paving the way for future missions.

If humans are to colonies Mars one day, an important step would be to solve the existing challenges. The technologies that would be developed on Earth need to be

tested in actual Martian conditions, after testing them on Earth by simulating those conditions. For this, Technology Demonstration Missions would need to be carried out and habitats with self-sustainable technology should be designed. Another important aspect of the mission would be to test the feasibility of growing selected crops in the habitat to meet the dietary requirements of the crew and public, once colonization is successful. The inflatable habitat that we have designed takes into account all these requirements.

2. Objective

Developing the Conceptual Design of an Inflatable Martian Habitat as part of a Technology Demonstration Mission for a crew of four astronauts (for four months), taking into account its Structural Analysis and Material Requirements. The design also includes the development of self-sustainable In-Situ Resource Utilisation Systems, and the required Environment Control and Life Support Systems or ECLSS and Power Systems.

3. Habitat Location

Apart from the Voluminous volcanism revealed on early in Valles Marineris, Landslides, origin and evolution of the

layered deposits, evidence for precipitation on Mars from dendritic valleys in the Valles Marineris area, mobility of large rock avalanches and some debates about the hydrated mineral stratigraphy of Ius Chasma. Mars's Valles Marineris, is host to numerous preserved geologic features, modern atmospheric phenomena and potential subsurface aqueous activity favorable towards human habitation. Our Inflatable habitat proposal zone is centered atop the region due to its rich science and technology aspects and promising favorable environment conditions including high solar insolation and atmospheric pressure. As a future aspect, the key science interests in this region have always been search for biological signs and correlation with earth atmosphere for their survival. Valles Marineris stretches over 4,000 km across Mars in the east-west region below the equator and 7km deep, one of the largest canyons of the Solar System.

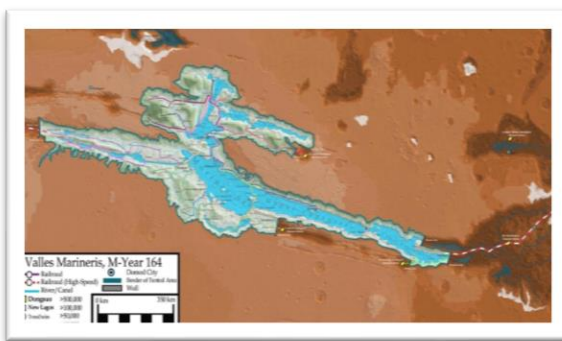


Figure 1: A topographic view of Valles Marineris

4.Design of the habitat

An Inflatable in general, is a structure that expands on being pressurized (typically like a balloon). This offers several advantages over a rigid-frame structure. The major advantage is that it offers high packing efficiency, thereby possessing less weight compared to a metal structure.

So it can be deflated and packed in a small space in the rocket and carried, and later be inflated with air. This is also highly reliable due to payload constraints and also due to increasing research in the area of composite materials. NASA (along with Bigelow Aerospace) is already working on this technology, keeping in mind the requirements of the upcoming Moon and Mars missions. This would serve as the habitat for the Martian astronauts.

4.I Design Requirements

4.I.I Mechanical Properties

Unlike on Earth, the habitat would be directly exposed to the harsh Martian environment and therefore must possess very good mechanical properties. To give an insight to the atmospheric conditions, the major factor to be considered is the temperature. The average surface temperature on Mars is -63degC, and it

reaches a maximum of 20degC. So there is a vast temperature gradient. The next parameter to be considered is the dusty Martian storms, which reach speeds up to 30m/s. This poses a risk to the overall stability of the structure. In addition to these, Mars is highly prone to radiation and micrometeoroids. Therefore, all these have to be kept in mind while designing the habitat. To encounter these problems, the materials used should possess high impact tolerance, tensile strength, puncture resistance, creep life, temperature resistance, radiation-resistance and flex-resistance. This would require high space-grade materials that satisfy all these requirements, in addition to being light weight and cost-effective. Therefore, a detailed study on suitable materials is essential, which is provided subsequently.

4.I.2 Aerodynamic and Structural Stability

The structure as a whole should be able to withstand Martian storms. This demands it to be stable even during the worst dust storms. So the stability of the structure should be considered. This could be facilitated by avoiding tall vertical structures and instead going with horizontal and symmetrical structures.

4.I.3 Simulated Environment

The habitat should be able to house the astronauts in an Earth-like environment by providing the necessary pressure and temperature conditions and all other necessary ECLSS to ensure sustenance. The internal pressure would exert very high stresses on the inner walls of the structure due to the fact that the Martian atmosphere is extremely thin (about 1% dense as that of Earth). So the habitat should be designed in such a way that it withstands the stresses as well as supports human sustenance.

4.I.4 Volume

The structure should also be volumetrically efficient, thereby ensuring that sufficient usable volume is available for the astronauts to carry out all their activities. This also includes precise dimensions of the habitat, structural analysis, shielding requirements, mode of deployment and basic conceptual designs.

4.2 Structural Design and Analysis

Keeping in mind all the aforementioned requirements, in order for the habitat to be habitable for the crew, and for it to provide enough space for all activities, a semi-hemispherical dome and four semi-cylindrical detachable modules have been

conceptualised and designed. The dome is situated centrally and surrounded by the modules through isolatable airlock entries. Figure 1 shows a three-dimensional representation of the inflatable martian habitat after being deployed. It shows a central semi-rigid hemispherical wall with an inflatable half dome on top. The base of the central dome is made out of thermally insulated materials to ensure that the habitat has a safe and livable atmosphere at all times. The four modules are attached to the central dome through airlock entrances. In case of damage to any module, it can first be isolated from the rest of the habitat by sealing the airlock entrances, then deflated in order for the crew to carry out a repair operation. The cylindrical walls of the modules are inflatable and made of layered materials and their base is made out of a semi-rigid thermally insulated material to insulate the living space inside from the adverse temperatures of the martian surface. The airlocks are also made of rigid materials.



Figure 2: 3D representation of the inflated habitat

Figure 2. shows the functional organisation of the conceptual design of the Martian habitat. The central dome will serve as the Control Centre for the entire habitat. The modules attached to it will serve different purposes. The main entry bay will have an airlock system and will also act as the storage for spacesuits and other equipment. This structure is aerodynamically and structurally stable, making it reliable and convenient for the astronauts to use. This novel design will be very stable during the Martian storms too. All the modules are interconnected, ensuring efficient functioning of the entire habitat and easy monitoring from the control center.

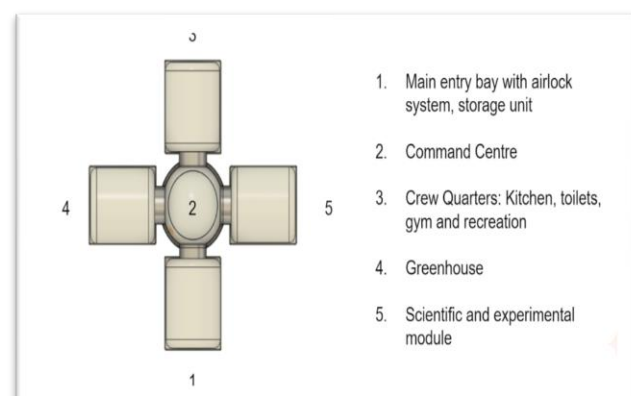


Figure 3: Diagram representing functional organisation

4.3 Internal Atmosphere of the Habitat

As the name suggests, internal pressure and temperature requirements have to be taken into account. This highly determines the

overall functioning of the habitat. The standard sea-level atmospheric pressure on Earth is 101kPa. We can assume the same pressure to be maintained inside the habitat, but it poses a lot of challenges. The Martian atmosphere is very thin. The atmospheric pressure is around 0.6kPa (less than 1% of Earth's). This would induce very high tensile stress on the walls of the structure as there is no resistance offered by the external Martian atmosphere. Thus, the structure has to be designed in such a way that it is able to withstand the stresses due to internal pressure, as well as support human life. So, an average of 70-80kPa can be maintained inside the habitat. The International Space Station has the same pressure, and is similar to that of a standard Boeing Aircraft's cabin pressure. The habitat should thus have depressurization and pressurization systems to control the habitat's environment. This way, the safety of both the structure and human life is taken care of. Temperature is also another important factor. The average temperature on Mars is -63degC. So the internal temperature should also be chosen appropriately. Internal temperature of 20-30degC would suit the needs of the humans. Again, the average temperature inside the ISS is 24degC. And this will be taken care of by the temperature control and regulation systems, pertaining to the needs of the astronauts. The inflation of the structure will take place after landing on the Martian

surface. It can be done using air (mixture of O₂, N₂ and H₂) which can be extracted from the atmosphere of Mars.

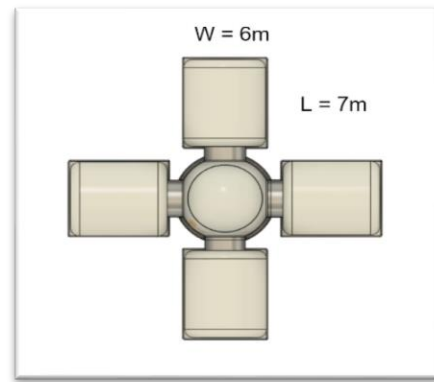


Figure 4: Top view of the habitat

4.4 Dimensions and Volumetric Analysis

The next logical step would be to find precise dimensions of the structure, as per the requirements. Taking inputs from the available references such as the International Space Station, Space Shuttle and Bigelow Aerospace's inflatable modules, and considering the volumetric requirements, the dimensions have been arrived at

4.4.1 Dimensions

- For hemispherical dome,
 - Diameter = 6m
 - Height (radius) = 3m.
- For semi-cylindrical module(s),
 - Diameter = 6m
 - Length = 7m

- Height (radius) = 3m.

4.4.2 Volume calculations from values

- Volume of hemispherical dome,

$$\frac{2}{3} \pi r^3 = 56.55 \text{ m}^3$$

- Volume of semi-cylindrical modules,

$$4 \times \frac{\pi r^2 h}{2} = 395.84 \text{ m}^3$$

- Total volume,

$$V = 452.39 \text{ m}^3$$

The dimensions have been decided while catering to the needs of a crew of four extendable upto 6. The volumetric requirements are also based on the various sections like living quarters which consist of kitchen, toilet, gym and medical bay, greenhouse and scientific laboratory.

4.4.3 Stress Calculations

All the individual modules are essentially pressure vessels. So the internal pressure exerts tensile stresses on the inner walls of the structure. There are basically two types of stresses that would be induced -

Longitudinal stress and Hoops (or circumferential stress). The design should be in such a way that the structure withstands these stresses, thereby ensuring safety. This will be discussed in detail in the Materials' section.

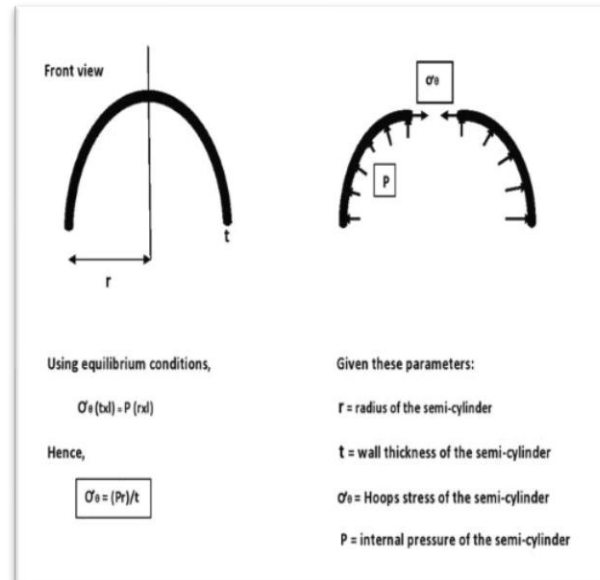


Figure 5: Hoops stress for semi cylindrical structure

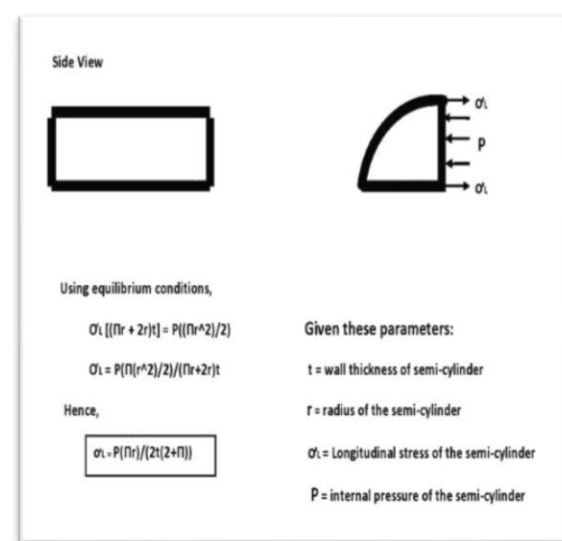


Figure 6: Longitudinal stress for half-cylinder

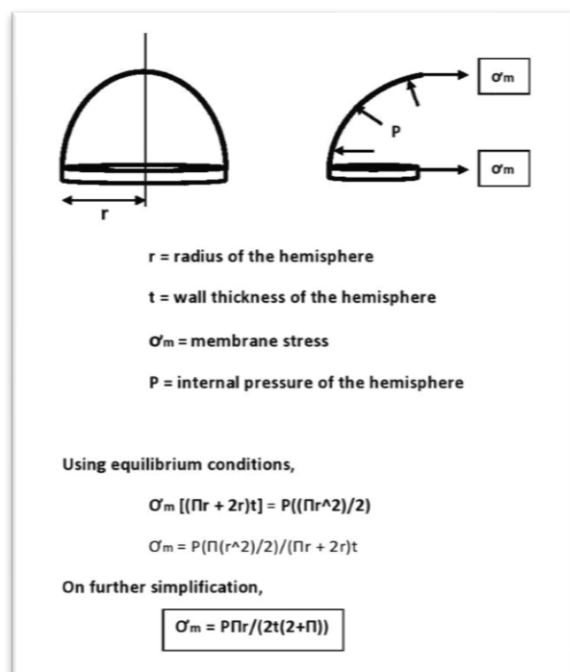


Figure 7: Membrane stress for hemisphere

Now to calculate the stresses, the value of wall thickness (t) should be known. So the thickness is taken to be 0.5m. This is in accordance with the references taken into consideration. One major reference is Bigelow Aerospace's B330 module, which is an inflatable space station under development. They are also working on building a Martian habitat, under similar design requirements. This value of thickness is therefore suitable for our project too. And since this structure is a thin-walled pressure vessel, this value is justifiable.

- Assumed values,

$$P = 80\text{kPa}$$

$$t = 0.5\text{m}$$

$$r = 3\text{m}$$

- Hoops stress for the semi-cylindrical structure,

$$\sigma_h = \frac{Pr}{t} = 480\text{kPa}$$

- Longitudinal stress for the semi-cylindrical structure,

$$\sigma_L = \frac{P \pi r}{2 t (2+\pi)} = 146.63\text{kPa}$$

- Membrane stress for the hemispherical dome,

$$\sigma_m = \frac{P \pi r}{2 t (2+\pi)} = 146.63\text{kPa}$$

5. Materials

The Inflatable Habitat deals with Structures as well as Materials. The success of this entire mission relies heavily upon the grade of the materials used. These materials must be able to withstand the environment of Mars.

As discussed earlier, such materials must exhibit very good mechanical properties. And for this mission, six candidate materials have been shortlisted (for any space mission in general) – Kevlar, Vectran, Dacron, Zylon, Technora and Spectra. All these

materials exhibit very good properties. But – Kevlar and Vectran prove to be the most promising ones. To understand this, one must know the shielding requirements for the habitat.



Figure 8: Cross-section of the habitat showing the different layers of shielding.

Out of these, Vectran is the most suitable material because of its unique combination of all required mechanical properties of the material. One major advantage of using Vectran is that its tensile strength is very high and it increases with decreasing temperature. Since the Martian temperature is very low (minus 63degC on an average), this material would be the best choice. It also has high creep resistance, impact tolerance, radiation resistance, flex/crack/abrasion resistance. It is used for ballistic applications like bullet-proof vests because it is capable of withstanding impacts created by particles of 2cm hitting it at 10km/sec, making it preferable for Micrometeoroid Shielding too. The strength of the structure can be enhanced by using a

combination of Kevlar and Vectran to shield the habitat, with Kevlar being used for the structural restraint layer. This will act as a reinforcement for the structure, thus providing better resistance to internal pressure, higher puncture resistance and also facilitating gas retention.

The innermost layer will be made up of Vectran, that is fire-proof and directly takes the stresses. It has high flexibility, tensile strength and puncture resistance, making it highly preferable. So the inflation will be smooth. Next is a layer made of Kevlar. Now in between these Kevlar and Vectran layers, air is filled. This acts as an insulation to ensure that there is no heat exchange across the layers. This Kevlar layer also acts as a structural restraint, which enhances the overall strength of the structure. It also distributes the stresses equally and facilitates uniform inflation. The next is the outer layer again made up of Vectran. This layer is thick and is directly exposed to the Martian environment. This acts as the layer that provides shielding from radiation, temperature and micrometeoroids. Thus, this structure would be highly safe and stable for the operation of the habitat. In addition to the synthetic shielding layers, a layer of Martian regolith can also be used to provide enhanced shielding from radiation and micrometeoroids damage. This ensures longer operational life of the habitat.

6. Stowed Configuration for Vehicle Payload

An inflatable habitat designed for interplanetary missions needs to be carried from earth to that planet in a rocket in a very compact structure. The inflatable habitat is designed for SpaceX's Starship Super Heavy Lift Vehicle, which has fairing dimensions of 9m diameter and 15m height. The stowed payload is the compacted and deflated form of the habitat that fits in the vehicle fairing. Figure.7 shows the three-dimensional model of the stowed configuration of the inflatable habitat.

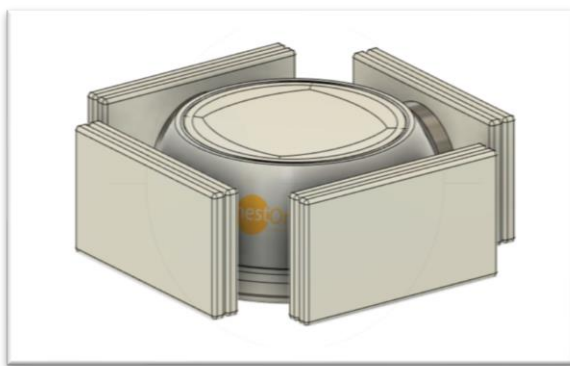


Figure 9: 3D representation of the stowed configuration

The stowed configuration has a central dome in two parts. The lower wall of the dome is a semi-rigid structure and the upper part, which is inflatable and made out of flexible materials along with layers for shielding. The solid airlocks are retracted to save space in the payload. The semi-rigid base of the uninflated semi-cylindrical

modules is folded into half and attached through the inflatable material to the retracted airlock entrances. The payload also consists of cargo inside the semi-rigid dome that consists of essential ECLSS subsystems to prepare the deployed habitat autonomously in the pre-crew phase, gas cylinders, fuel cells to power the habitat, essential lighting, etc.

7. Deployment

Once the stowed configuration of the habitat has landed on the surface of Mars, it needs to deploy, inflate, and prepare the cabin atmosphere and other necessities into a functional habitat for crew arrival. The deployment of an inflatable habitat is comparatively less complex than a mechanised system. During the deployment phase, the first step is the extension of the retracted airlock frame. Then, the semi-rigid base of each of the side modules extends outwards till it becomes horizontal on the surface of Mars. Once the base of the modules has been set in place, the airflow pumps are activated and the walls of the semi-cylindrical modules, and the upper half of the dome are inflated. The primary airlock entrance is deployed in the entrance module, and the system powers up the ECLSS subsystems to prepare the cabin atmosphere, the In-Situ Resource

Processing system (ISRPS), and the Water Reclamation System (WRS).



Figure 10: Deployment stages

(a) Stowed configuration

(b) Half deployment with module bases Extended

(c) Fully deployed habitat

8. Power Source

In order to power the Martian habitat, many sources of power have been identified and theorized by scientists and NASA, SpaceX and other space research organizations and institutes. Some of the sources of power that have been used to power rovers in previous NASA space missions include:

8.1 Solar Energy

Solar panels have an area of approximately 10 square meters (107.6 square feet) and contain 3,744 individual solar cells. The solar cells are able to convert more than 26% of the Sun's energy directly into electricity so that the power they produce is 32 volts, the voltage that most devices on the spacecraft need to operate properly. At Mars, the two panels together produce 1,000 watts of power.

8.2 Nickel Hydrogen Batteries

Nickel-hydrogen rechargeable batteries can be used to power the habitat's power systems, each with an energy storage capacity of 50 ampere-hours -- at 32 volts

that's 1,600 watts for one hour. However, to ensure there is no power failure, only a maximum of 40% of the battery can be utilized at a time.

8.3 Fuel Cells

Fuel cells are one of the most sought-after inventions because it converts chemical energy from hydrocarbon fuels directly into water and electricity causing little to no pollution. The water produced from fuel cells can also directly be sent to the Water Reclamation System, which after purification can be utilized by the astronauts in the habitat itself.

This report will take into account Solar Cells and Nickel-Hydrogen Batteries as power sources as well as fuel cells which have been explained.

9.In-Situ Resource Utilization

In-Situ Resource Utilization (ISRU) is a means of harvesting essential commodities like power, food, oxygen and other necessary gases to support long-term human and robotic exploration efforts on Mars. The Martian atmosphere contains many useful resources that can be utilized for exploration efforts, including carbon dioxide

that can be used to produce oxygen, methane, and water.

The Martian atmosphere consists of about 95.5% CO₂, 2.7% N₂, 1.6% Ar, 0.13% O₂ and 0.07% of other gases. CO₂ from the atmosphere can be extracted using various techniques such as CO₂ freezing, use of membranes, acid-base chemistry, chromatography and molecular sieves. After extraction, CO₂ has to be refined from trace chemicals and can be used as a valuable resource in the following manner:

1. Reforming CO₂ and trace amount of CH₄ to produce fuel gas using Fischer Tropsch process so as to power the habitat and the ECLSS..
2. Using CO₂, on biohybrids with the presence of water and sunlight to create organic molecules and oxygen.
3. Control the O₂ level in the greenhouse module by addition of CO₂.
4. Utilize Martian CO₂ to produce O₂ that can be utilized in the atmospheric control system for Astronauts.

N₂ and Ar present in the Martian atmosphere can also be collected so as to be used for buffer purposes. The scope of this report deals only with the utilization of CO₂ for the production of lower hydrocarbon fuels such as methane, ethane and methanol as well as the utilization of these fuels in a

fuel cell that can be used to power the ECLSS subsystems.

9.I Fuel production from a Martian atmosphere

Synthetic fuel can be produced by the Electro-Chemical Reduction (ECR) of CO₂, which can be a viable way of powering the ECLSS system. The flow of the system will be as follows: CO₂ captured from the atmosphere will be reduced electrolytically to CO. The electricity will be obtained from solar cells which store energy using the solar concentrators located on top of the habitat. The reduced CO will be separated from the unreacted CO₂. The unreacted CO₂ can be recycled while the separated CO will continue to the Fischer Tropsch or FT. In the FT, H₂ released from the hydrolysis of water to produce O₂ can be used to be combined with CO and produce synthetic fuel gas.

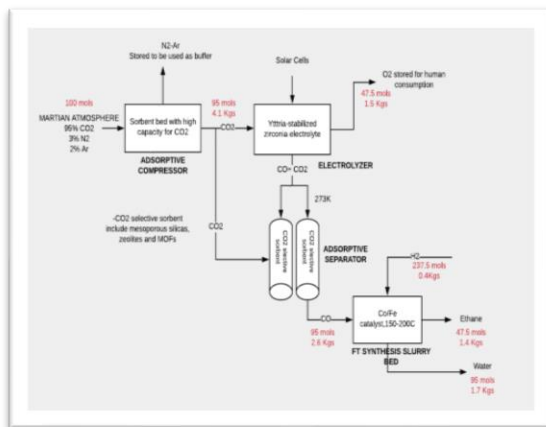


Figure 11: Ethane fuel from CO₂ block diagram

9.I.I Adsorptive Compressor

In the above process, we are separating CO₂ from the remaining gases by the use of an adsorptive compressor having a sorbent bed with a high affinity for CO₂. Usually, CO₂ selective sorbents include mesoporous silicas, zeolites and metal oxide frameworks(MOFs). The sorbent bed absorbs CO₂, and vents out N₂ and Ar which can be stored and used as a buffer. CO₂ is absorbed till maximum capacity after which it is heated to raise the internal pressure of the compressor to 1 bar. Carbon dioxide gets desorbed and is vented out to the electrolyzer. Meanwhile, the compressor cools down until reaching environmental pressure.

Suggested sorbent: Lewatit VP OC 1065
(Ion Exchange Resin)

9.I.2 Solid Oxide Electrolyzer

The vented CO₂ enters the electrolyzer, where it undergoes electrocatalysis and/or thermal dissociation produces O₂ at the anode. The CO formed at the cathode, as well as unreacted CO₂ are sent to a separation chamber. The electrolyzer requires DC voltage which can be obtained from solar powered batteries. The electrolyte used is a Yttria-Stabilized Zirconia (YSZ) electrolyte. Water from frozen Martian water is sent to an

electrolyzer. Oxygen produced at the anode is sent to AMS for human consumption.

Overall Reaction,



Suitable Temperature Range,

700-900 degC

Voltage Required: At 25 °C, ΔG_f is 257 kJ mol⁻¹, which corresponds to a reversible voltage of 1.33 V. At 800 °C, ΔG_f is only 189 kJ mol⁻¹ or 0.97 V

9.I.3 Adsorptive Separation

The CO and CO₂ mixture passes through a sorbent bed containing CO₂ selective material. The feed enters the sorbent bed at 273 K, and CO passes through the bed while the CO₂ gets absorbed until full capacity. At this point, the CO₂ is desorbed from the bed by heating it to 373 K and recycling the CO₂ into the electrolyzer. The bed is then cooled back to 273 K and the flow is started again. CO is sent to a FT synthesis slurry bed.

9.I.4 FT synthesis slurry bed

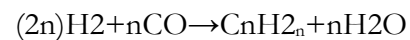
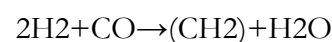
The CO and H₂ enter the Fischer Tropsch synthesis slurry bed. The Fischer-Tropsch process is a catalytic chemical reaction in

which carbon monoxide (CO) and hydrogen (H₂) in the syngas are converted into hydrocarbons of various molecular weights according to the following equation:



$$\Delta H = -165 \text{ kJ/mol}$$

Fe or Co metal catalysts are suitable for FT synthesis. Fe is a better catalyst at higher temperatures and reduces methane formation. Co is a good alternative to Fe, but operates at lower temperatures and promotes methane formation. It has a longer lifetime. The reaction takes place at 200 – 300 °C and 10 bars. Other general reactions are,



Since the reaction is exothermic, a cooling system is required to maintain the temperatures at a required heat range.

Catalyst suggested: Fe-K/ZSM-5

10. Life Support System

The Environmental Control and Life Support System or ECLSS is hardware technology based on principles of regeneration from waste matter, to support and sustain a healthy lifestyle for the crew in

the habitat. The primary role of the ECLSS is atmospheric control, waste management and water regeneration. The ECLSS also plays an important role in linking the output of the ISRPS with the appropriate subsystem.

10.1 Waste Management System (WMS)

The whole waste from the habitat can be broadly divided into two classes namely recyclable and non-recyclable. Storage buffers are required throughout the ECLSS to accommodate nominal variations in production and consumption and to accommodate and recover from contingency conditions (e.g. unplanned repair activities).

The human metabolic waste and food waste can be classified into recyclable waste. The medical and the other waste (which includes the waste from plants etc.) can be classified into non-recyclable waste as shown in the hierarchy chart (figure1).



Figure 12: Hierarchy chart of WMS

The representative life support inputs and outputs for a typical human being are shown in figure 2. The WMS has to be designed based on the values.

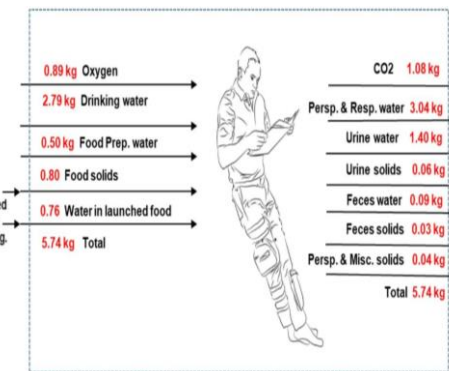


Figure 13: Output waste quantities of a person per day

10.1.1 Human metabolic waste-collection and storage.

The human metabolic waste consists of solid and liquid waste, the two waste are collected separately in the toilets and stored in the aluminum storage containers which can accommodate 0.13kg/per human being/per day of solid waste and

4.53kg/per human being/per day liquid waste.

10.1.2 Food waste- collection and storage.

The food waste consists of two classes of waste one of them are containers (non-

recyclable) and the other being leftover food. The two classes of waste are to be collected in separate aluminum containers and stored.

I0.I.3 Non-recyclable waste management system.

The non- recyclable waste should not contaminate the Martian surface so it has to be sealed in the air tight container and buried into the Martian soil with disinfecting systems.

I0.I.4 Medical waste collection and storage

All the medical waste is to be collected in an aluminum container.

I0.I.5 Miscellaneous waste

This contains the waste of plant waste, human grooming waste, e-waste. These are to be collected into aluminum containers.

I0.2 Water Reclamation System

The Water Reclamation System (WRS) mainly focuses on the objective on recycling used water in habitat. The WRS consists of

various treatment processes for generating treated pure water, and potable water. The Potable water is used by the crew for hydration and cooking. It also consists of storage tanks and sensor controlled valves to control the flow of pure water to other subsystems where it is required, and to the cabin. The system gets water from the ISRPS, cabin humidity, hydration system and moisture from Extra Vehicular Activity suits, and from transpiration of plants in the greenhouse module, and from the waste recycling.

The water which is recovered must meet stringent purity standards before it can be used in various ways.

I0.2.I Reusable Waste Processing Assembly (RWPA)

The Reusable waste processing assembly (RWPA), takes the inputs from biological payloads, plants waste and produces manure, methane, carbon dioxide and small amounts of water as the output.

The manure preparation requires the correct mixture of soil and the degradable biomass, the regulators attached to each collection and storage system extracts the predetermined ratio of biomass and sends it to the Reusable waste processing assembly (RWPA). The soil extracted from the Martian surface has to be screened and only fine powered sand is to be pumped into the

pit. The processing pit undergoes the conversion process for 50 days and produces the manure and by-products. The manure is sent to the greenhouse and the methane and carbon dioxide is sent to the fuel generation system. The water generated from RWPA is sent to the water processor assembly (WPA) which can be processed and used for the biological payloads. The block diagram in figure 12 shows the processes involved in the RWPA.

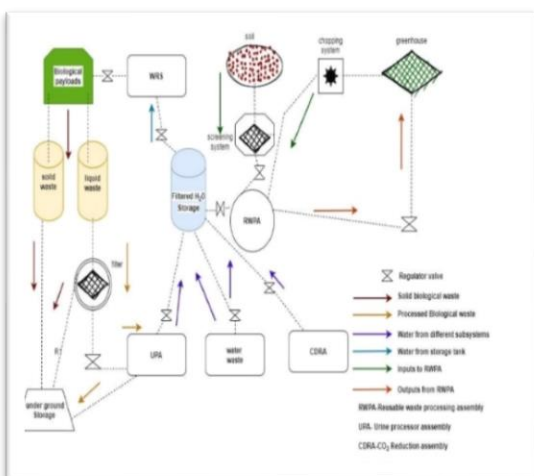


Figure 14: Block diagram of Waste Management System.

10.2.2 Urine Processor Assembly (UPA)

A simplified schematic of the Urine Processor Assembly (UPA) is shown in figure 13. Urine is delivered to the UPA from the liquid waste container of biological payloads as shown in figure 3. The urine is temporarily stored in the Waste water Storage Tank Assembly (WSTA) until it reaches a setpoint to begin processing. The

Fluids Control and Pump Assembly (FCPA) is a four-tube peristaltic pump which moves urine into the Distillation Assembly (DA), concentrated waste from the DA into the Recycle Filter Tank Assembly (RFTA), and product water to the interface with the WRS. The DA is the heart of the UPA, and consists of a rotating centrifuge where water is evaporated from the waste urine stream at very low pressure. A rotary lobe compressor provides the driving force for the evaporation and compression of water vapor. Waste brine resulting from the distillation process is concentrated in the RFTA. The Pressure Control and Pump Assembly (PCPA) is another fourth tube peristaltic pump, which removes non-condensable gases and water vapor from the DA. These gases are pumped to the Separator Plumbing Assembly (SPA), which recovers and returns water from the purge gases to the product water stream. A Firmware Controller Assembly (FCA) provides the command control, excitation, monitoring, and data downlink for UPA sensors and effectors.

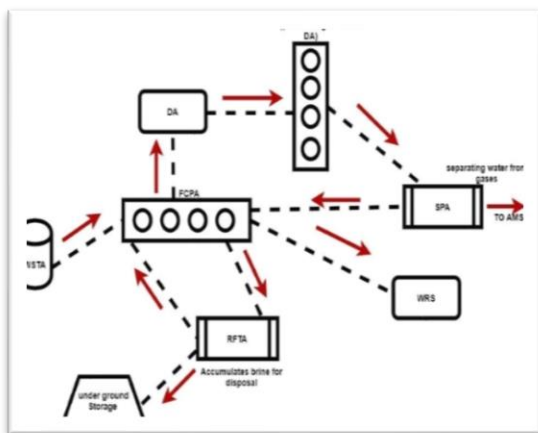


Figure 15: Block diagram representation of UPA

10.2.3 Distillation Assembly (DA)

The Distillation Assembly (DA) is the primary component in the UPA. The processes in DA are of two phases. The first phase of the process is done under vacuum and the second phase is done under microgravity. At a maximum load, the UPA² can process 13.6 kg (30 lbs.) of wastewater over an 18-hour period per day. It operates in a Batch mode, consuming 424 W power when processing, and 108 W during standby. And recovers a minimum of 85% of the water content in the specified wastewater stream.

Urine is pumped into the DA from the FCPA. It enters the rotating evaporator through the feed tube (Figure 5). The urine is spread onto the evaporator wall in a thin film that travels the length of the evaporator until it is collected in the urine/brine trough

and pumped out by the FCPA through the evaporator pickup tube. As it travels down the wall of the evaporator, water is evaporated from the urine. The steam that is generated is pumped through the centre of the hollow stationary shaft and compressed in the condenser by the compressor. Once the steam's pressure is raised, it begins to condense and give up its latent heat to the evaporator. This latent heat plus the waste heat generated from the compressor and motor are what provide the energy for the evaporation of water from the urine. The steam then condenses and, due to centrifugal force, collects on the outer wall of the condenser and travels to the product water trough. There it is pumped out of the condenser by the FCPA through the product water pickup tube. This entire process is done under vacuum. The vacuum is contained by the stationary bowl which surrounds the rotating still and compressor.

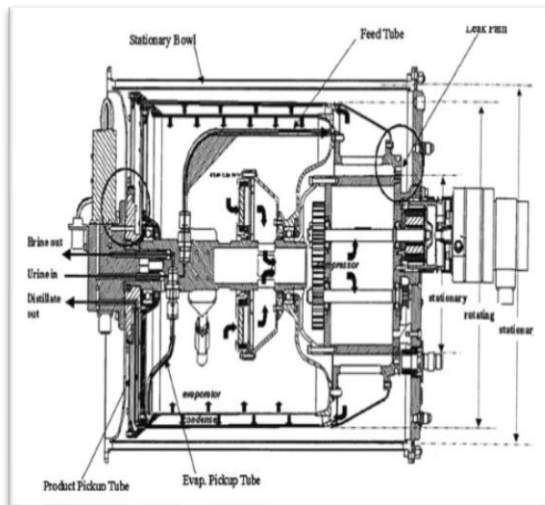


Figure 16: Cross-section of Distillation Assembly

The two-phase operation is controlled in microgravity by the centrifugal force of the rotating still. This allows the DA to control the location of liquid and steam in the DA so that the evaporation and condensation process can take place and the liquids can be pumped into and removed from the DA.

10.2.4 Pre-treatment of liquid waste in WSTA

There are two methods employed for pretreatment one followed by NASA and other by Roscosmos there are detailed in the table below. The table also contains Total organic Carbon (TOC) ,Total Inorganic Carbon(TIC), pH and Conductivity.

PARAMETER	U.S PRE-TREATMENT	RUSSIAN TREATMENT
Pre-treatment Chemicals	Oxone/sulfuric acid/potassium benzoate	Chromium Trioxide/Sulfuric Acid
TOC	150 mg/liter	55 mg/liter
TIC	-	1.1 mg/liter
PH	3.2	3.15
Conductivity	137 umhos/cm	150 umhos/cm

Table 1: Water quality data, indicating that the Russian pre-treatment may actually improve water quality.

10.3 Atmospheric Management System (AMS)

The Atmospheric Management System or AMS mainly deals with the Carbon Dioxide control, Oxygen Production, Atmospheric Circulation, Atmosphere Particulate Control, Trace Contaminant Control, Fire Detection and Notification, Post-Fire Atmospheric Recovery, Atmosphere Temperature and Humidity Control. Maintaining the proper pressure is required for crew comfort and survivability as well as habitat structural limits. AMS shall revitalize and maintain a safe, breathable and comfortable atmosphere for the crew and equipment within the habitat. Maintaining proper O₂, CO₂, trace contaminant concentration, humidity and air circulation through the habitat ensures crew comfort. Ventilation is needed for thermal control and air circulation. Proper cabin atmosphere maintenance is also necessary for the proper functioning of other subsystems designed for that particular condition inside the habitat.

10.3.1 Atmosphere circulation

Variable speed fans circulate the habitat air to provide homogeneous air mixture, heat

transport and movement of air through the various units that revitalize the air. Habitat fans are nominally controlled by the master computer and only switched off during contingency operations like fire to stop the spread of harmful chemicals till the system contains them.

10.3.2 Atmosphere Particulate Control

High-efficiency particulate absorbing filters (HEPA)⁶ will be attached to the fans and air intake in the habitat. These filters can remove particles of 0.3 micrometer diameter and make air safe to breath.

10.3.3 Trace Contaminant Control

Trace Contaminant Control System (TCCS) removes most hazardous contaminants from the habitat using a carbon bed, but some must be destroyed in high temperature catalytic oxidizers. TCCS should be designed to maintain the level of trace contaminants in the atmosphere of habitat below the allowable concentration. Over 214 particles¹⁸ have now been identified, including the alcohols, aldehydes, aromatics, ethers, ester, halocarbons, fluorosilanes, hydrocarbon, kittens, silicones, sulphides, and inorganic compounds such as carbon monoxide. Majority of the contaminants are removed from the atmosphere by charcoal beds and

others are removed by the water revitalization system. However, highly volatile low molecular weight compounds such as light hydrocarbons (Methane, acetylene, ethylene and ethane), carbon monoxide, light hydrocarbons (chloromethane, dichloromethane, and freon 22) and sulphur compounds like hydrogen sulphide have little affinity for activated carbon, and must be catalytically oxidised.

Cabin air enters the activated carbon bed at roughly 250 litres¹⁸ per minute. The activated carbon readily absorbs most contaminants including a variety of compounds that contain sulphur, nitrogen and halogens that would poison the catalyst. In addition, the carbon bed is impregnated with phosphoric acid to absorb ammonia before it reaches the oxidizer. A small portion (70 litre per minute) of the air leaving the activated charcoal bed is sent to a high temperature catalytic oxidizer. The air entering the oxidizer is heated to 400 degree Celsius by the regenerative heat exchanger and resistance heater. The catalyst oxidises the organics to carbon dioxide and water and converts the inorganic compounds to acidic gases such as HCl, HF and SO₂. The air leaving the catalyst bed is cooled in the regenerative heat exchanger and passed through a little hydroxide array, bade that is removed in acid by products produced during the oxidation process. Thus, TCC

from the cabin air is removed with activated carbon and high temperature catalytic oxidation assembly¹⁸.

10.3.4 Fire detection and notification

Fire detection consists of dedicated carbon monoxide sensors as well as particulate smoke detectors throughout the habitat that continuously monitor habitat air circulating through the habitat along with the additional carbon monoxide measurements provided by the atmosphere quality monitoring system. The habitat master computer is notified of any fire event. Portable fire extinguishers (PFE) will be used for fire suppression. The implementation would be similar to that of the CO₂ portable Fire extinguisher currently employed on the ISS. The PFE would be designed to be refilled by crew. We will not depressurise the habitat in any fire event instead the habitat compartment will be automatically separated from habitat by air lock to reduce further damage of habitat

10.3.5 Post-fire Atmosphere Recovery

Recovering the atmosphere after the fire event and making it suitable and breathable for crew will be done by a post fire atmospheric recovery system. The post fire atmosphere recovery provides for the removal of harmful post combustion products such as particulate, traces, organic

compounds, carbon monoxide and carbon dioxide without the need of depressurization of the atmosphere and the pressurization with stored gas. The subsystem utilizes the existing

HEPA filters to remove 99.97% of airborne particulates 0.3 microns or greater in particle diameter. A cartridge inserted in the ARS air stream by the crew following a fire event utilizes granulated media to remove organic compounds and converts CO to CO₂.

Generated CO₂ is removed by CO₂ removal assembly.

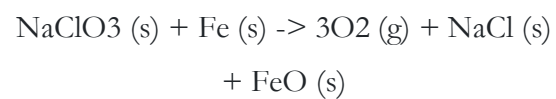
10.3.6 O₂ Generation System

The Oxygen Generation System produces oxygen for the crew to breathe. The system consists of the oxygen generation assembly and the carbon dioxide reduction assembly.

The oxygen generation assembly is composed of the cell stack, which electrolyzes water provided by the WRS, yielding oxygen and hydrogen as by products. The oxygen is delivered to the cabin atmosphere while the hydrogen is stored to be used by other subsystems. The assembly uses that hydrogen along with carbon dioxide exhaled by the crew in a Sabatier reactor.

The by-products of that process are methane and water for storage in the WRS.

Another backup system that makes oxygen through chemical reactions. The system is called the Solid fuel oxygen generator (SFOG) and is located in the station's service module (Zvezda). The SFOG, which is also called oxygen candles or chlorate candles, has canisters that contain a mixture of powdered sodium chlorate (NaClO₃) and iron (Fe) powder. When the SFOG is ignited, the iron "burns" at 1112 degrees F (600 degrees C), which supplies the heat energy required for the reaction. The sodium chlorate breaks down into sodium chloride (table salt- NaCl) and oxygen gas (O₂). Some of the oxygen combines with iron to form iron oxide (FeO) at 600°C



The SFOG supplies 6.5 man-hours of oxygen per kilogram of the mixture³.

10.3.7 Atmospheric Humidity and Temperature Control

Warm humid habitat is circulated across a condensing heat exchanger to cool the air and condense the water vapour into liquid. The flow of active thermal control system (ATCS) supplied chilled coolant through a liquid gas heat exchanger is regulated by a bypass valve to affect the required air temperature control. The non-potable condensed water is collated and transferred

to the WRS for further processing. The cool dry air is returned to the habitat atmosphere.

10.3.8 Carbon Dioxide Removal System

The block diagram depicts the Carbon Dioxide Removal Assembly(CDRA), the Oxygen Generation Assembly(OGA), and the Carbon Dioxide Reduction Assembly(CRA). The CDRA collects and concentrate carbon dioxide and feeds it's to the CRA. The OGA electrolyzes the water for oxygen and feeds the by-product hydrogen to the CRA. The CRA reacts hydrogen and carbon dioxide to form methane and water. The water is returned to the OGA, thus partially closing the oxygen loop. The CMS includes the mechanical compressor and accumulator. As of now, with existing improved technology, the previous 4 bed molecular sieve CDRA has been updated.

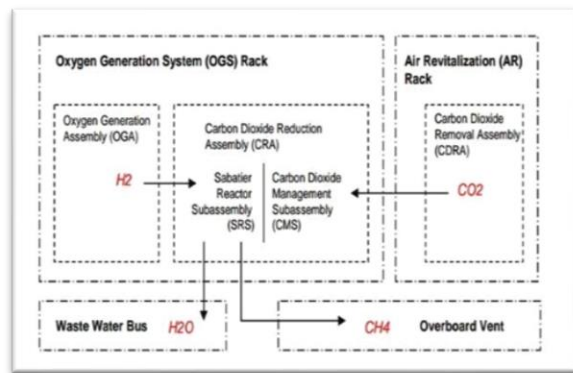


Figure 17: Block diagram representation of the AMS

10.3.9 Four – Bed Molecular Sieve (4BMS) Carbon Dioxide Removal Assembly (CDRA)

Four bed molecular sieve process consists of two desiccant beds and two carbon dioxide sorbent beds. Additionally, it includes blower, air-save pump, heat exchanger, valves and sensors. Cabin air is monitored and drawn towards one of the desiccant beds to remove the moisture and then passes through the sorbent bed to remove carbon dioxide. Processed air is thereby sent through the second, heated desiccant bed to re-humidify the stream before returning the air back to the cabin. At the same time, the second sorbent bed, which is loaded with carbon dioxide, is heated and evacuated to desorb the carbon dioxide. The vacuum circuit runs from the desorbing bed check valve to space vacuum (represented as yellow line).

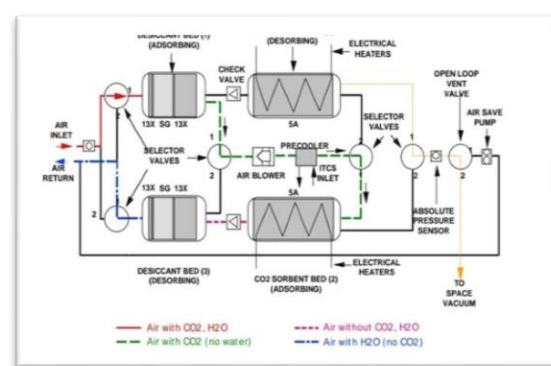


Figure 18: Block diagram representation of CDRA

In half the cycle, one bed is doing all the carbon dioxide removal functions. At the next half cycle, all beds switch to opposite mode and cabin air flow swings to the other set of adsorbent beds, the alternate bed then performs the carbon dioxide removal function. CDRA followed by compressor are used for compression of carbon dioxide for efficient storage and controlled delivery to the Sabatier. The compressor is designed out for oil free so that no oil contamination is introduced to the Sabatier reactor.

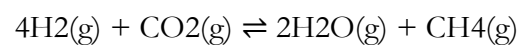
Accumulators are used for buffering capacity to integrate 4BMS and Sabatier when using a mechanical compressor. Due to space limitation within the OGA rack where the CRA hardware would be located, the total accumulator volume is achieved by hanging several small vessels together.

10.3.10 Sabatier CRA

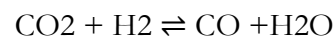
Sabatier consists of Sabatier reactor, a condensing heat exchanger, a phase separator, and necessary valves and sensors. Carbon dioxide from CDRA and hydrogen from OGA combines to produce methane and water. Water is sent to the Waste

Management System for processing it to potable water. Methane is used as a fuel source. Reaction in a catalyst reactor is reversible, highly exothermic. Ruthenium and nickel are found to be appreciably more active catalysts for promoting the Sabatier

reaction. But Nickel causes slow deterioration over the period and carbon deposition is reported at 650-700°F. A hydrogen cylinder and a flow controller are used to simulate the delivery of H₂ from an OGA. Water vapor in the product stream is condensed in an air-cooled heat exchanger. The methane gas and liquid water are separated in a rotary drum phase separator.



Sabatier CRA has two primary modes of operation: Process and Standby. In Process mode, inlet gases flow through the system and methane and water are produced. In Standby mode, supply gases and the system is isolated, coolant air is stopped. Low temperatures favor high conversions. At 700°F and a feed ratio (H₂ : CO₂) of 3.5:1 the equilibrium conversion of H₂ is only 90%, while at 400°F it is about 99%. As the feed ratio falls below 3.5:1, carbon becomes thermodynamically stable at higher temperatures. Carbon monoxide formation is thermodynamically possible above 700°F.



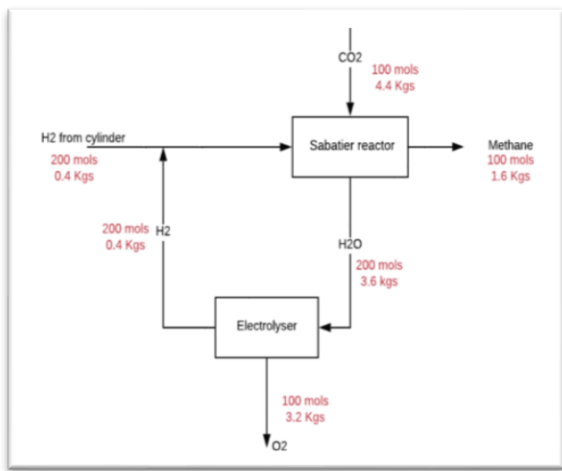


Figure 19: Block diagram of the Sabatier and OGS showing the quantities of materials

II. Results and Conclusions

A conceptual inflatable habitat was designed. A structure for the habitat was finalised after considering different configurations like Habitat Designs for Lunar and Martian Missions, and Inflatable Space Station Modules. Stress and Volumetric Analyses were performed for the structure of the habitat. A 3D model was developed for the habitat, and its stowed configuration and deployment were conceptualised. Environmental factors that would affect the habitat and materials to be used in each layer of the inflatable habitat were studied. The entire habitat was divided into sections which would house specified activities. ECLSS was designed for the

habitat for a crew size of 4 (expandable upto 6), for a duration of 4 months. In addition to these, various technologies were studied to utilise the resources present on the planet and make the habitat self-sustainable.

12. References

- [1] Astronaut Mass Balance for Long Duration Missions. Michael K. Ewert, NASA Johnson Space Center, Houston And Chel Stromgren, Binera, Inc.,
- [2] Development Status of the International Space Station Urine Processor Assembly, Donald W. Holder and Cindy F. Hutchens, NASA Marshall Space Flight Center
- [3] George C . Marshall Space Flight Center, ISS Environmental Control and Life Support System www.nasa.gov/marshall
- [4] Harry.W.Jones, Life Support for Deep Space and Mars, 44th International Conference on Environment System 13-17 july 2014
- [5] Jay L. Perry, Functional performance of an Enabling atmosphere reventilisation subsystem Architecture for deep space Space Exploration mission, American Institute of Aerospace and Astronautics

- [6] Barry W Finger, PARAGON, Mars One Habitat ECLSS Conceptual Design Assessment, WWW.paragonSDC.com
- [7] Finckenor, M. M., Comparison of High-Performance Fiber Materials Properties in Simulated and Actual Space Environments, Technical Memorandum (TM), July 1, 2017 <https://ntrs.nasa.gov/citations/20170006996>
- [8] Murray, E., Tsai, T. & Barnett, S. A direct-methane fuel cell with a ceria-based anode. Nature 400, 649–651 (1999). <https://doi.org/10.1038/23220>
- [9] Jo-Yong Park, Yun-Jo Lee, Ki-Won Jun, Jong Wook Bae, Nagabhatla Viswanadham, Young Ho Kim, Direct conversion of synthesis gas to light olefins using dual bed reactor, 2009, <https://doi.org/10.1016/j.jiec.2009.09.011>
- [10] Robertz. M, Inflatable Habitation for the Lunar Base, NASA Johnson Space Center.
- [11] Cadogan. D, Stein. J, Grahne. M, Dover. ILC, Inc. Inflatable Composite Habitat Structures for Lunar and Mars Exploration, Acta Astronautica, 1999.
- [12] Kriss. J. Kennedy, Inflatable Habitats Technology Development, NASA Johnson Space Center, 2000.
<https://ntrs.nasa.gov/citations/20050182969>
- [13] Inka Hublitz, Engineering Concepts for Inflatable Mars Surface Greenhouses, Division of Astronautics, Technische Universität München, Germany., NASA Johnson Space Center, Houston, Texas.
- [14] AI Globus, Ankur Bajoria, Nitin Arora, Kalpana One: A New Orbital Space Colony Design, American Institute of Aeronautics and Astronautics.
- [15] Simon. M, Whitmire. A, Otto. C, Neubek. D, Factors Impacting Habitable Volume Requirements: Results from the 2011 Habitable Volume Workshop, Center for Advanced Space Studies-Universities Space Research Association, Houston, Texas, 2011.<https://ntrs.nasa.gov/citations/20110023287>
- [16] Kuraray America, Inc, Vectran: Grasp The World Of Tomorrow - Liquid Crystal Technology.
- [17] James. W. Head, The Geology of Mars: New Insights and Outstanding Questions,

Department of Geological Sciences, Brown University.

- [18] John D. Wright, an Investigation of International Space Station trace Contamination

Oxidation Catalyst Poisoning , SAE International.

Study of eccentricities in Planetary Systems stabilized by Orbital Resonance – A Hamiltonian Approach

AUGUST 2020



Study of eccentricities in Planetary Systems stabilized by Orbital Resonance – A Hamiltonian Approach

Internal Mentor - Mr. Sundar M.N.
External Mentor - Dr. Parshati Patel



Our Team

1. Aayushi Doshi; 40312180384; Mithibai College (Autonomous), University of Mumbai, Mumbai.
2. Agamleen Singh; 28718001095; Department of Physics, Panjab University, Chandigarh
3. Athul Dev SP; CB.SC.I5PHY18017; Amrita Vishwa Vidyapeetham, Coimbatore.
4. Avinaba Majumdar; 001/18/XI/062; Techno India Group Public School, Hooghly, West Bengal.
5. Bhawna Dhawan; 28718001085; Department of Physics, Panjab University, Chandigarh.
6. Komal Kaur; 28716000034; Department of Physics, Panjab University, Chandigarh.
7. Manreet Kaur; 18059098; (Panjab University, Chandigarh) Government College for Girls, Ludhiana.
8. Prakruti S.; 1740474; Christ (Deemed to be University), Bangalore.
9. Rutuja Attal; 1711111; National Institute of Science Education and Research Bhubaneshwar.
10. Shivam Jaiswal; AIT17BEAE057; Acharya Institute of Technology Bengaluru.

11. Shraddha Puri; 28718001091; Department of Physics, Panjab University,

Chandigarh.

12. Srivardini A.; 19374055; Pondicherry University, Pondicherry.

ACKNOWLEDGEMENT

The Exoplanets team of SSERD Internship and Project Division would like to express sincere gratitude to all the Mentors and Guides of the SSERD Team who made this project successful including Mr. Sujay Sreedhar, Ms. Nikhitha C., Mr. Mahesh P., and Mr. Komal Kedarnath for their help and support. We are grateful to Dr. Parshati Patel, our external mentor, for guiding us in choosing the topic of research and Mr. Sundar M. N., our internal guide for helping us throughout the project in solving the problems we faced at different levels of our work. We whole-heartedly thank SSERD for giving us this opportunity to have a great learning experience with their constant support and interactions with students from all parts of the country even during this tough time.

ABSTRACT

In Celestial Mechanics, orbital resonances occur when orbiting bodies exert regular periodic gravitational influence on each other, usually because their orbital periods are related by a ratio of small integers. While most exoplanetary systems discovered are not found to have planets in mean motion resonances, we have tried to show the first order resonances' effects on two planets in orbital motion. Some simulations also indicated that the system of resonances may have formed via planetary migration (for example, the four-body orbital resonance in Kepler-223). We proposed that the orbital resonance is the reason for the stability of externally perturbed eccentric orbits by using a Hamiltonian approach. We reconsidered the general Keplerian Hamiltonian of the three-body problem to basic orbital parameters into action angle variables by using Jacobi-Hamilton theory, and thus, reducing the number of independent variables. Further, we plotted various graphs of the Hamiltonian v/s Eccentricity (one of the variable parameters) and checked for the stability of our proposed system using these graphs. In addition to this, we have checked the stability for various other configurations and came up with promising results.

Contents

Our Team.....	131
ACKNOWLEDGEMENT	133
ABSTRACT	134
1. Introduction	137
1.1 Motivation	137
1.2 Aims and Objectives	138
1.3 Proposed Solution.....	138
2. Background and Literature Overview.....	138
2.1 Derivation of Hamiltonian	138
2.2 Stability.....	143
2.2.1 Stability method one- Lagrangian.....	144
2.2.2 Stability method two- Different types of equilibrium.....	145
2.2.3 Final stability criteria	146
2.3 To simulate and find the probability of collision for a disturbed two-planet system with independent Keplerian orbits	146
2.4 Simulating and finding the probability of collision:	147
2.5 Evaluation Criteria.....	148
2.6 Related Work.....	148

3 Materials and Methods	149
4 Data and relevant graphs.....	150
4.1 Data	150
4.2 Graphs	151
4.3 Plotting the Graphs.....	152
5 Observations	153
6 Error Analysis	153
7 Results and Conclusions.....	154
7.1 Critique and Limitations	156
7.2 Future Scope	157
7.3 Summary	158
8 References	168

I. Introduction

The hidden mysteries of our Universe increase with the discoveries of inconceivable stellar objects. The Kuiper belt was one of such fascinating findings, which was the integral part of our solar system, sadly deluded by the past technologies. But, the discovery of a magnificent celestial body called exoplanet led to an increment in the space research field amongst the scientists all around the globe.

Exo (extrasolar) planets denote all the planets found beyond our solar system, orbiting a star or more in the universe. Until 1995, the existence of exoplanets was a pure speculation, but it was proved otherwise when a fastmoving gas giant, 51 Pegasi b was identified by NASA's Kepler Space telescope which led to the period of 'Planet hunting'. Though more than 4000 such planets have been discovered and confirmed, the science of its detection is still in its infancy.

These discoveries are done through:

- > radial velocity where the change in color of the star's light, because of the presence of an orbiting planet causes a wobble in space
- > by transit method, that is, dimming of the star's light measured due to transiting of a planet between the star and the observer,
- > direct imaging,
- > gravitational microlensing,
- > astrometry.

Still researches to explore every bit of the details about exoplanets are on and many

astonishing developments are being made.

The planets' names are derived from the star catalogs, telescopic sky surveys, and space telescopes. The planets are mainly classified by their masses as rocky planets, mainly composed of heavier elements, super-earths, planets between 1 to 10 earth masses, gas giants, exceeding 10 earth masses, hot Jupiter, gas giant orbiting close to the host star, and rogue planets, roaming freely around the space.

All the orbits of the planets in our solar system are aligned with the Sun to an accuracy of 7° difference and are almost circular (eccentricity nearly equal to zero). But it was not the same case with the found stellar systems. There were many proposed reasons to explain the misalignment and eccentricities of these orbits. To elucidate it in detail, we have considered orbital resonance as the main reason for the stability of the eccentric orbits.

I.I Motivation

There have been various observations showing the existence of misaligned and eccentric orbits in different stellar systems in the Universe. One idea that we came up with was that during the planet formations, the protoplanetary disk that is formed can be more than one in number (referred to as multi- protoplanetary disks). And due to this, there can be an inclination found between

each planet's stable orbit. Upon further analysis, some anomalies were concluded to the above idea, and so, we later changed our topic to a more specific one shifting from misaligned protoplanetary disks to misaligned planetary orbits, and later to stable eccentric planetary orbits.

Then, we looked into the internal and external perturbations and the reasons for stability of the final system. We concluded that there is a resonance factor which affects these stable planet orbits and all these orbits have a resonance ratio of small integer values like 1:2, 4:3 etc. We got this idea from Pluto which is in a 3:2 resonance orbit with Neptune. We have, thus, considered this one factor out of the various others (internal and external) to study its effects on the system.

I.2 Aims and Objectives

Our aim was to account for the eccentric orbits of the exoplanets due to external perturbations using orbital resonance as the reason for stability.

Our objective was to take a planetary system having resonant eccentric orbits and finding the conditions for the stable system by using the Hamiltonian method and simulations. We also had to simulate and find the probability of collision for a disturbed two-planet system with independent Keplerian orbits.

I.3 Proposed Solution

The solution proposed for the stable eccentricity problem was that, though there had been many internal and external factors which could have caused the stable eccentric planetary system, we focused on orbital resonance as a major reason. This affects the stability of the system. We proposed that the stability of the entire system is high because of the resonance between the exoplanet's orbit. In our solution, this had been verified by using the Hamiltonian equation and plotting the graphs. We proposed that by plotting the Hamiltonian for various values of eccentricities and ratios of semi-major axes, it can be checked that which Hamiltonian system is most stable. Then, we verified our theory by using values of known resonant stellar systems and comparing the results. Other than that, we also calculated the probability of collision for any system with nearly intersecting independent Keplerian orbit.

2. Background and Literature Overview

2.1 Derivation of Hamiltonian

The astronomical science had certainly taken, interestingly, a new course after the discovery of Plutinos in late 20th century. Since then, a vast number of astrophysicists have started concentrating on the methods to discover and explore exoplanets, which might help them to

understand the numerous possibilities that the vast universe holds within itself.

It has been constantly observed that the most stable systems are in mean motion resonances which generally give commensurable quantities as their resonance numbers. This natural occurrence cannot be left out as a mere coincidence. In fact, multiple conclusions in several papers have proposed the Mean Motion Resonance (MMR) of planets, as the factor elevating the stability of the planetary system. The reason of stability is 3:2 MMR between Neptune and Pluto [Mal95], considering the fact that they have mutual inclination of 17.2° . The other prominent examples in our solar system are resonance among Uranian satellites [TW90] [Pea89], Jovian satellites [Hin+10], and Saturnian satellites [MDN16]. The process of planets resulting into MMR appears to be a complex evolution over the scale of 10-500 million years to reach the present stable state in which the astronomers found them.

The three-body problem had been widely discussed and experimented over the years, but only couple of experts have worked in elaborating the unrestricted resonance dynamical systems [Riv+05] [CY07] [MBF08]. The methods used by the scientists are very accurate, indulging the modern computations and instrumental equipments to calculate the minute things in the best possible ways. We, as a team working in our own capacity have developed a method to check the stability of the

three-body planetary system in the first order mean motion resonance system. Here, we have presented a more comprehensible approach to calculate the Hamiltonian of a three-body and have checked for its lowest energy state for the various possible values of orbital elements. We used already developed theories to construct a geometrical and analytical model to visualize the variation of the semi-major axis and the eccentricities of the planets in their final stage of their stability. Albeit, from where the major proportion was fetched [BM13] had contributed a great deal in the resonant orbital motion theories. The same theory can be used to find the divergence of a stable system from their mean motion resonances disturbed by the external factors, as well as internal stresses. And this has been gradually proven by certain citations over all these years. The thermodynamical approach considering the evolution of a proto-planetary disk and internal changes are done by Paardekooper [PP09] and Bitsch [BK11]. Furthermore, the migration of planets can also be explained using similar models.

We took certain assumptions which saved us from the rigorous computations and helped simulating the actual dynamics of the planetary systems. The original theory has been used by numerous scientists to calculate the dynamics of the 3-body problem and simulate or compute the equations of motion with the help of advanced software. However, we used a household PC to plot our 3D graphs

and achieve stability conditions. The accuracy and precision of this method is quite good considering the type of model evolved. We have discussed that in detail in later sections.

We began with study of the orbital parameters governing the state of planetary motions in space. The list of orbital elements included a remarkably long range of parameters which were uniquely defined by Danby [JMA62]. Some of the parameters were significantly dropped from our model which we shall see in the derivation of Hamiltonian. Long-term radial velocity monitoring methods have revealed that giant planets occasionally reside in mean motion resonances at orbital distances exceeding 1 AU [Wri+11]. However, the resonances are common if the planets are orbiting very close to their host star [Fab+14]. In our model, we took the mass of inner planet equivalent to the mass of Jupiter, and outer to be twice the mass of Jupiter. This was done to include the most general case. In addition to this, we took the ratios of the semi-major axis instead of the semi-major axis itself. This one modification helped us to inculcate all the possible variation in distances between the two planets, which otherwise would have not been possible.

The exact Hamiltonian contained all the six necessary orbital parameters:

1. eccentricity (e),
2. semi-major axis (a),
3. inclination (i),
4. longitude of the ascending node (ω): It is

angle from a specified reference direction called origin of longitude to the direction of the ascending node, as measured in specified reference plane,

5. argument of periapsis (ω): Angle from body's ascending node to its periapsis, measured in direction of motion and

6. true anomaly (θ): parameter defining the position of the body moving along a keplarian orbit.

The basic heliocentric formula for H is given as [LR95] [Mor02]:

$$H = \left(\frac{M + m_1}{2M} \right) \cdot \frac{p_1^2}{2m_1} + \left(\frac{M + m_2}{2M} \right) \frac{p_2^2}{2m_1} - \frac{GMm_1}{r_1} - \frac{GMm_2}{r_2} + \frac{p_1 p_2}{M} - \frac{Gm_1 m_2}{\Delta_{12}} \quad (1)$$

where H is the required Hamiltonian, M is the mass of the host star; m_1 is the mass of the inner planet corresponding with r_1 distance from the star, and m_2 is mass of outer planet with r_2 distance. G is the universal gravitational constant. Δ_{12} is the distance between two planets; p being the momentum of the barycenter of the two bodies. We developed the theory in k , where k is the resonant number between planets. We now start introducing the equations in the form of orbital elements, and thus, H_{kep} takes the form referred in [Mor02]:

$$H_{kep} = -\frac{GMm_1}{ka_1} - \frac{GMm_2}{ka_2} \quad (2)$$

where a_1 and a_2 are semi-major axes of planets. The rest of the Hamiltonian is planet-planet interactions, and generally given as the

disturbing function. The disturbing function can be expressed as the Fourier series in orbital angles, and power series in inclination and eccentricities [LR95] [LB10]. Since we are assuming long term stability of the orbits, the terms in the Hamiltonian which vary over the orbital scales have been averaged out and dropped [Mur02] [MD00]. We have dealt with the first order resonant theory, so the dependence of inclination orbital parameter is left out. Therefore, resonant part of the Hamiltonian is given as:

$$H_{res} = -\frac{Gm_2m_1}{a_2}(f_{res}^{(1)}e_1 \cos(k\Lambda_2 - (k-1)\Lambda_1 - \bar{\omega}_1) + f_{res}^{(2)}e_2 \cos(k\Lambda_2 - (k-1)\Lambda_1 - \bar{\omega}_2)) \quad (3)$$

where $k:(k-1)$ is the resonant ratio exhibited by planets, $\bar{\omega}$ is the longitude of perihelion, e is the eccentricity of planet, and λ is the mean longitude. $f(1)$ and $f(2)$ are the parts of disturbance function which can be fetched either computationally or analytically [CY07] [LB10]. Solar System Dynamics 2000 have calculated these functions and tabulated with all the orders required. Although we started simplifying the Hamiltonian, the functional form of Keplerian orbital elements do not form a canonically conjugated set. Thus, we did canonical transformation and converted it to Poincare action-angle variables defined as:

$$\begin{aligned} \Lambda &= \mu\sqrt{G(M+m)a} \\ \Gamma &= \Lambda(1 - \sqrt{1 - e^2}) \simeq \frac{e^2\lambda}{2} \\ \gamma &= -\bar{\omega} \end{aligned} \quad (4)$$

where μ is the reduced mass,

$$\mu = \frac{mM}{M+m} \simeq m \quad (5)$$

after the transformation, the H_{kep} and H_{res} take following form:

$$H_{kep} = -\frac{G^2 M^2 m_1^3}{2\Lambda_1^2} - \frac{G^2 M^2 m_2^3}{2\Lambda_2^2} \quad (6)$$

$$\begin{aligned} H_{res} &= -G^2 M^2 m_1 m_2^3 (f_{res}^{(1)} \sqrt{\frac{2\Gamma_1}{\Lambda_1}} \cos(k\Lambda_2 - (k-1)\Lambda_1 + \gamma_1) \\ &+ f_{res}^{(2)} \sqrt{\frac{2\Gamma_2}{\Lambda_2}} \cos(k\Lambda_2 - (k-1)\Lambda_1 + \gamma_2)) \end{aligned} \quad (7)$$

Although we did not explicitly assume coplanar orbits, the linear expansion of the disturbing function contained no terms that had dependence on the longitudes of the ascending node and the orbital inclinations. Therefore, it was evident that the number of degrees of freedom of H had been reduced to four.

On further simplification and expansion of the Hamiltonian to second order, we got:

$$H_{kep} = n_1\Lambda_1 + n_2\Lambda_2 - \frac{3}{2}(n_1\Lambda_1^2 + n_2\Lambda_2^2) \quad (8)$$

where

$$n = \sqrt{\frac{GM}{a^3}} \quad (9)$$

and,

$$h = \frac{n}{\Lambda} = \frac{1}{ma^2} \quad (10)$$

The formulation can be simplified by introducing another canonical transformation.

The new variables are defined as:

$$\begin{aligned} K &= \Lambda_1 + \frac{k-1}{k}\Lambda_2 \\ \Theta &= \frac{\Lambda_2}{\kappa} \quad \theta = k\Lambda_2 - (k-1)\Lambda_1 \end{aligned} \quad (11)$$

Therefore, H_{res} and H_{kep} take the value:

$$H_{\text{kep}} = 4n_1K + 3h_1(k-1)K\Theta - \frac{3}{2}(h_1(k-1)^2 + h_2k^2)\Theta^2 - \frac{3}{2}h_1K^2 \quad (12)$$

$$H_{\text{res}} = -\alpha\sqrt{2\Gamma_1}\cos(\gamma_1 + \theta) - \beta\sqrt{2\Gamma_2}\cos(\gamma_2 + \theta) \quad (13)$$

where α and β takes the value:

$$\begin{aligned} \alpha &= \frac{G^2 M m_1 m_2^3}{\Lambda_2^2} \frac{f_{\text{res}}^{(1)}}{\sqrt{\Lambda_1}} \\ \beta &= \frac{G^2 M m_1 m_2^3}{\Lambda_2^2} \frac{f_{\text{res}}^{(2)}}{\sqrt{\Lambda_2}} \end{aligned}$$

We get the generating function of second kind F , and from where, we get k as the constant of motion.

$$F = \Lambda_1 K + (k\lambda_2 - (k-1)\lambda_1)\Theta$$

We further transform the equations into the mixed cartesian coordinates to Hamiltonian.

$$\begin{aligned} x_1 &= \sqrt{2\Gamma_1}\cos\gamma_1 & y_1 &= \sqrt{2\Gamma_1}\sin\gamma_1 \\ x_2 &= \sqrt{2\Gamma_2}\cos\gamma_2 & y_2 &= \sqrt{2\Gamma_2}\sin\gamma_2 \end{aligned}$$

where x is the conjugate momentum and y is

coordinate. After rigorous mathematics, H_{res} reads,

$$H_{\text{res}} = (-\alpha x_1 + \beta x_2)\cos\theta + (\alpha y_1 + \beta y_2)\sin\theta$$

We then introduce the rotation formulated by Henrard [Hen+86] and Wisdom [Wis86] to our Hamiltonian and defining it into polar coordinates (Φ, φ) .

$$\begin{aligned} u_1 &= \frac{\alpha x_1 + \beta x_2}{\sqrt{\alpha^2 + \beta^2}} & v_1 &= \frac{\alpha y_1 + \beta y_2}{\sqrt{\alpha^2 + \beta^2}} \\ u_2 &= \frac{\beta x_1 - \alpha x_2}{\sqrt{\alpha^2 + \beta^2}} & v_2 &= \frac{\beta y_1 - \alpha y_2}{\sqrt{\alpha^2 + \beta^2}} \\ u &= \sqrt{2\Phi}\cos\phi & v &= \sqrt{2\Phi}\sin\phi \end{aligned}$$

Now, the H_{res} is given by:

$$H_{\text{res}} = -\sqrt{\alpha^2 + \beta^2}\sqrt{2\Phi}\cos(\phi_1 + \theta)$$

After performing multiple transformations, we successfully reduced the number of freedoms to two. Further solving the Hamiltonian, we could find the constant terms, and drop them from the final equation. Till now, the H is formulated in the parameters. H is parameterized by h , n , α and β , so, we combined all the terms and came up with another constant δ^* , which we defined later. To simplify our Hamiltonian, we also divided it with a constant factor η without losing the generality of the Hamiltonian. So, the transformation goes like:

$$K' = \frac{K}{\eta}$$

$$\Theta' = \frac{\Theta}{\eta}$$

$$\phi'_1 = \frac{\phi_1}{\eta}$$

$$\phi'_2 = \frac{\phi_2}{\eta}$$

Where

$$\eta = \left[\frac{4\alpha^2 + \beta^2}{9(h_1(k-1)^2 + h_2k^2)^2} \right]^{\frac{1}{3}}$$

The Hamiltonian became:

$$H = \hat{\delta}\Theta' - \Theta'^2 - \sqrt{2\phi_1} \cos(\phi_1 + \Theta_1)$$

Where

$$\hat{\delta} = \frac{2h_1(k-1)K'}{h_1(k-1)^2 + h_2k^2}$$

The final canonical transformation yielded us the generating function F of second kind in which ω is a constant of motion.

$$F' = \Theta\Omega + (\phi_1 + \theta)\Psi_1 + (\phi_2 + \theta)\Psi_2$$

$$\Psi_1 = \phi'_1 \quad \Psi_1 = \phi_1 + \theta$$

$$\Psi_2 = \phi'_2 \quad \psi_1 = \phi_2 + \theta$$

$$\Omega = \Theta' - \Psi_1 - \Psi_2 \quad \omega = \theta$$

We now got the final Hamiltonian in one degree of freedom:

$$H = \hat{\delta}(\Omega + \Psi_1 + \Psi_2) - (\Omega + \Psi_1 + \Psi_2)^2 - \sqrt{2\Psi_1} \cos \psi_1 \quad (14)$$

1.1.1 Disturbance Function

For the first order argument the direct part is given by, the cosine argument:

$$j\lambda_2 - (1-j)\lambda_1 - \bar{\omega}_1$$

The term corresponding to the argument is defined as:

$$R_s = e_1 f_{27} + e_1^3 f_{28} + e_1 e_2^2 f_{29} + e(s^2 + s^{12}) f_{30}$$

The functions are given by:

$$\begin{aligned} f_{27} &= \frac{1}{2}[-2j - \xi D] A_j \\ f_{28} &= \frac{1}{16}[2j - 10j^2 + 8j^3 + 3\xi D - 7j\xi D + 4j^2\xi D - 2\xi^2 D^2 - 2j\xi j^2 D^2 - \xi^3 D^3] A_j \\ f_{29} &= \frac{1}{8}[8j^3 - 2\xi D - 4j\xi D + 4j^2\xi D - 4\xi^2 D^2 - 2j\xi^2 D^2 - \xi^3 D^3] A_5 \\ f_{30} &= \frac{1}{4}[\xi + 2j\xi + \xi^2 D][B_{j-1} + B_{j+1}] \end{aligned}$$

where ξ is the ratio of two semi major axes

$$d = d/d\xi$$

$$A_J = b_{\frac{1}{2}}^i(\xi)$$

$$B_J = b_{\frac{3}{2}}^j(\xi)$$

$$b_s^j(\xi) = \frac{2(s)(S+1)---(S+j-1)(\xi^3)}{1.2.3.4---} X [1 + \frac{S(S+j)\xi_2}{1+j} + \frac{S(S+1)(S+j+1)\xi^4}{1.2(j+1)(j+2)} + ---] \quad (15)$$

2.2 Stability

We looked into various approaches to find the stability of a Hamiltonian, before coming to a conclusion. As seen in the previous section, our Hamiltonian function consisted of orbital elements. Also, as mentioned in the proposed solution, most of the parameters of the Hamiltonian were kept constant. By varying the eccentricities and the ratio of the

semi-major axes, we got different values of Hamiltonian for different systems. So, to check which system will be the most stable, we needed a way to determine the stability of the Hamiltonian. Below are the various methods that we looked into.

2.2.1 Stability method one- Lagrangian

This method used a Lagrangian to find the equation of motion and then putting the potential experienced by the system to further find points of stability [GOL02]. Here, we considered a generalized approach which could be used if found suitable for our system, taking into account all the parameters required to define our model: eccentricities, masses, semi-major axis, etc. Let the Lagrangian be L . In spherical polar coordinates, the Lagrangian becomes:

$$L = T - V = \frac{1}{2}m(\dot{r}^2 + r^2\dot{\theta}^2) - V(r)$$

The generalized co-ordinates are[Gup11]:

$$p_\theta = \frac{\partial L}{\partial \dot{\theta}} = mr^2\dot{\theta} \quad (16)$$

$$\dot{p}_\theta = \frac{d}{dt}(mr^2\dot{\theta}) = 0 \quad (17)$$

Integrating (2),

$$mr^2\dot{\theta} = \text{const} \quad (18)$$

$$mr^2\dot{\theta} = l \quad (19)$$

(2) can be written as

$$\frac{d}{dt}\left(\frac{1}{2}mr^2\dot{\theta}\right) = 0.$$

Factor of $\frac{1}{2}$ is added because $\frac{1}{2}mr^2$ is expression for areal velocity

$$dA = \frac{1}{2}r(rd\theta)$$

$$\frac{dA}{dt} = \frac{1}{2}r^2\frac{d\theta}{dt}$$

Thus, the Lagrangian gives us the equation,

$$\frac{d}{dr}(m\dot{r}) - mr\dot{\theta}^2 + \frac{\partial V}{\partial r} = 0$$

$$\text{Let } -\frac{\partial V}{\partial r} = f(r)$$

$$m\ddot{r} - mr\dot{\theta}^2 = f(r)$$

Putting (4),

$$m\ddot{r} - \frac{l^2}{m * r^3} = f(r)$$

Further solving this equation gives the value of r :

$$\dot{r} = \sqrt{2/m(E - V - l^2/(2mr^2))}$$

This equation, on solving further, led us to an expression of eccentricity. Next, we needed an expression for energy. Thus, equation of energy is:

$$E = \frac{1}{2}m(\dot{r}^2 + r^2\dot{\theta}^2) + V(r) \quad (20)$$

For $r = 0$ (circular orbits),

$$E = V + \frac{l^2}{2mr^2}$$

Taking $V = -\frac{k}{r}$

$$E = -\frac{k}{r} + \frac{l^2}{2mr^2}$$

$$\frac{dE}{dr} = \frac{k}{r^2} - \frac{l^2}{2mr^3}$$

Putting this equal to 0,

$$\begin{aligned} rk &= \frac{l^2}{m} \\ r &= \frac{l^2}{mk} \end{aligned} \quad (21)$$

This is minima or maxima.

$$\frac{d^2E}{dr^2} = -\frac{2k}{r^3} + \frac{3l^2}{mr^4} = -\frac{2k^4m^3}{l^6} + \frac{3k^4m^3}{l^6} = \frac{k^4m^3}{l^6} \quad (22)$$

which is positive, and hence, a minima or a point of stability.

2.2.2 Stability method two- Different types of equilibrium

In this approach, we looked into the different types of stability: [How13]

1. Lyapunov stable

If there existed an equilibrium at $z_0 = (q_0, p_0)$ belonging to \mathbb{R}^{2n} of an autonomous hamiltonian flow, the equilibrium is called Lyapunov Stable if all nearby orbits remain close to z_0 for all forward time[How13].

It is also known as non-linearly stable. In mathematical terms, an equilibrium z_0 belonging to \mathbb{R}^{2n} is Lyapunov stable if for all neighbourhood V of z_0 , there exists a neighbourhood $U \subseteq V$ such that $z_0 \in U$.

This implies $z(t) \in V$ for all forward time.

2. Linearly Stable

An equilibrium is linearly stable if all orbits of tangent flow are bounded for all forward time.

A vector field in an autonomous hamiltonian flow:

$$\dot{z} = J\nabla H \quad (23)$$

where J = poisson matrix with I_n

J is non-singular. z_0 is an equilibrium of (2.1) iff $\nabla H(z_0) = 0$.

To study the stability of z_0 ,

$$\delta z = z - z_0 \quad (24)$$

where δz is infinitesimal.

$$\dot{\delta z} = L\delta z \quad (25)$$

where $L = JD^2H(z_0)$.

Since D^2H is symmetric, L is a Hamiltonian matrix. Hence, $LTJ + JL = 0$

Assuming distinct eigen values, the solution of (2.3) is known as 'tangent flow', and is of the form:

$$\delta z(t) = \sum_{j=1}^{2n} c_j \vec{v}_j e^{\sigma_j t} \quad (26)$$

where σ_j and \vec{v}_j are the eigen values and eigen vectors of L respectively. Eigen values are the roots of the characteristic polynomial:

$$P(\sigma) = \det(L - \sigma I) \quad (27)$$

Hence, the problem of linear stability reduces

to finding the eigen values and eigen vectors of the Hamiltonian matrix L.

3. Spectrally stable

An equilibrium is spectrally stable if all the eigen values of the tangent flow/linearisation are purely imaginary.

Non-linear stability \Rightarrow Linear stability \Rightarrow
Spectral stability

2.2.3 Final stability criteria

The above stability methods needed the Hamiltonian in (q,p) form whereas the simplified Hamiltonian that we had found had orbital elements as parameters.

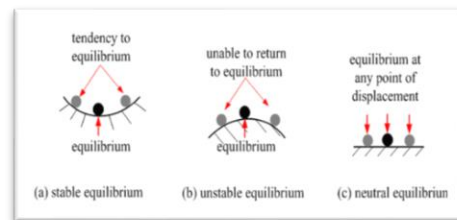
Moreover, the above methods that we researched gave us the stability of different points in a single system whereas we didn't need the most stable point in a system.

In the Hamiltonian, as we varied the eccentricity, we were changing the whole system itself. Hence, we discarded the above two methods and decided that for whichever eccentricities and semi-major axes, the Hamiltonian would have the lowest value, that would be the most stable Hamiltonian as it is time-independent. Thus, Hamiltonian represents the total energy.

The Hamiltonian is an energy function. We took the energy analogy, that the lowest point

is in stable equilibrium as seen in the figure below.

Figure 1: Equilibrium-Energy Analogy



2.3 To simulate and find the probability of collision for a disturbed two-planet system with independent Keplerian orbits

Collision probability for non-intersecting orbits [iop17]:

The collision probability per unit time is given by:

$$P = \frac{\pi \tau U}{(2|v_1 \times v_2|T_1 T_2)} \quad (28)$$

where

P = collision probability per unit time

τ = Collision radius

U = relative velocities of planet in the direction of motion

T1, T2 = Orbital period of planets

v_1, v_2 = velocity of planets

Collision radius and Gravitational focusing factor:

We consider two spherical objects have collided if the distance between them is less than or equal to the sum of their radii. This is true for normal objects. But for massive planets, gravity comes into picture. So, the effective radius of planets increases, and hence, the definition of collision radius changes because of multiplying this factor. This factor is called the gravitational focusing factor.

It is given by:

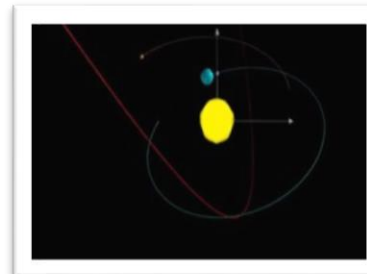
$$1 + \left(\frac{v_{esc}}{v_{enc}}\right)^2 \quad (29)$$

where v_{esc} is escape velocity of the more massive planet, and v_{enc} is the encounter velocity of the planet.

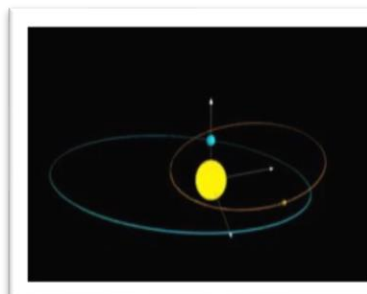
2.4 Simulating and finding the probability of collision:

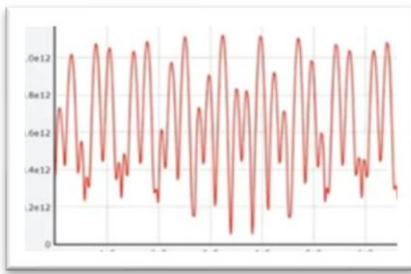
We have used vpython module in Python to simulate the process. We have also graphed the interplanetary distance. In our simulation, we have not taken the gravitational focusing factor into consideration since it doesn't make a big difference for low mass objects. Using this collision probability, we were able determine the stability of the planetary orbits. Since, the probability depends on the encounter velocity (relative velocity of

planets during the closest approach), the code is made to update the probability every time the distance of the closest approach is lower than the previous one. Multiple simulations have been performed using reasonable values for mass of planets, stars, and asteroids. Although, due to some computational limits, we couldn't increase the frame rate of the simulation, to speed up the process, we increased the velocity of the planets, and to make the planet clearly visible, the radius is increased.



After running the simulations, we calculated the probability of collision





- (a) Before disturbance
- (b) Foreign body approaches the Stable Sysytem
- (c) A new system with a different Orientation
- (d) Distance between the planets V/S Time

Graph

The probability being very low, the system will remain stable for a long time provided no other external factors affect the system.

2.5 Evaluation Criteria

We have evaluated our theory by verifying our model and code with known resonant systems. If our eccentricity and semi-major axis values were close enough to the known values, then, our theoretical model must have been correct. There was space for error in the values due to approximation on our part, and the error bars already there in the known values.

2.6 Related Work

To verify our findings, we looked for similar models to our system. But to our surprise, every study on this topic was done considering the desirable parameters. Like,

for our study, we chose to work with eccentricities and semi-major axis, thus, we started with the research papers defining Hamiltonian of systems in resonances.

In one paper titled "Revealing the evolution the stability and escapes of families of resonant periodic orbits in Hamiltonian systems" [EE13], the study was based on the evolution of different resonance families as a function of their energy. This study mentioned about stable and unstable periodic orbits citing that the stable periodic orbits which avoid going through the center are called "centrophobic", and unstable periodic orbits starting from the origin are known as "centrophilic". Also, their graphs suggested that stable periodic orbits corresponded to elliptic points and unstable periodic orbits corresponded to saddle points in the phase plane.

In another paper titled "Planets Near Mean-Motion Resonances" [CT13], they have used the modified Delaunay variables for canonical elements $\lambda = +\omega$, $\Gamma = \omega$, $\Lambda = (\mu a)^{1/2}$, $\tau = (\mu a)^{1/2}[1 - (1 - e^2)^{1/2}]$, where $\mu = Gm$ is the gravitational mass of the star

According to their study, transit observations of exoplanets measure the time interval P between successive transits, that is, the interval in which the longitude increases by 2π . Hence, the distribution of transit-based period ratios near resonances was determined mainly by the distribution of the osculating

mean motions instead by any differences between the osculating and transit-based mean motions.

In their three-body problem explanation, they have also discussed results for variable eccentricities. Non-zero eccentricity of the perturber is expected to introduce chaotic zones in the vicinity of the resonances, such that initially circular orbits are excited to higher eccentricity over a wider range of period ratios compared with the case of a zero-eccentricity perturber. Non-zero eccentricities could also lead to slow evolution of the period-ratio distribution on timescales much longer than the 10^4 planet orbits.

Further, they did comparisons of their models with Kepler systems. This model and observed period-ratio distributions near these resonances are consistent for mean planet masses in the range $20\text{--}100 M_\oplus$.

So, we realized that we were not able to find exactly the same Hamiltonian, that is, with the same parameters as generalized co-ordinates as the one we considered in our study.

And many such studies have been done in this field but with different models based on parameters like:

1. Spin-orbit couplings
2. Period ratio distribution
3. Inclination

4. Long period-short period
5. Depending upon mass
6. 1st and 2nd ordered resonances, etc.

3 Materials and Methods

The stability of an exoplanetary system depends upon many variable parameters, among which some are dependent or independent of each other. Amid the many factors which were surveyed as external perturbations for a stellar system to be misaligned, we have examined Orbital Resonance as the main reason for stabilization of these systems.

We have considered a three-body system, two planets orbiting a host star, such that the ratio of the orbital parameters gives a simple integer. Those systems whose periods of revolution are a simple integer of each other are said to be in mean motion orbital resonance (MMR). To further simplify the complexity, we have taken the systems which were in first order orbital resonance. We have analyzed and collected all the parameters or the initial conditions affecting the stability of the resonance, which included, host star mass, eccentricity of the orbits, semi-major axis, argument of the periaxis (ω), inclination angle(i), mass of the planets, and mean motion resonance (MMR) from various sources

We have used Hamiltonian to explain the equation of motion of the considered stellar system. Since there were many parameters that defined the system, the number of independent variables had to be reduced, that is, we reduced the degrees of freedom to four by Canonical transformation of Keplerian orbital parameters to Poincare Action angle variables. After many canonical transformations, Hamiltonian is regarded in polar coordinates. We later arrived to the final equation simplified to Hamiltonian in one degree of freedom as explained in detail above .

To check the stability of the above formulated Hamiltonian function, certain methods were put forward. Different types of equilibrium were investigated to check if it was suitable for the proposed method.

Stability analysis through equation of motion of Lagrangian was compared to check its compatibility to the proposed function. We decided to proceed with the energy analog, where the lowest point should be in stable equilibrium.

To calculate the stable energy of our system, the mathematical model was coded in Python 3.8 Anaconda Jupyter version and a 3D graph was plotted between the eccentricities of the two planets and the host star to visualize the variations. The graphs have been explained later in the paper. Thus, we had obtained the eccentricities of the two

planets corresponding to the lowest energy stable state.

This was compared to the data collected from various existing planetary models to caliber the proposed model. The data collection was a challenging task as there were less systems found till date.

4 Data and relevant graphs

4.I Data

The following are the various graphs that we have drawn from the data:

	Planetary system	Host mass	e (eccentricity)	a(AU) (semi-major axis)	w(degrees)	λ (deg)	Planet mass	MMR (Mean Motion Ratio)
Star	GJ436	0.41Ms						
Planet1	GJ436b		0.16	0.02872	351	72	21.36Me	2:1
Planet2	GJ436c		0.3	7.9	36.5	139	0.23Mj	
Star	PSRB1257+12	1.4Ms						
Planet1	PSRb		0.0186	0.36	108.3	-	4.3 Me	2:3
Planet2	PSR d		0.46	0.46	250.4	-	3.9Me	
Star	GJ876	0.334Ms						
Planet1	GJ876b		0.0328	0.21	248.7	341.13	0.7142Mj	2:1
Planet2	GJ876c		0.255	0.129	252.08	71.09		
Star	HD82943	1.14Ms						
Planet1	HD82943c		0.359	0.746	124	343	1.439Mj	1:2
Planet2	HD82943b		0.219	1.19	237	83	14.5Mj	
Star	MU ARA	1.10Ms						
Planet1	MU ARAd		0.066	0.921	213	235.13	0.0396Mj	2:1
Planet2	MU ARAb		0.128	1.527	22	36.59	1.74Mj	

Table 1: Data of various planetary systems
[\[Byr13\]](#) [\[NAS\]](#) [\[SK06\]](#) [\[Tin+06\]](#) [\[PH05\]](#) [\[Sch10\]](#) [\[Rod+18\]](#)

where,

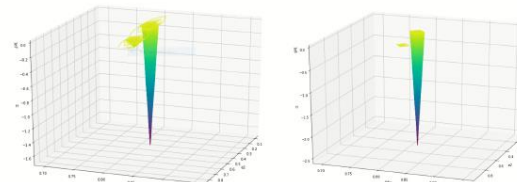
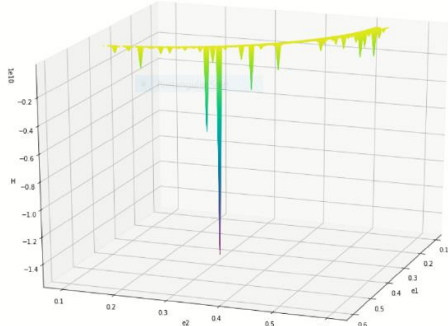
M_s = Mass of the Sun M_j = Mass of Jupiter

M_e = Mass of Earth

For our project, we have only taken the data from the stellar system of HD82943. The graphs in the next section correspond to this system.

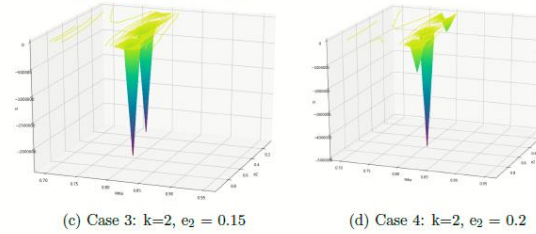
4.2 Graphs

The following graph is of the system HD82493 to check the eccentricity error. While, the rest of the graphs are obtained for the various cases considered.



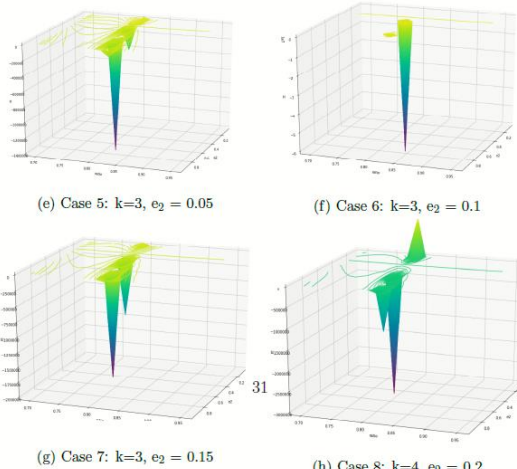
(a) Case 1: $k=2, e_2 = 0.05$

(b) Case 2: $k=2, e_2 = 0.1$



(c) Case 3: $k=2, e_2 = 0.15$

(d) Case 4: $k=2, e_2 = 0.2$



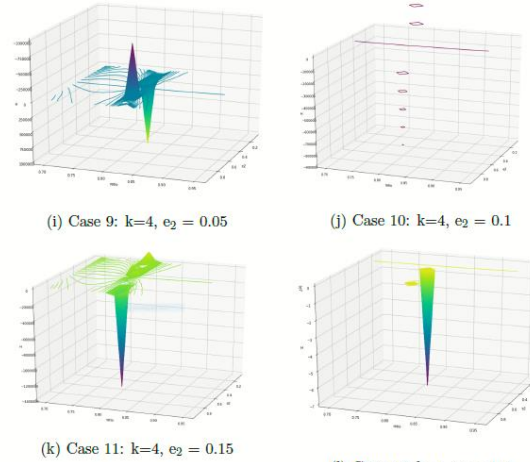
(e) Case 5: $k=3, e_2 = 0.05$

(f) Case 6: $k=3, e_2 = 0.1$

(g) Case 7: $k=3, e_2 = 0.15$

(h) Case 8: $k=4, e_2 = 0.2$

Figure 4: H, e_1, e_2



(i) Case 9: $k=4, e_2 = 0.05$

(j) Case 10: $k=4, e_2 = 0.1$

(k) Case 11: $k=4, e_2 = 0.15$

(l) Case 12: $k=4, e_2 = 0.2$

Figure 5: All the cases for H, r, e_2

4.3 Plotting the Graphs

We have coded and obtained the various graphs in 3D using matplotlib. Python 3.8 was used to render all the graphs aided by Jupyter notebook, Anaconda. The following were the steps used to analyse the Hamiltonian from our graphs.

Checking for the error in eccentricities by taking different values of e1 and e2:

- We started with a constant value of e1, that is, 0.01 and ran the program with different values of e2, i.e., 0.001 to 0.599. This gave us 60 H values with the step size of 0.01.
- We then changed the value of e1 by 0.01 and repeated the same process. This fetched 60 H values with the step size of 0.01.
- By continually changing e1 with same interval, we got all the 3600 values of H.
- The obtained data was tabulated in the form of e1, e2, and H.
- It was plotted on a 3D graph with y-axis as H, x-axis as e1, and z-axis as e2.
- This gave us the standard error analysis of eccentricities to get an insight on how viable our model is.

To obtain the stability points in the resonance orbits by taking different values of e2 and the ratio of semi-major axis α :

- We took e1 to be a constant, e.g., 0.049 with a specific value of ξ (a_1/a_2), e.g., 0.01. We ran the program with different values of e2, e.g., 0.001 to 0.799. This gave us 80 H values with the step size of 0.01.
- Then, we changed the value of ξ with the step size of 0.01. Repeating the steps again, fetched another 90 H values with the step size of 0.01.
- Continually changing ξ with same interval gave us all the 8100 values of H.
- The obtained data was tabulated in the form of e2, ξ , and H.
- A 3D graph with y-axis as H, x-axis as e2, and z-axis as ξ was plotted.
- This gave the stable points of system with the stability corresponding to the lowest value of the Hamiltonian.
- This gave one 3D graph for one value of e1. We computed it for two or three more sets of e1.
- The computations correspond to first order resonance with the k value of 2, that is, 2:1 resonance.
- For k=3 and 4, we repeated all the steps to obtain 4 graphs corresponding to each value of k to check for higher order resonances

5 Observations

On carefully scrutinizing the graphs, we observed the following points.

1. The graphs between e_1 , e_2 , and H were analysed first. As mentioned previously, we used that method to calculate the percentage error in e_2 which came out to be 13.091%. This error was within the permissible limits considering the accuracy of our model. We have used the variation of α from 0.7 to 0.95 with the step size of 0.05. The range was significantly reduced in order to reduce the H values.
2. The other graphs corresponded to the various k values or the other cases of first order mean motion resonances. We calculated the log error from the derived equation of log error of our Hamiltonian. The various log errors for each graph are given in the table below.
3. We took all the other orbital parameters as constant except for the values of e_1 , e_2 , and α . On one of the axis, we plotted the energy values; corresponding to the ξ and eccentricity of second planet.

4. This configuration gave us the parameters for which the system was most stable as the lowest peak relates to the minimum energy as discussed in detail in earlier sections.
5. The error in the higher k values increased as we figured it out from the log error analysis.

6 Error Analysis

We found the error in H (Hamiltonian) by propagation of log errors in e_1 and e_2 . The individual errors of various parameters used in the Hamiltonian are given below. The final error in Hamiltonian is given by the Equation 41.

$$H = \hat{\delta}\left(\frac{\Theta}{\eta}\right) - \left(\frac{\Theta}{\eta}\right)^2 - \frac{1}{\sqrt{\eta}}(u_1 \cos\theta - v_1 \sin\theta) \quad (30)$$

This can be written as,

$$H = H_1 + H_2 + H_3 \quad (31)$$

$$H_1 = \hat{\delta}\left(\frac{\Theta}{\eta}\right) \quad (32)$$

$$H_2 = -\left(\frac{\Theta}{\eta}\right)^2 \quad (33)$$

$$H_3 = -\frac{1}{\sqrt{\eta}}(u_1 \cos\theta - v_1 \sin\theta) \quad (34)$$

The error propagation in Hamiltonian is given as:

$$\frac{\Delta H}{H} = [(\frac{\Delta H_1}{H_1})^2 + (\frac{\Delta H_2}{H_2})^2 + (\frac{\Delta H_3}{H_3})^2]^{\frac{1}{2}} \quad (35)$$

The individual error of the terms are given as:

$$\frac{\Delta H_1}{H_1} = \frac{\Delta H_2}{H_2} = -2\frac{\Delta \eta}{\eta} \quad (36)$$

$$(\frac{\Delta \eta}{\eta}) = (\frac{\sqrt{8}}{3}) \frac{\Delta \alpha}{\alpha} \quad (37)$$

$$\frac{\Delta \Gamma_1}{\Gamma_1} = 2\frac{\Delta e_1}{e_1}, \quad \frac{\Delta \Gamma_2}{\Gamma_2} = 2\frac{\Delta e_2}{e_2} \quad (38)$$

$$\frac{\Delta \alpha}{\alpha} = \frac{\Delta \beta}{\beta} = \frac{\Delta R}{R} = 4(\frac{\Delta e_2}{e_2}) + [(\frac{2\Delta e_1}{e_1})^2 + (\frac{\Delta e_2}{e_2})]^{\frac{1}{2}} \quad (39)$$

$$\begin{aligned} \frac{\Delta u_1}{u_1} = \frac{\Delta v_1}{v_1} = 2(\frac{\Delta \alpha}{\alpha})^2 + \frac{1}{2}(\frac{\Delta \Gamma_1}{\Gamma_1})^2 + \frac{1}{2}(\frac{\Delta \Gamma_2}{\Gamma_2})^2 + (\frac{\Delta \beta}{\beta})^2 \\ + \frac{1}{2}\sqrt{(\frac{2\Delta \alpha}{\alpha})^2 + (\frac{2\Delta \beta}{\beta})^2} \end{aligned} \quad (40)$$

$$\frac{\Delta H_3}{H_3} = [(-\frac{2}{3}\frac{\Delta \alpha}{\alpha})^2 + \sqrt{2}(\frac{\Delta u_1}{u_1})]^{\frac{1}{2}} \quad (41)$$

This gives us the error in Hamiltonian

$$\begin{aligned} \frac{\Delta H}{H} = [8(\frac{8}{9}\frac{\Delta \alpha}{\alpha})^2 + (-\frac{2}{3}\frac{\Delta \alpha}{\alpha})^2 + \sqrt{2}(2\frac{\Delta \alpha}{\alpha})^2 + \frac{1}{2}(2\frac{\Delta e_1}{e_1})^2 \\ + \frac{1}{2}(\frac{\Delta e_2}{e_2})^2 + (\frac{\Delta \alpha}{\alpha})^2 + 4(\frac{\Delta \alpha}{\alpha})]^{\frac{1}{2}} \end{aligned} \quad (42)$$

Case Number	k	e ₁	H	ΔH
1	2	0.05	-17797715.99	-8344780
2	2	0.1	-11544.80496	-5276.67
3	2	0.15	-297269.764	-244771
4	2	0.2	-2586808.24	-1254209
5	3	0.05	-13438625.3	-6300942
6	3	0.1	-1356581.518	-671553
7	3	0.15	-257095.944	-211050
8	3	0.2	-1529980.828	-741808
9	4	0.05	-9414593.16	-4414202
10	4	0.1	-212515.571	-464498
11	4	0.15	-220074.187	-480195
12	4	0.2	-1356581.518	-657736

Table 2: Error in H

This error analysis is for the (H, r, e2) graphs. Here we have taken the star to be a sun like star and the planets to have Jupiter like mass. The graphs are drawn to see what such a system would be like for varying eccentricities and ratio of the semi-major axes of the two exo-planets.

7 Results and Conclusions

- It was evident from the 1st graph between e1, e2, and H, what we were trying to plot. We found the minimum Hamiltonian by adjusting the range of z-axis (H), and we got energy dips, as expected. Plotting a large picture of H values would hide the energy dips in the plot, so a limited range was chosen to show only the required levels. We found our mathematical model to be quite satisfactory for certain eccentricities as it showed a 13.09%

error. So, for the HD 82493 system, our model gave acceptable results.

However, the accuracy can be increased to 10–4. Normally, it would take 15 minutes to execute a single program computing around 10,000 values of Hamiltonian. The idea of working with 3,00,000 values of Hamiltonian was, therefore, dropped. We can have covered a larger range of α values with a better technological hand.

2. The log error in the Hamiltonian was calculated with the error propagation analysis. Although the model gives low value of ΔH for the maximum values of obtained lowest Hamiltonians, there is a particular set of Hamiltonians corresponding to eccentricity 0.15, which show very large errors. All the mathematics was rechecked, but it showed no sign of possible errors. However, it is felt that the Laplace coefficients including the disturbance function can account for this error.
3. The graphs clearly showed us the minimum stability for all the values of k and e . The combination of corresponding eccentricities and the ξ

value can give us the information about the resonant conditions of the system. By analysing multiple systems with various parameters, we can come up with resonance equations for each system. But, we need highly accurate and precise values to consider this method.

4. In the similar fashion, we can observe stability of any planetary system by calculating the Hamiltonians at any values of eccentricities and semi-major axis. The data for various exoplanets are given in Table 1. This can be used to scrutinize the orbital structures and check the viability of this model.
5. This technique could also be used to find any unknown orbital parameters, provided we know all the other orbital parameters. But, the stability would still be a subjective choice here, adding more complexities to the equations.
6. The stability of the Hamiltonian could be calculated by various methods mentioned in earlier sections, but another mathematical model may be required to calculate that analytically.

So, our model gives acceptable results for the HD 82493 system. But as seen from the error analysis of the rest of the graphs the model shows increasing error as the k value increases. We will need to verify our model with more data to give a more proper conclusion.

7.1 Critique and Limitations

The mass of the inner planet was considered to be equal to the mass of Jupiter and the outer planet, twice the mass of Jupiter for a general case. This was considered due to the fact that many of the exoplanets found over the 1 AU distances are gas giants. This was solely done to simplify the mathematics and to adapt to the computational capabilities.

The ratio of semi-major axes of the two planets were taken instead of semi-major axis itself to account distances over large ranges. This was an additive advantage rather than the limitation. Oblateness factor was the one factor which could have caused significant change in the resonance strengths but to save ourselves from the tedious equations, it was assumed to be zero. Several research analyses have already covered in detail, but oblateness factor deals with the internal stresses, instead of the external factors. Since the project was focused on

external factors, the idea of dropping oblateness factor was a relevant approach.

To further narrow down the complexity, first order resonances were only scrutinized excluding higher order resonances. While considering the first order resonant theory, the dependence of inclination orbital parameter was automatically left out as there was no term involving inclinations between the planets.

For finding similar models to the one proposed above, many papers varied from each other in the parameters making it arduous to collate. Our computational proficiency was meager for the complex task we put forward. As the values of our function were not normalized, the range of the axis came out to be very large. The programming allowed us to consider limited step size for a particular range and recognized only certain bounded ranges, thus, making it more difficult and time consuming to plot for each function. Moreover, the data available from different sources for our requirements were very sparse.

7.2 Future Scope

There are a number of factors which we could have worked upon to get better and more accurate results:

1. There are different methods to find the errors in the above implemented model. Plotting the error bars would have been key factor in analysing the obtained values of Hamiltonian. Extrapolating the data could be done if the computational obstacles are manageable. We can also calculate the variance, find residuals using Statistical Chi square value method, or finding the percentage error. However, the function is non-linear and the complexity increases multi-fold. Another method which support non-linear functions, called Regression Analysis, can be used by which we can analyze how much error is present in dependent variables (such as eccentricities, semi-major axis) which contribute to the overall error of the function.
2. Collecting more number of data to check the compatibility of our Hamiltonian function can lead to more accuracy in error evaluation.
3. As the limitations of our project lead to the future aspect, the computational tactics can be further improved for reducing the marginal errors by managing the step size and bounded range to get more accurate data from the limited sources available.
4. We have considered many initial parameters as constant to simplify the mathematical equations to achieve equation in one degree of freedom. Further steps can be taken to consider less constants and more variables to include in the final equation, thus, increasing its credibility.
5. We have taken the final stage of a stable system and considered the resonance to be the main factor of its stability. There are other factors such as planetary migration, spin orbit coupling, etc. which can be studied to understand its contribution to a stable system. The options are boundless.
6. The external perturbations, like shock waves, tidal waves, and internal stresses which lead to a resonance in the periodic orbits in the stable systems could be studied

simultaneously to improve this theory.

7. Computational programming along with simulations can be adapted to visually portray the mathematical function of a planetary system for a better understanding.
8. Order of resonances for systems higher than one can be studied and introspected.

7.3 Summary

The aim was to count for the stability of the resonant orbits of a planetary system after it was externally perturbed. The parameters which contributed to the state of the stellar structures were studied.

The equation of motion of the planetary system was reduced to a three body problem and a relation was found between most of

the initial parameters to account for its stability. The planetary system was noted to be in first order orbital resonance.

The mathematical model was written in Hamiltonian to reduce the complexity. The Hamiltonian included two parts: Keplerian equations and the external disturbing functions. The degrees of freedom of the Hamiltonian function was reduced to one from six by multiple canonical transformation of Keplerian orbital parameters to Poincare action angle variables, then later to polar coordinates.

The constants and less important terms are excluded from the Hamiltonian. The Hamiltonian was found for the lowest possible energy for various orbital variables. The stable eccentricities were found for each systems corresponding to its stable Hamiltonian through lowest point energy analog. These are compared to the existing planets and the error percentage is calculated.

A Code for the (H, e_1, e_2) graph

The following code is for the graph of (H, e_1, e_2) graph:

```

import math
import sympy as sp
import numpy as np

#Initial Parameters
k = 2
G = 6.67e-11
M = 2.287e30
m1 = 12.00372e24
m2 = 10.451e24
mu = 0 #mean anomaly
a1 = 11249759.82e3
a2 = 17802146.53e3
ratio = a1/a2

#longitude of the ascending node
w1 = math.radians(122)
w2 = math.radians(130)
gamma1 = -w1
gamma2 = -w2

#mean longitude
lambda1 = math.radians(119)
lambda2 = math.radians(122)

#resonant angles
theta1 = lambda1-(2*lambda2)+w1
theta2 = lambda1-(2*lambda2)+w2
theta = theta1-theta2

#reduced mass
u1 = m1*M/(m1+M)
u2 = m2*M/(m2+M)

#capital lambda
clambda1 = u1*math.sqrt(G*(M+m1)*a1)
clambda2 = u2*math.sqrt(G*(M+m2)*a2)

K = u1*math.sqrt(G*(M+m1)*a1) + ((k-1)/k)*u2*math.sqrt(G*(M+m2)*a2)

h1 = 1/(m1*a1**2)
h2 = 1/(m2*a2**2)

#Disturbance function
s = 1/2
x = sp.Symbol('x')
balpha = 2*s*x*(1+(3/8)*x**2+(15/96)*x**4)

#evaluated derivatives in the disturbance function
D1 = sp.Derivative(balpha,x).doit()
D2 = sp.Derivative(D1,x).doit()
D3 = sp.Derivative(D2,x).doit()
balphai = balpha.evalf(subs={x: ratio})
d1 = D1.evalf(subs={x: ratio})
d2 = D2.evalf(subs={x: ratio})
d3 = D3.evalf(subs={x: ratio})

```

```
#Term1: Disturbance function
def R1():
    r1 = (1/2)*(e2)*(7*balpha1+ratio*d1)
    return r1

#Term2: Disturbance function
def R2():
    r2 = (1/18)*(e1**2)*e2*(-252-(20*ratio*d1)+
        (11*d2*ratio**2)+(d3*ratio**3))
    return r2

#Term3: Disturbance function
def R3():
    r3 = (1/16)*(e2**3)*(-358-(26*ratio*d1)+(13*d2*ratio**2)+
        (d3*ratio**3))
    return r3

#Disturbance function with the argument
def Rd():
    disturbfn = R1()+R2()+R3()
    angle = sp.cos(lambda2-w1)

    rd = disturbfn*angle
    return rd

#alpha
def alpha():
    alpha = (G**2)*M*m1*(m2**3)*Rd()/
        (clambda2**2*math.sqrt(clambda1))
    return alpha

#beta
def beta():
    beta = (G**2)*M*m1*(m2**3)*Rd()/
        (clambda2**2*math.sqrt(clambda2))
    return beta

#eta
def eta():
    n = ((4*(alpha()**2+beta()**2))/(
        (9*(h1*(k-1)**2+h2*k**2)**2)))**(1/3)
    return n

#theta/eta
def thetabyeta():
    thet = (u2*math.sqrt(G*(M+m2)*a2))/(eta()*k)
    return thet

#capital gamma with eccentricity
def bg(e1,e2):
    bg1 = u1*math.sqrt(G*(M+m1)*a1)*(e1**2)/2
    bg2 = u2*math.sqrt(G*(M+m2)*a2)*(e2**2)/2
    return (bg1,bg2)

#mu1
def mu1():
    mui = (alpha()*((2*bg(e1,e2)[0])**2)*sp.cos(gamma1)+ 
        beta()*((2*bg(e1,e2)[1])**2)*sp.cos(gamma2))/(
            (alpha()**2+beta()**2)**2)
    return mui
```

```
#v1
def v1():

    v1 = (alpha()*((2*bg(e1,e2)[0])**1/2))*sp.sin(gamma1) +
        beta()*((2*bg(e1,e2)[1])**1/2))*sp.sin(gamma2))/(
            alpha()**2+beta()**2)**1/2
    return v1

#Final Hamiltonian
def Hamiltonian():
    H = (2*h1*(k-1)*K*thetabyeta()/
        (eta()*(2*h1*(k-1)**2+2*h2*k**2))-
        (thetabyeta()**2)-((1/math.sqrt(eta()))*
        (mu1()*sp.cos(theta)-v1()*sp.sin(theta))))
    return H

#range for eccentricities (0.1 to 0.6 in steps of 0.005)
B = [0.1]
for i in range(100):
    B.append(B[i]+0.005)
er = np.array(B)

#Hamiltonians
q = []
d = 1
for e1 in er:
    for e2 in er:
        print(d,".", "e1 =", round(e1,5), ", e2 =", round(e2,5), ",",
              H ="",Hamiltonian())
        d +=1
    q.append(Hamiltonian())

#Minimum Hamiltonian (5397 . e1 = 0.365 , e2 = 0.315 , H =
#-91564460284.0426)
print(min(list(q)))

#3D plot
from mpl_toolkits import mplot3d
get_ipython().run_line_magic('matplotlib', 'inline')
import numpy as np

import matplotlib.pyplot as plt

x1 = np.linspace(0.1, 0.6, num=100)
y1 = np.linspace(0.1, 0.6, num=100)
z1 = []
for e1 in x1:
    for e2 in y1:
        z1.append(Hamiltonian())
z = np.array(z1)
z = z.reshape((len(x1),len(y1)))

# In[ ]:
```

```
X, Y = np.meshgrid(x1, y1)

#fig = plt.figure()
fig= plt.figure(figsize=(16,12))
ax = plt.axes(projection='3d')
ax.contour3D(X, Y, z, 1000, cmap='viridis')
ax.set_xlabel('e1')
ax.set_ylabel('e2')
ax.set_zlabel('H')
ax.view_init(20, 20)
```

B Code for (H, r, e₂)

The following is the code for Case-6 of (H, r, e₂). All the codes for the other cases are similar with just the e₂ value and the r value changing.

```
import math
import sympy as sp
import numpy as np

#Initial parameters
k = 2
G = 6.67e-11
M = 1.989e30
m1 = 1.898e27

m2 = 2*m1
e1 = 0.05
mu = 0 #mean anomaly
a1 = 1

#longitude of the ascending node
w1 = math.radians(122)
w2 = math.radians(130)
gamma1 = -w1
gamma2 = -w2

#mean longitude
lambda1 = math.radians(119)
lambda2 = math.radians(122)
theta1 = lambda1-(2*lambda2)+w1
theta2 = lambda1-(2*lambda2)+w2
theta = theta1-theta2

#reduced mass
u1 = m1*M/(m1+M)
u2 = m2*M/(m2+M)

#capital lambda
def clambda(a1,ratio):
    clambda1 = u1*math.sqrt(G*(M+m1)*a1)
    clambda2 = u2*math.sqrt(G*(M+m2)*(a1/ratio))
    return (clambda1,clambda2)

#K
def K(a1,ratio):
    K = u1*math.sqrt(G*(M+m1)*a1) +
        ((k-1)/k)*u2*math.sqrt(G*(M+m2)*(a1/ratio))
    return K
```

```

def h(a1, ratio):
    h1 = 1/(m1*a1**2)
    h2 = 1/(m2*(a1/ratio)**2)
    return (h1,h2)

#range for eccentricity
A = [0.01]

for i in range(18):
    A.append(A[i]+0.05)
es = np.array(A)

#range for ratio
B = [0.6]
for i in range(9):
    B.append(B[i]+0.05)
er = np.array(B)

#Disturbance function
s = 1/2
x = sp.Symbol('x')
balpha = 2*s*x*(1+(3/8)*x**2+(15/96)*x**4)

#evaluated derivatives in the disturbance function
D1 = sp.Derivative(balpha,x).doit()
D2 = sp.Derivative(D1,x).doit()
D3 = sp.Derivative(D2,x).doit()

def balphai(ratio):
    balphai = balpha.evalf(subs={x: ratio})
    return balphai

def d1(ratio):
    d1 = D1.evalf(subs={x: ratio})
    return d1

def d2(ratio):
    d2 = D2.evalf(subs={x: ratio})
    return d2

def d3(ratio):
    d3 = D3.evalf(subs={x: ratio})
    return d3

#Term1: Disturbance function
def R1():
    r1 = (1/2)*(e2)*(7*balphai(ratio)+ratio*d1(ratio))
    return r1

```

```

#Term2: Disturbance function
def R2():
    r2 = (1/18)*(e1**2)*e2*(-252-(20*ratio*d1(ratio))+  

                (11*d2(ratio)*ratio**2)+  

                (d3(ratio)*ratio**3))
    return r2

#Term3: Disturbance function
def R3():
    r3 = (1/16)*(e2**3)*(-358-(26*ratio*d1(ratio))+  

                (13*d2(ratio)*ratio**2)+  

                (d3(ratio)*ratio**3))
    return r3

#Disturbance function with the argument
def Rd():
    disturbfn = R1()+R2()+R3()
    angle = sp.cos(lambda2-w1)
    rd = disturbfn*angle
    return rd

#alpha
def alpha():
    alpha = (G**2)*M*m1*(m2**3)*Rd() /  

            (clambda(a1, ratio)[1]**2*math.sqrt(clambda(a1, ratio)[0]))
    return alpha

#beta
def beta():
    beta = (G**2)*M*m1*(m2**3)*Rd() /  

            (clambda(a1, ratio)[1]**2*math.sqrt(clambda(a1, ratio)[0]))
    return beta

#eta
def eta():
    n = ((4*(alpha()**2+beta()**2))/(9*(h(a1, ratio)[0]*(k-1)**  

                                              2+h(a1, ratio)[1]*k**2)**2))**(1/3)
    return n

#theta/eta
def thetabyeta():

    thet = (u2*math.sqrt(G*(M+m2)*(a1/ratio)))/(eta()*k)
    return thet

#capital gamma in terms of eccentricities
def bg(e1,e2):
    bg1 = u1*math.sqrt(G*(M+m1)*a1)*(e1**2)/2
    bg2 = u2*math.sqrt(G*(M+m2)*(a1/ratio))*(e2**2)/2
    return (bg1,bg2)

#mui
def mui():
    mui = (alpha()*((2*bg(e1,e2)[0])**1/2))*sp.cos(gamma1)+  

          beta()*((2*bg(e1,e2)[1])**1/2))*  

          sp.cos(gamma2)/(alpha()**2+beta()**2)**1/2
    return mui

#v1
def v1():
    v1 = (alpha()*((2*bg(e1,e2)[0])**1/2))*sp.sin(gamma1)+  

          beta()*((2*bg(e1,e2)[1])**1/2))*sp.sin(gamma2)/  

          (alpha()**2+beta()**2)**1/2
    return v1

```

```

#Final Hamiltonian
def Hamiltonian():
    H = (2*h(a1, ratio)[0]*(k-1)*K(a1, ratio)*thetabyeta()/
        (eta)*(2*h(a1, ratio)[0]*(k-1)**2+2*h(a1, ratio)[1]*k**2))
        )-(thetabyeta()**2)-((1/math.sqrt(eta()))*(mu1()*sp.cos(theta)-v1())*sp.s
    return H

#Hamiltonian Values
l = []
d = 1
for ratio in er:
    for e2 in es:
        print(d,".", "ratio =", ratio, ", e2 =", round(e2,3), ", H"
              ="", Hamiltonian())
        d +=1
    l.append(Hamiltonian())

#Minnimum Hamiltonian

print(min(l))
#125. ratio = 0.9000000000000002 , e2 = 0.51 , H = -17797715.9983390

#3D plot
from mpl_toolkits import mplot3d
get_ipython().run_line_magic('matplotlib', 'inline')
import numpy as np
import matplotlib.pyplot as plt
x1 = np.linspace(0.1, 0.91, num=19)
y1 = np.linspace(0.7, 0.95, num=19)
z1 = []
for e2 in x1:
    for ratio in y1:
        z1.append(Hamiltonian())
z = np.array(z1)
z = z.reshape((len(x1),len(y1)))

X, Y = np.meshgrid(x1, y1)
#fig = plt.figure()
fig= plt.figure(figsize=(16,12))
ax = plt.axes(projection='3d')
ax.contour3D(X, Y, z, 1000, cmap='viridis')
ax.set_xlabel('e2')
ax.set_ylabel('ratio')
ax.set_zlabel('H')
ax.set_zlim(-1.7e7,0)
ax.view_init(20, 20)

```

C Code for the probability simulation

```

import numpy as np
from vpython import *
scene = canvas(width = 1000,height = 1000,center = vector(0,0,0))
graph1 = graph(x = 800,y=0,width= 600,height = 400,title =
'dist_between_planets')
f1= gcurve(color = color.red)

```

```

f2= gcurve(color = color.blue)
t=0
G = 6.674*10**-11
Ms = 2* 10**37          #Mass of star
Mp1 = 10**24            #Mass of planet 1
Mp2 = 10**20            #Mass of planet 2
Ma = 5 *10**36          #Mass of the asteroid
def cross(a,b):
    #Function for cross product
    x = [a.x,a.y,a.z]
    y = [b.x,b.y,b.z]
    x = np.asarray(x)
    y = np.asarray(y)
    return np.dot(np.cross(x,y),np.cross(x,y))**.5
#Defining the objects and their positions
star = simple_sphere(pos=vector(0,0,0),color=color.yellow,radius=
                      7*10**10,emissive = True)
planet1 = simple_sphere(pos = vector(-152*10**9,0,0),radius=10**10,
                        color=color.orange,make_trail =
                        True,retain =100,trail_radius = 10**9)
planet2 = simple_sphere(pos = vector(-520*10**9,0,0),radius=3*10**10,
                        color=color.cyan, make_trail = True,retain =100,
                        trail_radius = 10**9)
asteroid = simple_sphere(pos=vector(-500*10**9,1000*10**9,-500*10**9),
                         radius=3*10**9, color=color.red,
                         make_trail = True,retain =1000,trail_radius = 10**9)
planet1v = vector(0,0,8*10**7)           #Planet 1 velocity
planet2v = vector(0,0,3.5*10**7)         #Planet 2 velocity
asteroidv = 4*10**7 * ((planet2.pos)-(asteroid.pos)) /
             ((planet2.pos)-(asteroid.pos)).mag
                                         #Asteroid velocity

#Defining coordinate axis
a1 = arrow(pos=vector(0,0,0),axis =
           vector(0,0,3*10**11),shaftwidth = 10**9)
a2 = arrow(pos=vector(0,0,0),axis =
           vector(3*10**11,0,0),shaftwidth = 10**9)
a3 = arrow(pos=vector(0,0,0),axis =
           vector(0,3*10**11,0),shaftwidth = 10**9)
neard2 = planet2.pos.mag
fard2 = planet2.pos.mag
neardi1 = planet1.pos.mag
fardi1 = planet1.pos.mag

```

```

dmin = (planet1.pos-planet2.pos).mag          #Distance btw planets
for i in range (1000000):
    rate(5000)                                #Setting up the frame rate
    #Updating planet and asteroid position
    planet1.pos += planet1v
    planet2.pos += planet2v
    asteroid.pos += asteroidv
    asdist = (star.pos-asteroid.pos).mag
    apidist = (planet1.pos-asteroid.pos).mag
    ap2dist = (planet2.pos-asteroid.pos).mag
    sp1dist = planet1.pos.mag
    sp2dist = planet2.pos.mag
    p1p2dist = (planet1.pos - planet2.pos).mag
    apirv = (+planet1.pos-asteroid.pos) / apidist
    ap2rv = (+planet2.pos-asteroid.pos) / ap2dist
    asrv = (-star.pos + asteroid.pos ) / asdist
    spirv = (-star.pos+planet1.pos) / sp1dist
    sp2rv = (-star.pos+planet2.pos) / sp2dist
    pip2rv = (+planet1.pos-planet2.pos) / p1p2dist
    piacc = (-G*Ms*spirv/spidist**2) +
            (-G*Ma*apirv/ap1dist**2) +
            (-G*Mp2*pip2rv/p1p2dist**2)
    p2acc = (-G*Ms*sp2rv/sp2dist**2) +
            (-G*Ma*ap2rv/ap2dist**2) +
            (-G*Mp1*-pip2rv/p1p2dist**2)
    aacc = (-G*Ms*asrv/asdist**2) + (-G*Mp1*apirv/ap1dist**2)
    + (-G*Mp2*ap2rv/ap2dist**2)
    planet1v += piacc
    planet2v += p2acc
    asteroidv +=aacc
    planet1.pos += planet1v
    planet2.pos += planet2v
    asteroid.pos +=asteroidv
    t +=1
Tp1 = 24400 #Time period of the orbit of planet 1
Tp2 = 36400 #Time period of the orbit of planet 2
#Simulation stops When objects collide
if spidist < star.radius or asdist < star.radius or
   sp2dist < star.radius or p1p2dist < planet1.radius or
   pip2dist < planet2.radius :
    break
y = (((planet1.pos-planet2.pos).x * (planet1v-planet2v).x)
      +((planet1.pos-planet2.pos).y*(planet1v-planet2v).y)
      + ((planet1.pos-planet2.pos).z*(planet1v-planet2v).z)) /
      10**8
f1.plot(pos = (t,(planet1.pos-planet2.pos).mag))
if dmin > (planet1.pos-planet2.pos).mag :
    dmin = (planet1.pos-planet2.pos).mag
    U = (planet1v - planet2v).mag
    P = (np.pi * (planet1.radius + planet2.radius) * U) /
        (2*cross(planet1v,planet2v)*Tp1*Tp2)
    print("probability of collision:",P)

```

8 References

- exoplanet.eu. url: <http://exoplanet.eu/catalog/>.
 - Exoplanets database. url: <http://exoplanets.org/table?datasets=explorer>.
 - Trappist 1 - System. url: <http://www.trappist.one/#system>.
- [BK11]** B. Bitsch and W. Kley. \Range of outward migration and influence of the disc's mass on the migration of giant planet cores". In:Astronomy & Astrophysics 536 (2011), A77. doi: 10.1051/0004-6361/201117202. url: <https://doi.org/10.1051%2F0004-6361%2F201117202>.
- [BM13]** K. Batygin and A. Morbidelli. \Analytical treatment of planetary resonances". In: Astronomy & Astrophysics 556 (2013), p. 20.doi: 10.1051/0004-6361/201220907. url: <https://doi.org/10.1051/0004-6361/201220907>.
- [Byr13]** Deborah Byrd. Unseen exoplanet predicted, now conrmed. 2013.url: <https://earthsky.org/space/unseen-exoplanet-predicted-now-confirmed>.
- [CT13]** Renu Malhotra Cristobal Petrovich and Scott Tremaine. \PLANETS NEAR MEAN-MOTION RESONANCES". In: The Astrophysical Journal 770 (2013), p. 16. doi: 10.1088/0004-637X/770/1/24. url: <https://doi.org/10.1088/0004-637X/770/1/24>.
- [CY07]** N. Callegari and T. Yokoyama. \Dynamics of two satellites in the 2/1 Mean{Motion resonance: application to the case of Enceladus and Dione". In: Celestial Mechanics and Dynamical Astronomy 98.1 (2007), pp. 5{30. doi: 10.1007/s10569-007-9066-9. url: <https://doi.org/10.1007%2Fs10569-007-9066-9>.
- [EE13]** Zotos E.E. \Revealing the evolution, the stability, and the escapes of families of resonant periodic orbits in Hamiltonian systems." In: Nonlinear Dyn 73 (2013), pp. 931{962. doi: 10.1007/s11071-013-0844-5. url: <https://doi.org/10.1007/s11071-013-0844-5>.
- [Fab+14]** Daniel C. Fabrycky et al. \ARCHITECTURE OF KEPLER'S MULTI-TRANSITING SYSTEMS. II. NEW INVESTIGATIONS WITH TWICE AS MANY CANDIDATES". In: The Astrophysical Journal 790.2 (2014), p. 146. doi: 10.1088/0004-637x/790/2/146. url: <https://doi.org/10.1088%2F0004-637x%2F790%2F2%2F146>.

[GOL02] GOLDSTEIN. Mechanics. 2002.

[Gup11] Sourendu Gupta. Stability of circular orbits. 2011. url:
<http://theory.tifr.res.in/~sgupta/courses/cm2011/hand12.pdf>.

[Hen+86] J. Henrard et al. \The reducing transformation and Apocentric Librators". In: Celestial Mechanics 38.4 (1986), pp. 335{344. doi: 10.1007/bf01238924. url:
<https://doi.org/10.1007%2Fbf01238924>.

[Hin+10] T. C. Hinse et al. \Application of the MEGNO technique to the dynamics of Jovian irregular satellites". In: Monthly Notices of the Royal Astronomical Society 404.2 (2010), pp. 837{857. doi: 10 . 1111 / j . 1365 - 2966 . 2010 . 16307 . x. url: <https://doi.org/10.1111/j.1365-2966.2010.16307.x>.

[How13] James Howard. Stability of Hamiltonian equilibria. 2013. url: http://www.scholarpedia.org/article/Stability_of_Hamiltonian_equilibria.

[iop17] iop. Simplified Derivation of the Collision Probability of Two Objects in Independent Keplerian Orbits. 2017. url: <https://iopscience.iop.org/article/10.3847/1538-3881/aa6aa7>.

[JMA62] Danby J.M.A. Fundamentals of Celestial Mechanics. 1962.

[LB10] J. Laskar and G. Boue. \Explicit expansion of the three-body disturbing function for arbitrary eccentricities and inclinations". In: Astronomy & Astrophysics 522 (2010), A60. doi: 10.1051/0004 - 6361 / 201014496. url: [https://doi.org/10.1051%2F0004-6361%2F201014496](https://doi.org/10.1051/0004-6361%2F201014496).

[LR95] Jacques Laskar and Philippe Robutel. \Stability of the planetary three-body problem". In: Celestial Mechanics & Dynamical Astronomy 62.3 (1995), pp. 193{217. doi: 10.1007/bf00692088. url: <https://doi.org/10.1007%2Fbf00692088>.

[Mal95] Renu Malhotra. \The Origin of Pluto's Orbit: Implications for the Solar System Beyond Neptune". In: The Astronomical Journal 110 (1995), p. 420. doi: 10.1086/117532. url: <https://doi.org/10.1086%2F117532>.

[MBF08] T. A. Michtchenko, C. Beauge, and S. Ferraz-Mello. \Dynamic portrait of the planetary 2/1 mean-motion resonance { I. Systems with a more massive outer planet". In: Monthly Notices of the Royal Astronomical Society 387.2 (2008), pp. 747{758. doi: 10.1111/j.1365-2966.2008.13278.x. url: <https://doi.org/10.1111%2Fj.1365-2966.2008.13278.x>.

- [MD00]** Ellis Keren M. and Murray Carl D. \The Disturbing Function in Solar System Dynamics". In: *icarus* 147.1 (2000), pp. 129{144. doi: 10.1006/icar.2000.6399. url: <https://ui.adsabs.harvard.edu/abs/2000Icar..147..129E>.
- [MDN16]** MatijaCuk, Luke Dones, and David Nesvorný. \DYNAMICAL EVIDENCE FOR A LATE FORMATION OF SATURN'S MOONS". In: *The Astrophysical Journal* 820.2 (2016), p. 16. doi: 10.3847/0004-637X/820/2/97. url: <https://doi.org/10.3847/0004-637X/820/2/97>.
- [Mor02]** A. Morbidelli. *Modern celestial mechanics: aspects of solar system dynamics* (London: Taylor Francis). 2002.
- [Mur02]** C. D.& Dermott S. F. Murray. *Solar System Dynamics* (Cambridge: Cambridge Univ. Press). 2002.
- [NAS]** NASA. Exoplanets. url: <https://exoplanets.nasa.gov/>.
- [Pea89]** S. J. Peale. \Some unsolved problems in evolutionary dynamics in the solar system". In: *Celestial Mechanics and Dynamical Astronomy* 46.3 (1989), pp. 253{275. doi: 10.1007/bf00049261. url: <https://doi.org/10.1007%2Fbf00049261>.
- [PH05]** Dionyssia Psychoyos and John D. Hadjidemetriou. \Dynamics Of 2/1 Resonant Extrasolar Systems Application to HD82943 and GLIESE876". In: *Celestial Mechanics and Dynamical Astronomy* 92.1-3 (2005), pp. 135{156. doi: 10.1007/s10569-004-1333-4. url: <https://doi.org/10.1007%2Fs10569-004-1333-4>.
- [PP09]** S.-J. Paardekooper and J. C. B. Papaloizou. \On corotation torques, horseshoe drag and the possibility of sustained stalled or outward protoplanetary migration". In: *Monthly Notices of the Royal Astronomical Society* 394.4 (2009), pp. 2283{2296. doi:10.1111/j.1365-2966.2009.14511.x. url: <https://doi.org/10.1111%2Fj.1365-2966.2009.14511.x>.
- [Riv+05]** Eugenio J. Rivera et al. \A □ 7:5ML Planet Orbiting the Nearby Star, GJ 876*". In: *The Astronomical Journal* 634.1 (2005), p. 16. doi: 10 . 1086 / 491669. url: <https://doi.org/10.1086/491669>.
- [Rod+18]** Joseph E. Rodriguez et al. \A Compact Multi-planet System with a Significantly Misaligned Ultra Short Period Planet". In: *The Astronomical Journal* 156.5 (2018), p. 245. doi: 10.3847/1538-3881/aae530. url: <https://doi.org/10.3847%2F1538-3881%2Faae530>.

[Sch10] Kevin C. Schlaufman. \EVIDENCE OF POSSIBLE SPIN-ORBIT MISALIGNMENT ALONG THE LINE OF SIGHT IN TRANSITING EXOPLANET SYSTEMS". In: The Astrophysical Journal 719.1 (2010), pp. 602{611. doi: 10.1088/0004-637x/719/1/602.url: <https://doi.org/10.1088%2F0004-637x%2F719%2F1%2F602>.

[SK06] Zs. Sandor and W. Kley. \On the evolution of the resonant planetary system HD 128311". In: Astronomy & Astrophysics 451.3 (2006), pp. L31{L34. doi: 10.1051/0004-6361:20065196. url: <https://doi.org/10.1051%2F0004-6361%3A20065196>.

[Tin+06] C. G. Tinney et al. \The 2 : 1 Resonant Exoplanetary System Orbiting HD 73526". In: The Astrophysical Journal 647.1 (2006), pp. 594{599. doi: 10.1086/503706. url: <https://doi.org/10.1086%2F503706>.

[TW90] William C. Tittemore and Jack Wisdom. \Tidal evolution of the Uranian satellites". In: Icarus 85.2 (1990), pp. 394{443. doi: 10.1016/0019-1035(90)90125-s. url: <https://doi.org/10.1016/0019-1035%2890%2990125-s>.

[Wis86] Jack Wisdom. \Canonical solution of the two critical argument problem". In: Celestial Mechanics 38.2 (1986), pp. 175{180. doi: 10 . 1007 / bf01230429. url: <https://doi.org/10.1007%2Fbf01230429>.

[Wri+11] J. T. Wright et al. \THE CALIFORNIA PLANET SURVEY. III. A POSSIBLE 2:1 RESONANCE IN THE EXOPLANETARY TRIPLE SYSTEM HD 37124". In: The Astrophysical Journal 730.1 (2011), p. 9. doi: 10.1088/0004-637X/730/2/93. url: <https://doi.org/10.1088/0004-637X/730/2/93>.



EDUCATE - INSPIRE - INNOVATE

www.sserd.org